Neural dynamics in cortical populations

Marius Pachitariu

Dissertation submitted for the degree of
Doctor of Philosophy
of
University College London

Gatsby Computational Neuroscience Unit

University College London

2014

Declaration

I, Marius Pachitariu, declare that this thesis was composed by myself, that the work contained herein is my own except where explicitly stated otherwise in the text, and that this work has not been submitted for any other degree or professional qualification except as specified.

Marius Pachitariu
January 30, 2015

Abstract

Many essential neural computations are implemented by large populations of neurons working in concert. Recent studies have sought both to monitor increasingly large groups of neurons and to characterise their collective behaviour, but the standard computational approaches available to identify the collective dynamics scale poorly with the size of the dataset. We develop new efficient methods for discovering the low-dimensional dynamics that underlie simultaneously-recorded spike trains from a neural population. We use the new models to analyze two different sets of population recordings, one from motor cortex and another from auditory cortex. In motor cortex, we describe the nature of the trial-by-trial spontaneous fluctuations identified by the model and connect these fluctuations to behavioral events. The spatio-temporal structure of the spontaneous events was tracked by three trajectories identified by the model. These trajectories followed similar dynamics during hand reaches as they did when the hands were stationary. The structure of the models we developed allow them to be used as decoders of hand position from neural activity, significantly improving upon previous state-of-the-art methods. The decoders were able to predict information about the direction, onset time and speed profile of movements. In auditory cortex, we use the statistical models to identify population dynamics under different brain states. We report major differences in dynamics and stimulus coding between synchronized and desychronized brain states. Synchronized but not desynchronized brain states imposed constraints on neural dynamics such that a four-dimensional system accounted for most of the dynamical structure of population events. We used the low-dimensional representation of the data to construct network simulations that reproduced the patterns present in the recordings. The simulations suggest that the overall level of feedback inhibition controls the stability of each local cortical network, with unstable dynamics resulting in synchronized brain states. Finally we propose a functional role for dynamics in the representation of visual motion in visual cortex.

Acknowledgments

I thank my supervisor Maneesh Sahani for the guidance and all the help he has provided over the years, and for the connections he has helped me build with other theoretical and experimental researchers.

I thank Peter Dayan for holding the Gatsby Unit together and on a steady course while supporting the diversity of research conducted there. I thank Peter Latham, Yee Whye Teh and Arthur Gretton for providing different viewpoints into science, and I thank my fellow Gatsby colleagues, the students and postdocs with whom I shared my academic and social endeavours. I have started my studies alongside Arthur Guez and I thank him for his camaraderie and for keeping a good pace in the marathon that has been the Gatsby PhD.

I thank my experimental collaborators outside the Gatsby Unit, that have given me practical views into scientific life as well as access to their hard-earned data. They have been a model for me and a continuous source of interesting discussion, helping me shape my armchair analytic thinking to the practical problems of scientific experimentation. At the Ear Institute I have collaborated closely with Nicholas Lesica, who has significantly extended my scientific interests. At the Cruciform I have collaborated with Adam Packer and other members of Michael Häusser's laboratory and I also had the opportunity to work closely with Thomas Mrsic-Flögel, Sonja Hofer, Adil Khan, Jasper Poort and other members of their group. I also thank my collaborators outside London, Krishna Shenoy and members of his lab in Stanford.

Outside of academia, my family has been a constant source of support and so have my friends from Princeton and those from my hometown. Carsen also has been a great source of moral support as well as academic help during the final year of my doctorate.

Contents

List of figures

Outline

This thesis proceeds as follows:

Chapter 1 provides an introduction and literature review on the dynamics of neural populations, multi-neuron recordings and the statistical and network simulation tools we use to analyze them.

Chapter 2 develops the recurrent linear model, a novel and effective class of statistical models of dynamics.

Chapter 3 applies the framework to array recordings from the motor cortex of behaving primates.

Chapter 4 studies the role of spontaneous as well as stimulus-driven dynamics in auditory cortex and uses network simulations to characterize the observed effects in the neural data.

Chapter 5 further develops the statistical models of dynamics to make them suitable to data from sensory cortices. The model captures the statistical patterns and stimulus-interactions in auditory cortex of gerbils across different brain states.

Chapter 6 conducts a thorough investigation on the influence of cortical state on sensory coding in auditory cortex.

Chapter 7 proposes a functional role for dynamics in sensory cortices and develops a theory for how the dynamics can be optimally-adjusted based on sensory experience.

Chapter 8 concludes the thesis with a discussion on how the methods developed here could be used in the context of current emerging neuroscience methods.

I

Introduction

Outline

This chapter starts by considering the collective dynamics of neuronal populations in the brain and our window into these dynamics provided by multi-neuron recordings. We motivate the need for dynamical models fit directly to data sources.

1.1 An informal introduction to the study of brain dynamics

The brain is a complex organ that takes as input external stimuli and produces movements as outputs. Processes in the brain give rise to behavior and the entire transformation from inputs to outputs is dynamical in nature by necessity. Dynamics are used to represent and interpret sensory streams, to modify and use information towards an individual's purposes and goals. More synapses exist between pairs of neurons in cortex than anywhere else, and the continual chit-chat between neurons creates time-dependent processes. Although neural computation is inherently dynamical, we still know very little about how the dynamics are implemented by neural architecture and specifically how they enable the complex transformations most brains can perform.

Dynamics in the brain occur on a multiplicity of temporal and spatial scales. The fast dynamics of ion channels opening and closing are the fundamental basis for the production of quick action potentials that support information processing and synaptic transmission throughout the brain. The slower dynamics result in synapse modifications and enable the formation of life-long memories and learned behaviors. The timescale of dynamics we study in this thesis could be considered intermediate: neurons in spatially localized regions of cortex fire action potentials in a coordinated fashion over periods of tens to hundreds of milliseconds. Their coordinated behavior is enabled by tight interconnections, as well as by the common external inputs they receive. This is the time scale of understanding the visual content of an image or perceiving a spoken word, the timescale of producing a hand movement or visual saccade, the timescale of retrieving memories and recognizing known faces, the timescale of thoughts and ideas.

We wanted to understand cortical dynamics but quickly stumbled across a little-appreciated property of biological networks of neurons: there are ”good” and ”bad” dynamics in the brain. ”Bad” fluctuations in network activity are only weakly-linked to sensory processing or motor production, as we will show over the course of this thesis. The bad dynamics are known, in their extreme instantiation, as up and down state fluctuations or synchronized brain states, typically dominant during sleep or anesthesia. Less extreme versions of bad dynamics occur in awake animals, where population-wide fluctuations in brain activity are still present and dominate the multi-neuron activity patterns in recordings. Periods of synchronized fluctuations in networks have little spatio-temporal structure, and in fact activate all neurons in the network indiscriminately. As such, we regard these dynamics as bad and of little interest to the study of complex computations performed in the brain. We will later show that they constitute a distraction from the more diverse and higher dimensional aspects of cortical processing that can be enabled in networks of neurons.

The contrast between good and bad dynamics is best illustrated with a popular neuroscience metaphor, which we extend. Imagine a stadium seating 40,000 people passionately watching a game together. Listening-in to the roar of the crowd is usually compared to low-resolution brain imaging methods like functional MRI or EEG. Lowering a microphone close to a single person is compared to lowering an electrode in the brain to listen closely to the activity of a single neuron. But if the game is truly engaging, most people will in fact express their enthusiasm at the same timepoints during the game. Thus, listening to what a single person has to say will sound very much like the overall roar of the crowd. Such are synchronized brain states in cortex, because strongly-interconnected networks of neurons can produce and sustain periods of high and indiscriminate neural firing.

Imagine now the same 40000 people instead working together as part of a Fortune 500 company. Their interactions are now spatially limited, their tasks diverse and the structure of the company helps the collective achieve their goals of prosperity. Everyone has their separate role to play and their overall coordination ensures that complex tasks can be achieved. However, there is now no roar of the crowd and listening in to all 40,000 people at once simply sounds like noise. Such is, we believe, the state of the brain when neurons are performing complicated computations together. We will attempt to characterize such states throughout this thesis and emphasize their properties, especially in relation to the states that do not allow for complex computations.

1.2 Collective behavior in networks of neurons

Understanding sensory processing in the cerebral cortex requires characterizing the interactions between stimulus-driven inputs from the periphery and the intrinsic state-dependent dynamics of cortical networks. Cortical dynamics have been characterized relatively well in animals with synchronized brain states. Synchronized brain states are identified by characteristic slow-wave LFP oscillations and occur during sleep, passive wakefulness and under certain anesthetic preparations. Previous studies in synchronized sensory cortices have suggested rather simplistic roles for intracortical dynamics, which are presumed to merely amplify thalamic inputs by a fixed factor regardless of stimulus ([Han and Mrsic-Flogel, 2013]; [Li et al., 2013a]; [Li et al., 2013b]; [Lien and Scanziani, 2013]). These studies appear to disprove a long-standing hypothesis in neuroscience that intracortical dynamics have an important role in performing stimulus-dependent computations. For example, lateral inhibition has been proposed to sharpen the selectivity of principal excitatory cells to external stimulus qualities and generate sensory responses that are susceptible to surround suppression ([Ferster and Miller, 2000]). Experimental work have confirmed surround suppression effects in the responses of neurons in primary visual cortex to stimuli outside their classical receptive fields ([Allman et al., 1985], [Cavanaugh et al., 2002], [Jones et al., 2001]). More recently, direct causal evidence for lateral inhibition has been provided by optical stimulation studies, in which neurons are activated at a specific location in cortex and their effect on other neurons is measured as a function of the distance between their physical locations ([Sato et al., 2013], [Zhang et al., 2014]).

In rodent A1 in particular, intrinsic cortical dynamics observed in synchronized states prevent the network from responding reliably and with temporal precision to tone stimuli ([Bandyopadhyay et al., 2010]; [Bathellier et al., 2012];[Rothschild et al., 2010a]). Moreover, the cortical patterns observed with respect to different tones are highly constrained and generally resemble the patterns observed in spontaneous activity ([Luczak et al., 2009]). Fortunately, radically different patterns of responses are observed in desynchronized states, in which responses to stimuli are well-tuned, reliable and sharply time-locked to stimulus features ([Marguet and Harris, 2011]; [Goard and Dan, 2009]; [Otazu et al., 2009]; [Abolafia et al., 2013], Pachitariu et al, 2015). Desynchronization of cortex occurs at stimulus onset in awake behaving animals ([Tan et al., 2014];[Mitchell et al., 2009]; [Ecker et al., 2014]), as well as in some anesthetized preparations ([Middleton et al., 2012]; [Constantinople and Bruno, 2011]; [Tan et al., 2013]; [Hirata and Castro-Alamancos, 2011]).

Intrinsic cortical dynamics in synchronized cortex have been observed even without thalamic inputs. For example, traveling waves of neuronal activity are ubiquitous in sensory cortices and may facilitate long-range stimulus interactions and higher level computation ([Sato et al., 2012]). When thalamic input is severed, these waves persist both in vivo and in vitro in rodent brain tissue ([Song et al., 2006]; [MacLean et al., 2005]). Synchronized cortical activity is also characterized by periods of population-wide neural firing and subsequent network quiescence (”up” and ”down” states), which require Layer V pyramidal neurons for their generation ([Beltramo et al., 2013a]).

Theoretical models have captured cortical dynamics using a recurrent neural network with short-term synaptic depression which prevents runaway excitation and allows for periodic transitions between ”up” and ”down” states ([Latham et al., 2010]; [Loebel et al., 2007]; [Curto et al., 2009]). Inhibition has also been proposed as a mechanism to control recurrent excitation and sharpen spike timing in cortex ([Wehr and Zador, 2005]; [Murphy and Miller, 2009];[de la Rocha et al., 2007]; [Goard and Dan, 2009];[Wolf et al., 2014]). In particular, in both desynchronized and synchronized auditory cortex, strong inhibitory responses precede excitatory responses ([Zhou et al., 2014b]; [Atencio and Schreiner, 2013];[Sun et al., 2014]; [yun Li et al., 2014]). In desynchronized rodent cortices, inhibitory conductances are shown to dominate excitatory conductances ([Haider et al., 2013]) and there is evidence that certain inhibitory neurons are sharply tuned to the stimulus ([yun Li et al., 2014]; [Sun et al., 2010]). The suppression of responses in auditory cortex lasting hundreds of milliseconds has also been observed in ketamine-anesthetized rats with synchronized brain activity. Inhibitory conductances contribute to suppression for only 50-100 ms after tone onset. This long-lasting suppression has been attributed to synaptic depression [Wehr and Zador, 2005]; [Gabernet et al., 2005]).

1.3 Four types of state-dependent patterns in cortical recordings

We collected multi-neuron spiking activity from the auditory cortex of rodents while in several different brain states. We show that four distinctly identifiable brain states exist. Two of these states have previously been described, the classic desynchronized and synchronized states. The two novel states, which we describe here, will be referred to as synchronized bumpy and desynchronized quiescent. Multi-neuron patterns have qualitatively different properties under these four cortical states both spontaneously and in response to stimuli.

The desynchronized quiescent state is characterized by non-synchronous population responses to stimuli, similar to the classical desynchronized state. Unlike this classical desynchronized state, the desynchronized quiescent state has much lower levels of driven activity and little spontaneous network activation. Response variability and covariability in response to stimuli is very low, even lower than in classical desynchronized states.

We suggest that this quiescent desynchronized state is the relevant desynchronized state for sensory computations. In our experiments, this state produced highly reliable and sparse neural responses and encoded external stimuli flexibly, and with high fidelity.

In order to capture these experimental findings we used a simple network simulation of excitatory and inhibitory populations to show that increased inhibition produces the transition from the classical balanced regimes to the new inhibition-dominated regimes we have observed experimentally and describe here. Our model simulations suggest that network stabilization is state-dependent: classical states operate in a depression-stabilized regime, and desynchronized quiescent cortex is stabilized by inhibition.

Further, we describe a qualitatively different synchronized state, which we refer to as bumpy. This is because ”up” states in such brain states are composed of multiple short and consecutive synchronized periods of population spiking for durations of 30-100ms (Fig. 5.1c). Bumps tended to come together in packets of 2 or 3, and in some recordings even more. They contain significant power at theta frequencies of about 10Hz, in addition to still having power at 1-2Hz, like classical UP/DOWN states.

1.4 Multi-purpose dynamical models

Although network simulations may suffice to capture particular aspects of neural activity, they are often insufficiently constrained by experimental data. Due to this lack of experimental constraints, most network simulation studies assume a random connectivity pattern between neurons ([Renart et al., 2010]). More recently, it has been shown that structured connectivity can generate qualitatively different patterns of neural activity [Litwin-Kumar and Doiron, 2012], but the connectivity pattern used is mostly biologically unsupported for principal excitatory neurons. While connectivity is highly-structured and clustered in cortex among different cell classes, there has been little information about specific connectivity between groups of pyramidal neurons.

Here we argue that the architecture of dynamical models should be inferred directly from datasets of multi-neuron recordings. The Hidden Markov Model (HMM) dynamical framework allows the fitting of a parametric dynamical system to data, and constitutes the basis for much of the work presented here. To allow for an intuitive and biologically-relevant understanding of the HMM framework, consider a simplified scenario in which neurons are clustered into

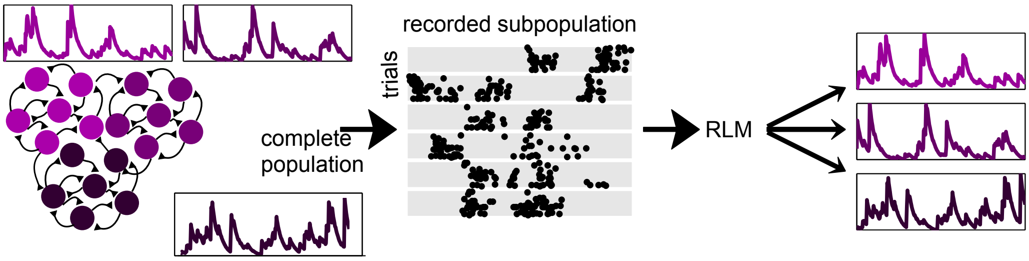

Figure 1.1: **Models can recover underlying dynamics from data.**

tightly-connected groups with weaker across-group connections, as assumed by Litwin-Kumar and Doiron. Barring any additional structure, all the neurons belonging to a single group will respond with relatively similar firing rates, both in spontaneous and in stimulus-driven activity, so that the mean firing rate of a single group of neurons constitutes a good description of the activity of all neurons in that group. We can thus describe the activity of all the neurons in the network in terms of just the mean firing rate of the respective groups and how these groups interact through the weak lateral connections. In the data analyzed here we never encountered a situation where neurons clearly clustered based on their response patterns, so that neurons in the same cluster respond much more similarly than neurons in different clusters. Instead, many neurons shared features of their responses and appeared to encode a weighted sum of some underlying fundamental responses. This situation can still be visualized in the simple clustered-network description above if, following Litwin-Kumar and Doiron we allow neurons to not belong exclusively to one cluster, but gather almost equal inputs from each cluster (see schematic in Fig. 1.1). In such a situation, due to the roughly-clustered structure of the network, neural dynamics may still be described in terms of a few underlying cluster firing rates, but each neuron would be responding as a weighted combination of these mean firing rates. In terms of the connectivity matrix, this model implies a soft-clustering of the connections as opposed to a hard-clustering (where each neuron in the same cluster has exactly the same incoming and outgoing connectivity structure). Soft-clustering implies that the connections of each neuron to the rest of the network are a weighted combination of a few prototypical patterns. Such a connectivity pattern generally corresponds to a low-dimensional recurrent matrix.

More formally, the neural model we will assume throughout this work is one where the matrix of recurrent connectivity effectively has a low-rank component. The simplest example can be understood with linear dynamics

$$\boldsymbol{y}_{t+1} = M\boldsymbol{y}_t$$

where $\boldsymbol{y}_t$ is the vector of firing in bin t and M is the matrix of recurrent connections. Suppose the matrix M can be well described by a reduced-dimensional representation $M = CAC^T$, where C has a small number of columns and is orthonormal $C^TC = \mathrm{I}$. A clustered matrix of connections can be put into this form, but so can a soft-clustering matrix like that described in the previous paragraph. In general, all low-rank matrices M can be put into this form as can be easily derived from the singular value decomposition.

If we define $\boldsymbol{x}_t = C^T\boldsymbol{y}_t$, it follows from our simple linear dynamics that $\boldsymbol{x}_{t+1} = C^T\boldsymbol{y}_{t+1} = C^TM\boldsymbol{y}_t = (C^TC)A(C^T\boldsymbol{y}_t) = A\boldsymbol{x}_t$. We thus have an equivalent set of linear dynamics that describe the evolution of $\boldsymbol{x}_t$ by $\boldsymbol{x}_{t+1} = A\boldsymbol{x}_t$, and these dynamics are now low-dimensional. The individual neuron firing rates can now be determined as $\boldsymbol{y}_{t+1} = M\boldsymbol{y}_t = CA(C^T\boldsymbol{y}_t) = C(A\boldsymbol{x}_t) = C\boldsymbol{x}_{t+1}$. We say that the dynamics of $\boldsymbol{x}_t$ are latent and unobserved, while in typical neural recordings we only observe the spiking of individual neurons in the population $\boldsymbol{y}_t$. If we can recover or infer $\boldsymbol{x}_t$ from the observed $\boldsymbol{y}_t$, then we will have a good picture of the dynamics of the entire (unrecorded) local population. This toy linear model exemplifies very well the types of analysis we will do in the rest of the thesis, but nonlinearities will have to be added for us to be able to model strictly positive firing rates and spiking point processes (see chapter 2).

The statistical models we develop here attempt to recover the underlying low-dimensional dynamics that are sufficient to predict with good accuracy the spike times of recorded neurons (Fig. 1.1). Because the network structure generates the observed responses, we may thus be able to understand connectivity patterns in cortex, purely from the statistical patterns of multi-neuron recordings. A graphical summary of the procedure for recovering HMMs is shown in figure

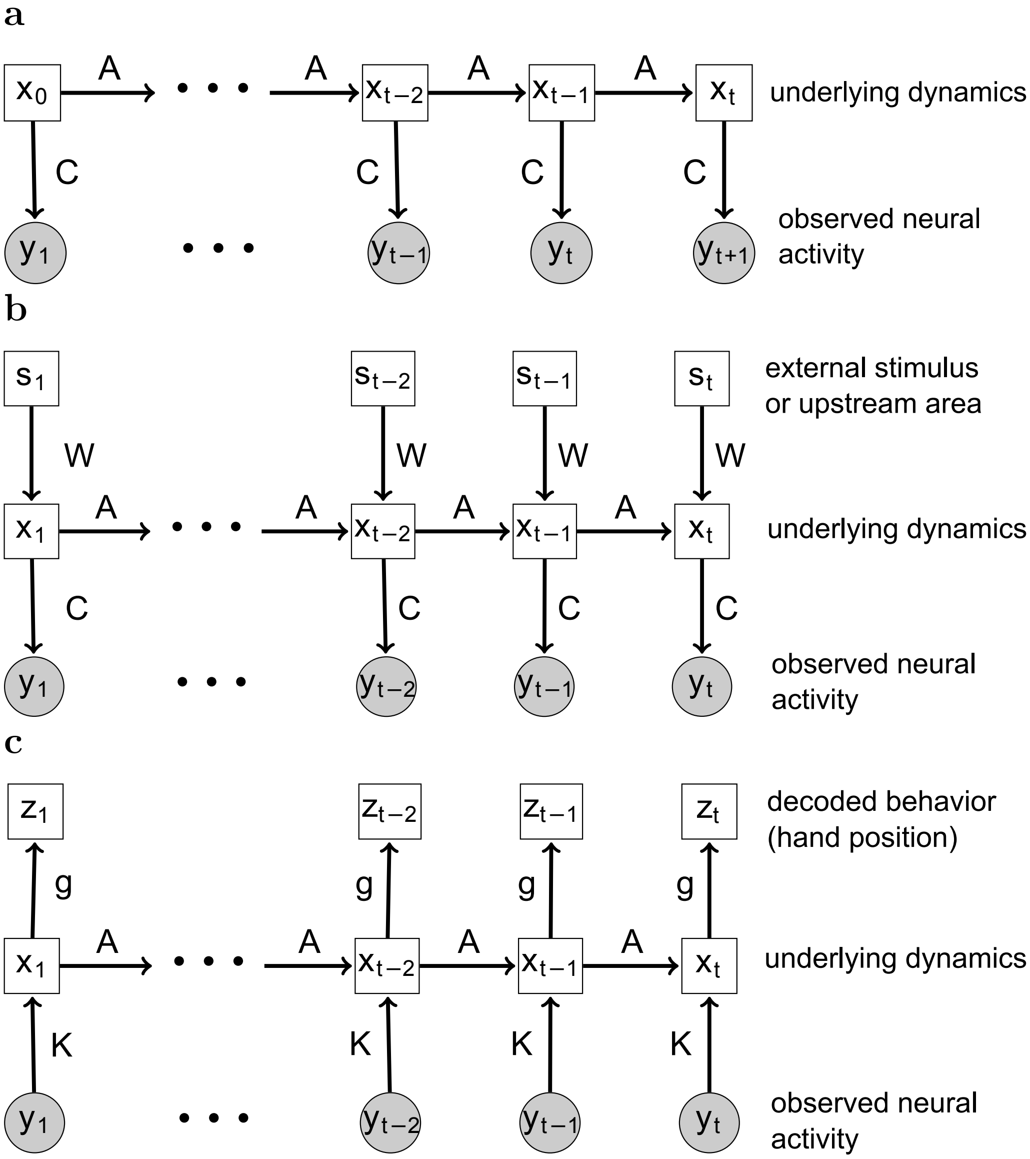

Figure 1.2: **Multi-purpose dynamical models. a)** Intrinsic dynamics in neural recordings. **b)** Dynamical encoding of feedforward inputs. **c)** Dynamical decoding of brain activity.

1.2a, and will be detailed in the next chapter. In summary, we use the neural activities up to time t to track the underlying dynamics, and use these dynamics to predict neural firing at time $t+1$. Such tracking algorithms as we develop here have a long history, going all the way back to the Kalman filter [Kalman, 1960].

In the picture provided by figure 1.1, other uses for dynamical models can be devised. For example, we may want to study how a neural population collectively encodes an external stimulus, that arrives as inputs to each neuron in the network. In such a situation, the reduced-dimensional dynamics can still help, because the network contribution to each neuron's response will still be low-dimensional following the low dimensional structure. If the recurrent contribution dominates the feedforward inputs, then neurons in the network will essentially still respond as weighted combinations of the stimulus-driven underlying dynamics, such as described in the graph of figure 1.2b. The parameters of such a transformation can still be recovered directly from data, provided we have access to the stimulus.

We describe the feedforward model in the simple linear toy model presented above. Suppose now the dynamical evolution of the neural activities proceeds as

$$\boldsymbol{y}_{t+1} = M\boldsymbol{y}_t + T\boldsymbol{s}_t$$

where $\boldsymbol{s}_t$ is the vector of external stimuli and T is a projection matrix from the stimuli to the neurons. Following a similar derivation as before, the activities of the low-rank dynamics $\boldsymbol{x}_t$ now proceeds as

$$\boldsymbol{x}_{t+1} = A\boldsymbol{x}_t + (C^T T)\boldsymbol{s}_t$$

and we can rewrite $y_{t+1} = Cx_{t+1} + ((\mathrm{Id} - CC^T)T)s_t$, where Id is the identity matrix. So we see the activity of each neuron can still be represented in terms of the low-dimensional stimulus-driven network activity, together with a purely feedforward component. Depending on the modelling scenario, we will either ignore the feedforward component (we assume it is small compared to the recurrent drive, see chapter 4) or model it explicitly (chapter 5).

Finally, a third use for dynamical models is in decoding information from multi-unit recordings. In motor cortex, the population activity of neurons drives muscles and produces movements. Thus, a relationship exists between neural activity and movements, which we may be able to capture by driving a dynamical system with inputs from the recorded neural activity (Figure 1.2c). Good performance in capturing such transformations may eventually enable good brain machine interfaces of the kind useful in medical prosthetic applications.

Using the toy linear model we have used above, we assume that kinematic variables $\boldsymbol{z}_t$ (position, velocity etc.) are driven linearly by the network state such that $\boldsymbol{z}_t = Q\boldsymbol{x}_t$, a direct projection from the latent dynamics x_t. Thus we get the picture presented in figure 1.2c, where we use the recorded neural activity $\boldsymbol{y}_t$ to estimate $\boldsymbol{x}_t$, and in turn use $\boldsymbol{x}_t$ to estimate the kinematic variables $\boldsymbol{z}_t$. Again we emphasize that the toy linear model is a simplification and nonlinearities need to be added to this simplified picture. For the decoder, a nonlinearity $\mathbf{g}$ was necessary to transform signals from the latent space to the physical space of the kinematic variables.

Examples of each of these three uses of our dynamical systems framework can be found throughout this work. Chapters 2, 3 and 5 use the intrinsic dynamics recovery model (Fig. 1.2a), chapters 4 and 5 use the stimulus-driven models of dynamics (Fig. 1.2b), and chapter 3 also uses the dynamical decoder of neural activity (Fig. 1.2c).

II

Recurrent linear models of simultaneously-recorded neural populations

Outline

Population recordings of neurons with a temporal structure that occurs on long timescales are often best understood in terms of a shared underlying low-dimensional dynamical process. Advances in recording technology provide access to an ever larger fraction of the neural population, but the standard computational approaches available to identify the collective dynamics scale poorly with the increasing sizes of these datasets. Here we describe a new, scalable approach to discovering the low-dimensional dynamics that underlie simultaneously recorded spike trains from neural populations. Our method is based on recurrent linear models (RLMs) and relates closely to timeseries models based on recurrent neural networks. We formulate RLMs for neural data by generalising the Kalman-filter-based likelihood calculation for latent linear dynamical systems (LDS) models to incorporate a generalised-linear observation process. We show that RLMs describe motor-cortical population data better than either directly-coupled generalised-linear models or latent linear dynamical system models with generalised-linear observations. We also introduce the cascaded linear model (CLM) to capture low-dimensional instantaneous correlations in neural populations. The CLM describes the cortical recordings better than either Ising or Gaussian models and, like the RLM, can be fit exactly and quickly. The CLM can also be seen as a generalization of a low-rank Gaussian model, in this case factor analysis. The computational tractability of the RLM and CLM allow both to scale to very high-dimensional neural data.

2.1 Introduction

[1] Many essential neural computations are implemented by large populations of neurons working in concert, and recent studies have sought both to monitor increasingly large groups of neurons [Schneidman et al., 2005, Buzsaki, 2004] and to characterise their collective behaviour [Pillow et al., 2008, Churchland et al., 2007]. Here we introduce a new computational tool to model coordinated behaviour in very large neural data sets. While we explicitly consider only multi-electrode array recordings of spiking neurons, the same model can be readily used to characterise data generated by the two-photon imaging of population activity using calcium-sensitive indicators, EEG, fMRI or even large scale biologically-faithful simulations.

The activity of neural populations may be represented at each time point by a vector $\boldsymbol{y}_t$ with as many dimensions as neurons, and as many indices t as time points in the experiment. For spiking neurons, $\boldsymbol{y}_t$ will have positive integer elements corresponding to the number of spikes fired by each neuron in the time interval corresponding to the t-th bin. As others before [Yu et al., 2006, Macke et al., 2011], we assume that the coordinated activity reflected in the measurement $\boldsymbol{y}_t$ arises from a low-dimensional set of processes, collected into a vector $\boldsymbol{x}_t$, which is not directly observed. However, unlike previous studies, we construct a recurrent model in which the hidden processes $\boldsymbol{x}_t$ are driven directly and explicitly by the measured neural signals $\boldsymbol{y}_1 \ldots \boldsymbol{y}_{t-1}$. This assumption simplifies the estimation process: we assume for simplicity that $\boldsymbol{x}_t$ evolves with linear dynamics, and affects the future state of the neural signal $\boldsymbol{y}_t$ in a generalised-linear manner, although both assumptions may be relaxed. As in the latent LDS, the resulting model enforces a "bottleneck", whereby predictions of $\boldsymbol{y}_t$ based on $\boldsymbol{y}_1 \ldots \boldsymbol{y}_{t-1}$ must be carried by the low-dimensional $\boldsymbol{x}_t$.

State prediction in the RLM is related to the Kalman filter [Kalman, 1960] and we show in the next section a formal equivalence between the likelihoods of the

[1] The data used in this chapter has been generously made available by Krishna Shenoy and was recorded in his laboratory by Mark Churchland.

RLM and a latent LDS model when observation noise is normally distributed. However, spiking data is not well modelled as Gaussian, and the generalisation of our approach to Poisson noise leads to a departure from the latent LDS approach. Unlike LDS models with conditionally Poisson observations, the parameters of our model can be estimated efficiently and without approximation. We show that, perhaps in consequence, the RLM can provide superior descriptions of neural population data.

2.2 From Kalman filters to recurrent linear models

Consider a latent LDS model with linear-Gaussian observations (which we will abbreviate as GLDS). Its graphical model is shown in Fig. 2.1 (top). The latent dynamics are parametrised by a dynamics matrix A and innovations covariance Q that describe the evolution of the latent state $\boldsymbol{x}_t$:

$$P(\boldsymbol{x}_t|\boldsymbol{x}_{t-1}) = \mathcal{N}(\boldsymbol{x}_t|A\boldsymbol{x}_{t-1}, Q)\,,$$

where $\mathcal{N}(x|\mu, \Sigma)$ represents a normal distribution on x with mean μ and (co)variance Σ. For brevity, we omit here and below the special case of the first time-step, in which $\boldsymbol{x}_1$ is drawn from a multivariate Gaussian. The output distribution involves an observation loading matrix C and a noise covariance R often taken to be diagonal so that all covariance is modelled by the latent process:

$$P(\boldsymbol{y}_t|\boldsymbol{x}_t) = \mathcal{N}(\boldsymbol{y}_t|C\boldsymbol{x}_t, R)\,.$$

In this GLDS, the joint likelihood of the observations $\{\boldsymbol{y}_t\}$ can be written as the product:

$$P(\boldsymbol{y}_1 \dots \boldsymbol{y}_T) = P(\boldsymbol{y}_1) \prod_{t=2}^{T} P(\boldsymbol{y}_t|\boldsymbol{y}_1 \dots \boldsymbol{y}_{t-1})$$

and can be computed using the usual Kalman filter approach to find the conditional distribution at time t iteratively:

$$\begin{aligned}
P(\boldsymbol{y}_{t+1}|\boldsymbol{y}_1 \ldots \boldsymbol{y}_t) &= \int d\boldsymbol{x}_{t+1}\, P(\boldsymbol{y}_{t+1}|\boldsymbol{x}_{t+1}) P(\boldsymbol{x}_{t+1}|\boldsymbol{y}_1 \ldots \boldsymbol{y}_t) \\
&= \int d\boldsymbol{x}_{t+1}\, \mathcal{N}(\boldsymbol{y}_{t+1}|C\boldsymbol{x}_{t+1}, R)\, \mathcal{N}(\boldsymbol{x}_{t+1}|A\hat{\boldsymbol{x}}_t, V_{t+1}) \\
&= \mathcal{N}(\boldsymbol{y}_{t+1}|CA\hat{\boldsymbol{x}}_t, CV_{t+1}C^\top + R)\,,
\end{aligned}$$

where we have introduced the (filtered) state estimate $\hat{\boldsymbol{x}}_t = \mathsf{E}\left[\boldsymbol{x}_t|\boldsymbol{y}_1 \ldots \boldsymbol{y}_t\right]$ and (predictive) uncertainty $V_{t+1} = \mathsf{E}\left[(\boldsymbol{x}_{t+1} - A\hat{\boldsymbol{x}}_t)^2|\boldsymbol{y}_1 \ldots \boldsymbol{y}_t\right]$. Both quantities are computed recursively using the Kalman gain $K_t = V_t C^\top (CV_tC^\top + R)^{-1}$, giving the following recursive recipe to calculate the conditional likelihood of $\boldsymbol{y}_{t+1}$:

$$\begin{aligned}
\hat{\boldsymbol{x}}_t &= A\hat{\boldsymbol{x}}_{t-1} + K_t(\boldsymbol{y}_t - \hat{\boldsymbol{y}}_t) \\
V_{t+1} &= A(I - K_tC)V_tA^\top + Q \\
\hat{\boldsymbol{y}}_{t+1} &= CA\hat{\boldsymbol{x}}_t \\
P(\boldsymbol{y}_{t+1}|\boldsymbol{y}_1 \ldots \boldsymbol{y}_t) &= \mathcal{N}(\boldsymbol{y}_{t+1}|\hat{\boldsymbol{y}}_{t+1}, CV_{t+1}C^\top + R)
\end{aligned}$$

For the GLDS, the Kalman gain K_t and state uncertainty V_{t+1} (and thus the output covariance $CV_{t+1}C^\top + R$) depend on the model parameters (A, C, R, Q) and on the time step—although as time grows they both converge to stationary values. Neither depends on the observations.

Thus, we might consider a relaxation of the GLDS model in which these matrices are taken to be stationary from the outset, and are parametrised independently so that they are no longer constrained to take on the "correct" values as computed for Kalman inference. Let us call this parametric form of the Kalman gain W and the parametric form of the output covariance S. Then the conditional likelihood iteration becomes

$$\begin{aligned}
\hat{\boldsymbol{x}}_t &= A\hat{\boldsymbol{x}}_{t-1} + W(\boldsymbol{y}_t - \hat{\boldsymbol{y}}_t) \\
\hat{\boldsymbol{y}}_{t+1} &= CA\hat{\boldsymbol{x}}_t \\
P(\boldsymbol{y}_{t+1}|\boldsymbol{y}_1 \ldots \boldsymbol{y}_t) &= \mathcal{N}(\boldsymbol{y}_{t+1}|\hat{\boldsymbol{y}}_{t+1}, S)\,.
\end{aligned}$$

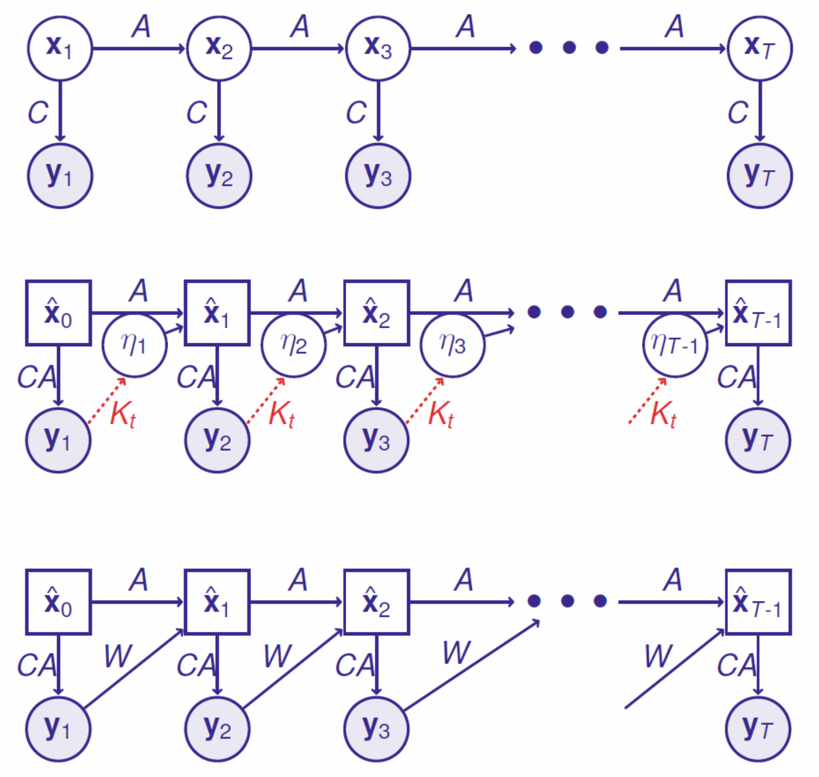

Figure 2.1: Graphical model representations of linear dynamical systems (top, middle) and recurrent linear models (bottom). Shaded variables are observed, non-shaded circles are latent random variables and squares are variables that depend deterministically on their parents. The middle graph redraws the LDS in terms of the innovations $\boldsymbol{\eta}_t = \boldsymbol{x}_t - A\boldsymbol{x}_{t-1}$ to facilitate the transition towards the RLM. The RLM model is then obtained by replacing $\boldsymbol{\eta}_t$ (middle) with a deterministic prediction $W(\boldsymbol{y}_t - \hat{\boldsymbol{y}}_t)$.

The parameters of this new model are A, C, W and S. This is a relaxation of the latent GLDS model because W has more degrees of freedom than Q, as does S than R (at least if R is constrained to be diagonal). The new model has a recurrent linear structure in that the random observation $\boldsymbol{y}_t$ is fed back linearly to perturb the otherwise deterministic evolution of the state $\hat{\boldsymbol{x}}_t$. We call it a Gaussian Recurrent Linear Model (GRLM).

A graphical representation of this model is shown in Fig. 2.1 (bottom), along with a redrawn graph of the LDS model (middle). The RLM can be viewed as replacing the random innovation variables $\boldsymbol{\eta}_t = \boldsymbol{x}_t - A\boldsymbol{x}_{t-1}$ with data-derived estimates $W(\boldsymbol{y}_t - \hat{\boldsymbol{y}}_t)$; estimates which are made possible by the fact that $\boldsymbol{\eta}_t$ contributes to the variability of $\boldsymbol{y}_t$ around $\hat{\boldsymbol{y}}_t$.

2.3 Recurrent linear models with Poisson observations

The discussion above has transformed a stochastic latent LDS model with Gaussian output to an RLM with deterministic latent, but still with Gaussian output. Our goal, however, is to fit a model with an output distribution more suitable for modelling the binned point-processes that characterise neural spiking. Both linear Kalman-filtering steps above and the eventual stationarity of the inference parameters depend on the joint Gaussian structure of the GLDS model. They would not apply if we were to begin a similar derivation from an LDS with Poisson output. However, a tractable approach to modelling point-process data with low-dimensional temporal structure may be provided by introducing a generalised-linear output stage *directly* to the RLM (a model we call a gl-RLM). This model is given by:

$$\begin{aligned} \hat{\boldsymbol{x}}_t &= A\hat{\boldsymbol{x}}_{t-1} + W(\boldsymbol{y}_t - \hat{\boldsymbol{y}}_t) \\ g(\hat{\boldsymbol{y}}_{t+1}) &= CA\hat{\boldsymbol{x}}_t \\ P(\boldsymbol{y}_{t+1}|\boldsymbol{y}_1 \ldots \boldsymbol{y}_t) &= \mathsf{ExpFam}(\boldsymbol{y}_{t+1}|\hat{\boldsymbol{y}}_{t+1}) \end{aligned} \tag{2.1}$$

where ExpFam is an exponential-family distribution such as Poisson, and the element-wise link function g allows for a nonlinear mapping from $\boldsymbol{x}_t$ to the predicted mean $\hat{\boldsymbol{y}}_{t+1}$. In the following, we will write f for the inverse-link as is more common for neural models, so that $\hat{\boldsymbol{y}}_{t+1} = \mathrm{f}(CA\hat{\boldsymbol{x}}_t)$.

The simplest Poisson-based gl-RLM might take as its output distribution

$$P(\boldsymbol{y}_t|\hat{\boldsymbol{y}}_t) = \prod_i \mathsf{Poisson}(y_{ti}|\hat{y}_{ti}); \qquad \hat{\boldsymbol{y}}_t = \mathrm{f}(CA\hat{\boldsymbol{x}}_{t-1}))\,,$$

where y_{ti} is the spike count of the ith cell in bin t and the (inverse) link f is non-negative. However, comparison with the output distribution derived for the GRLM suggests that this choice would fail to capture the instantaneous covariance that the LDS formulation transfers to the output distribution (and which appears in the low-rank structure of S above). We can address this concern in two ways. One option is to bin the data more finely, thus diminishing the influence of the instantaneous covariance. The alternative is to replace the independent Poissons with a correlated output distribution on spike counts. The cascaded generalized-linear model introduced below is a natural choice, and we show that it captures instantaneous correlations faithfully with very few hidden dimensions.

In practice, we also sometimes add a fixed input $\boldsymbol{\mu}_t$ to equation 2.1 that varies in time and determines the average behavior of the population or the peri-stimulus time histogram (PSTH).

$$\hat{\boldsymbol{y}}_{t+1} = \mathrm{f}\left(\boldsymbol{\mu}_t + CA\boldsymbol{x}_t\right)$$

Note that the matrices A and C retain their interpretation from the LDS models. The matrix A controls the evolution of the dynamical process $\boldsymbol{x}_t$. The phenomenology of its dynamics is determined by the complex eigenvalues of A. Eigenvalues with moduli close to 1 correspond to long timescales of fluctuation around the PSTH. Eigenvalues with non-zero imaginary part correspond to oscillatory components. Finally, the dynamics will be stable if and only if all the eigenvalues lie within the unit disc. The matrix C describes the dependence of the high-dimensional neural signals on the low-dimensional latent processes $\boldsymbol{x}_t$. In particular, equation 2.2 determines the firing rate of the neurons. This generalized-linear stage ensures that the firing rates are positive through the link function f, and the observation process is Poisson. For other types of data, the generalized-linear stage might be replaced by other appropriate link functions and output distributions.

2.3.1 Relationship to other models

RLMs are also related to recurrent neural networks (RNN) [Elman, 1990]. An RNN can be obtained from the RLM by replacing the innovation term $W\left(\boldsymbol{y}_{t-1} - \hat{\boldsymbol{y}}_t\right)$ with $W\boldsymbol{y}_{t-1}$ and adding a nonlinearity in the hidden process $\boldsymbol{x}_t = h\left(A\boldsymbol{x}_{t-1} + W\boldsymbol{y}_{t-1}\right)$. We found that using sigmoidal or threshold-linear functions h resulted in models as good as the linear version of the model for the dataset used in this paper and so we restrict our attention to simple linear dynamics. We also found that using the full prediction error term $W\left(\boldsymbol{y}_{t-1} - \hat{\boldsymbol{y}}_t\right)$ resulted in better models than the simple RNN formulation, and we attribute this difference to the similarity of the RLM to Kalman filter models.

We might also consider a more straightforward generalization of the LDS to generalized-linear observations, recently proposed as the Poisson-LDS model [Macke et al., 2011], which directly replaces the Gaussian output distribution of the LDS with a Poisson output. The main difficulty with such models is the intractability of the estimation procedure. For an unobserved latent process $\boldsymbol{x}_t$, an inference procedure needs to be devised to estimate the posterior distribution on the entire sequence $\boldsymbol{x}_1 \ldots \boldsymbol{x}_t$. For linear-Gaussian observations, this inference procedure is tractable and corresponds to the Kalman smoother. However, with generalized-linear observations the inference becomes intractable and approximations need to be devised like those of [Macke et al., 2011]. These approximations are computationally intense and can jeopardize the quality of the fitted models. In contrast, in our model $\boldsymbol{x}_t$ is a deterministic function of the data. In other words, the Kalman filter has been built into the model as the accurate estimation procedure and fitting the model can be done efficiently by standard gradient ascent on the log-likelihood of the model. Empirically we did not encounter local minima issues during optimization, as reported for LDS type models fitted with an EM algorithm [Buesing et al., 2012]. Multiple restarts from different random values of the parameters always led to models with similar likelihoods.

Notice that in order to estimate the matrices A and W the gradient needs to be backpropagated through successive iterations of equation 2.1. This technique is known as backpropagation-through-time (BPTT) and has been initially described by [Rumelhart et al., 1986] as a technique to fit recurrent neural network models. More recent implementations have proved to be state-of-the-art language models [Mikolov et al., 2011]. BPTT is thought to be inherently unstable when propagated past many timesteps and often the gradient is truncated after several time steps [Mikolov et al., 2011]. We found that using large values of momentum in the gradient ascent alleviates these instabilities and allowed us to use BPTT without the truncation.

2.4 Cascaded linear models

Our derivation of RLMs from LDS models has motivated us to search for similar extensions of Gaussian models to describe correlated distributions on simultaneous spike counts. Such distributions are useful in modelling neural activity when we ignore the temporal structure of the dynamics. We can instead describe solely the distribution of spike counts $\boldsymbol{y}$ recorded during brief temporal windows [Schneidman et al., 2005] (note that we have dropped the time index t). By describing the distribution of $\boldsymbol{y}$ we can determine what parts of the large N-dimensional space are visited by the neural activity. What types of models should we use to describe the distribution of $\boldsymbol{y}$? The simplest perhaps is a Gaussian model which can accurately capture the full covariance structure of $\boldsymbol{y}$. The weakness of the Gaussian model is that it assumes continuous-valued vectors $\boldsymbol{y}$, which spike counts obviously are not.

As with the derivation of the RLM from the Kalman filter, we obtain a new generalization of a Gaussian model to spike count data. The distribution of a multivariate variable $\boldsymbol{y}$ can be factorized as a product of multiple one-dimensional distributions:

$$\mathrm{P}\left(\boldsymbol{y}\right) = \prod_{n=1}^{N} \mathrm{P}\left(y_n | y_{<n}\right). \tag{2.2}$$

Here n indexes the neurons up to the last neuron N. For a Gaussian distributed $\boldsymbol{y}$, the conditionals $\mathrm{P}\left(y_n | y_{<n}\right)$ are linear-Gaussian but we can change these one-dimensional distributions to generalized-linear observations just like we did for the RLM

$$\hat{\boldsymbol{y}}_n = \mathrm{f}\left(\mu_n + S_n^T \boldsymbol{y}_{<n}\right) \tag{2.3}$$

$$\mathrm{P}\left(y_n | y_{<n}\right) = \mathrm{Poisson}\left(\hat{\boldsymbol{y}}_n\right). \tag{2.4}$$

The prediction for neuron n must be based only on the activities of the neurons with indices up to $n-1$ (written $\boldsymbol{y}_{<n}$). When f is linear and the Poisson conditionals are replaced with Gaussians, equations 2.3 and 2.4 describe exactly all full-covariance Gaussians. If the covariance of the Gaussian model is Σ, a simple calculation shows that

$$S_n = \frac{1}{\left(\Sigma^{-1}\right)_{n,n}} \left(\Sigma_{<n,<n}\right)^{-1}_{n,<n} . \tag{2.5}$$

Our goal however was to define a low-dimensional model on instantaneous spike count data. This can be achieved for linear-Gaussian observations if instead of starting from any full-covariance Gaussian model, we start from a factor analysis model [Bishop, 2006]. Factor analysis assumes the data is generated from a low-dimensional latent process $\boldsymbol{x} \sim \mathcal{N}(0, I)$, where I is the identity matrix. $\boldsymbol{y}$ is then obtained such that $\mathrm{P}(\boldsymbol{y}|\boldsymbol{x}) = \mathcal{N}(\Lambda\boldsymbol{x}, \Psi)$ with Ψ a diagonal matrix and Λ a loading matrix. In factor analysis, the covariance of $\boldsymbol{y}$ is $\Psi + \Lambda\Lambda^T$. If we repeat the derivation of equations 2.3, 2.4 and 2.5 for this covariance matrix, we obtain an expression for S_n via the matrix inversion lemma:

$$\begin{aligned} S_n &= \frac{1}{\left(\Sigma^{-1}\right)_{n,n}} \left(\Psi_{<n,<n} + \Lambda_{<n}\Lambda^T_{<n}\right)^{-1}_{n,<n} \\ &= \frac{1}{\left(\Sigma^{-1}\right)_{n,n}} \left(\Psi^{-1}_{<n,<n} + \Psi^{-1}_{<n,<n}\Lambda_{<n} + \cdots\right)_{n,<n} , \end{aligned}$$

where the dots omit further factors in the inverse matrix expansion. Taking into account that Ψ is diagonal, we see that S_n is a linear combination of the columns of $\Psi^{-1}\Lambda$ for all n, followed by a truncation to the first $n-1$ elements. If we arrange all S_n as upper columns of an N by N matrix S, then we can write $S = \text{upper}\left(zw^T\right)$ for some low-dimensional matrices $z = \Psi^{-1}\Lambda$ and w, where the operation upper extracts the strictly upper triangular part of a matrix. Finally, we can easily impose this constraint on S even for generalized-linear observations. The resulting cascaded linear model (CLM) is shown to provide better fits to binarized neural data than standard Ising models (see the Results section), even with as few as three dimensions of common input.

Another strong property of the CLM is that it allows stimulus-dependent inputs in equation 2.3. The CLM can also be used in combination with the RLM, where the CLM replaces the observation model of the RLM. This approach can be useful when large bins are used to discretize spike trains. In both cases the model can be estimated quickly with standard gradient ascent techniques.

2.5 Alternative models

2.5.1 Alternative for temporal interactions: causally-coupled generalized linear model

One popular and simple model of simultaneously recorded neuronal populations [Pillow et al., 2008] constructs temporal dependencies between units by directly coupling a neuron's probability to fire with the histories of all other neurons and its own history as described by the following equation:

$$\mathbf{y}_t \propto \text{Poisson}(\text{f}(\mu_t + \sum_{i=1}^{N_t} B_i \left(h_i \star \mathbf{y}_t\right)))$$

$h_i \star \mathbf{y}_t$ are convolutions of the spike trains with a set of basis functions h_i and B_i are the pairwise interaction terms. Each matrix B_i has N^2 parameters where N is the number of neurons, so the number of parameters grows quadratically with the population size. This type of scaling makes the model prohibitive to use with large-scale array recordings. Even with aggressive regularization techniques, the model's parameters are difficult to identify with limited amounts of data. Perhaps more importantly, the model does not have a physical interpretation. Neurons recorded in cortex are rarely directly connected, and retinal ganglion cells almost never directly connect to each other. Instead, such directly coupled GLMs are used to describe so-called functional interactions between neurons [Pillow et al., 2008]. We believe a much better interpretation for the correlations observed between pairs of neurons is that they are caused by common and low-dimensional inputs to these neurons and the models we propose here, the RLM and the CLM, are aimed at discovering these inputs.

2.5.2 Alternative for instantaneous interactions: the Ising model

For instantaneous interactions, a model from statistical physics is available that can also capture the full covariance structure of $\boldsymbol{y}$ if we assume that each entry in $\boldsymbol{y}$ is either 0 or 1 [Schneidman et al., 2005]. This is called the Ising model and is given by equation

$$\mathrm{P}\left(\boldsymbol{y}\right) = \frac{1}{Z}\ \mathrm{e}^{\boldsymbol{y}^T J \boldsymbol{y}}. \tag{2.6}$$

where J is a pairwise interaction matrix and Z is the partition function, or the normalization constant of the model. The model's attractiveness is that for a given covariance structure it makes the least assumptions about the distribution of $\boldsymbol{y}$, or in other words has the largest entropy. However, the Ising model and the so-called functional interactions J have no physical interpretation when applied to data recorded in the brain. Furthermore, Ising models are difficult to fit as they require estimates of the gradients of the partition function Z. The models become much more difficult to estimate with an increasing number of neurons as the number of parameters grows quadratically with the number of neurons. Ising models are even harder to estimate when stimulus-dependent inputs are added in equation 2.6. For datasets collected in the retina or other sensory areas [Schneidman et al., 2005], much of the covariability in $\boldsymbol{y}$ is expected to be due to a common stimulus input. Another short coming of the Ising model is that it can only model binarized data and cannot be normalized for integer $\boldsymbol{y}$'s [Macke et al., 2011], so either the time bins need to be reduced to ensure no neuron fires more than one spike in a single bin or the spike counts must be capped at 1.

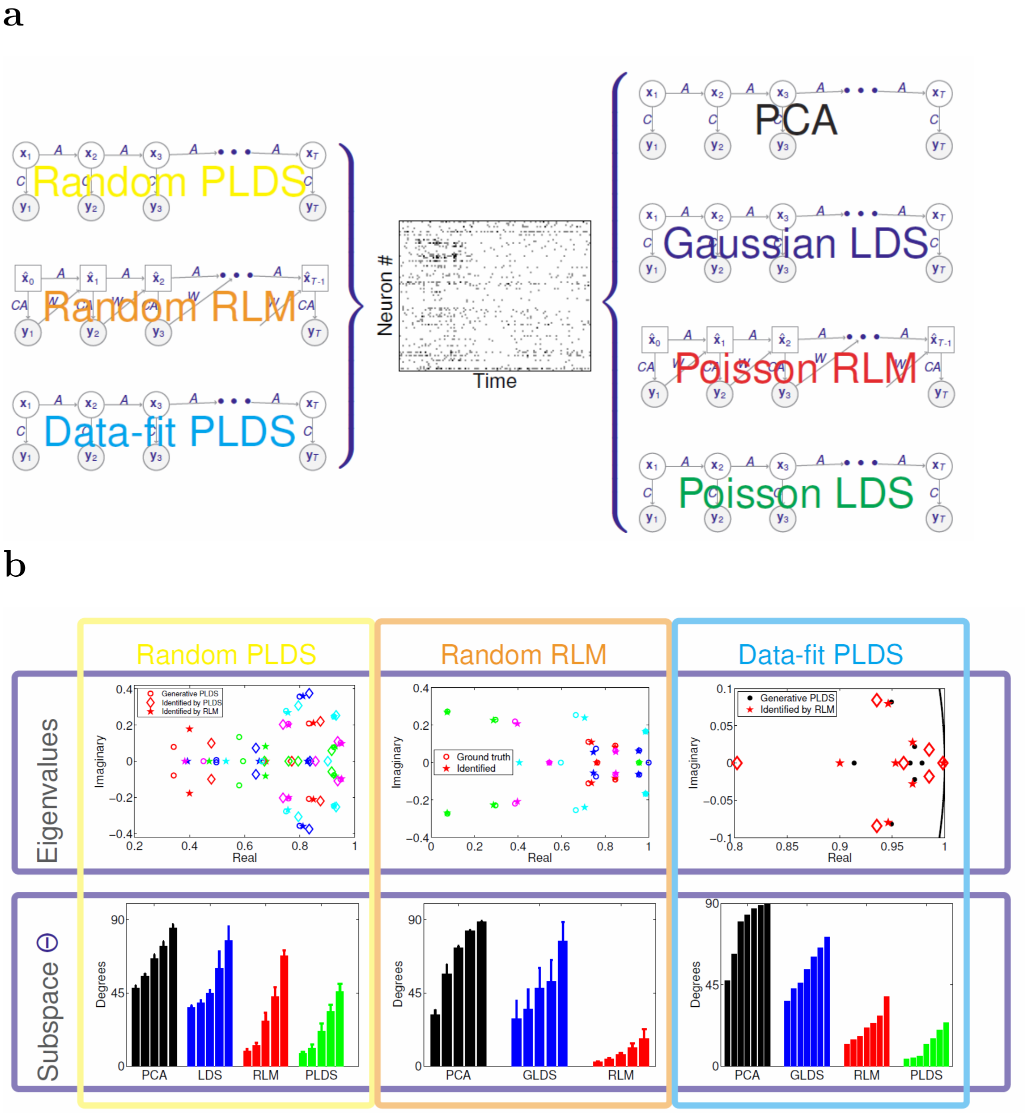

Figure 2.2: Experiments on simulated data. **a)** Shows a schematic of generating pseudo-data from diverse generative models, including a ground truth PLDS model, ground truth RLM model and a realistic PLDS model fit to array recordings. **b)** Shows the performance of the models at recovering eigenvalues of dynamics and underlying subspaces.

2.6 Results

2.6.1 Simulated data

We began by evaluating RLM models fit to simulated data where the true generative parameters were known. Two aspects of the estimated models were of particular interest: the phenomenology of the dynamics (captured by the eigenvalues of the dynamics matrix A) and the relationship between the dynamical subspace and measured neural activity (captured by the output matrix C). We evaluated the agreement between the estimated and generative output matrices by measuring the principal angles between the corresponding subspaces. These report, in succession, the smallest angle achievable between a line in one subspace and a line in the second subspace, once all previous such vectors of maximal agreement have been projected out. Exactly aligned n-dimensional subspaces have all n principal angles equal to $0°$. Unrelated low-dimensional subspaces embedded in high dimensions are close to orthogonal and so have principal angles near $90°$.

We first verified the robustness of maximisation of the gl-RLM likelihood by fitting models to data that were themselves generated by a known gl-RLM. Fig. 2.2b shows eigenvalues from several simulated RLMs and the eigenvalues recovered by fitting parameters to simulated data. The agreement is generally good. In particular, the qualitative aspects of the dynamics reflected in the absolute values and imaginary parts of the eigenvalues are well characterised. Fig. 2.2b shows that the RLM fits also recover the subspace defined by the loading matrix C, and do so substantially more accurately than either principal components analysis (PCA) or GLDS models. It is important to note that the likelihoods of LDS models with Poisson observations are difficult to optimise, and so may yield poor results even when fit to within-class data. In practice we did not observe local optima with the RLM or CLM.

We also asked whether the RLM could recover the dynamical properties and latent subspace of data generated by a latent LDS model with Poisson observations (PLDS). Fig. 2.2b shows that the dynamical eigenvalues of the maximum-

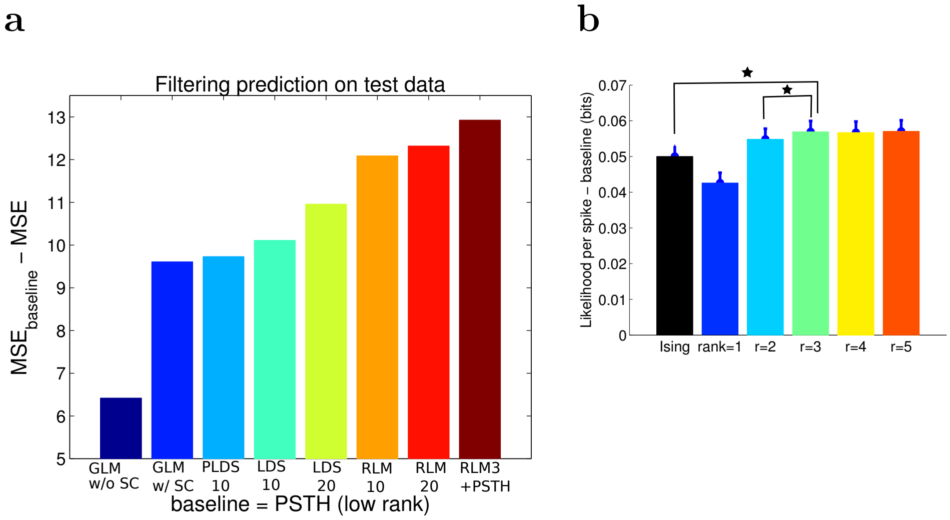

Figure 2.3: **a)** Perfomance on test data of the models that we evaluated (higher is better). GLM type models are helped greatly by self-coupling filters (which the other models do not have). The best model is an RLM with three latent dimensions and with a low-rank model μ of the PSTH. Adding self-coupling filters to this model further increases its predictive performance by 5 (not shown). **b)** The likelihood per spike of Ising models as well as CLM models with small numbers of hidden dimensions. The CLM saturates at three dimensions and performs better than Ising models.

likelihood RLM are close to the eigenvalues of generative PLDS dynamics, whilst Fig. 2.2b shows that the dynamical subspace is also correctly recovered. Parameters for these simulations were chosen randomly. We then asked whether the quality of parameter identification extended to PLDS models with realistic parameters, by generating data from a PLDS model that had been fit to a neural recording. As seen in figs. 2.2b the RLM fits remain accurate in this regime, yielding better subspace estimates than either PCA or GLDS.

2.6.2 Array recorded data

In this section we show that the two proposed models, RLM and CLM, better capture the statistical structure of spike trains than previous models. In particular, we compare the RLM to the GLM, LDS and PLDS and the CLM to the Ising model.

We used a dataset of 92 neurons recorded with a Utah array implanted in the premotor and motor cortices of a rhesus macaque monkey performing a delayed center-out reach task. For all comparisons below we use datasets of 108 trials in which the monkey is making movements to the same target.

We discretized spike trains in time bins of 10ms as the GLM has too many parameters and needs to be regularized in order to make good predictions on held-out test data. Figure 2.3a shows only the best cross-validation result for the GLM and the results without regularization for models with low-dimensional parametrization. The measure of performance we show in figure 2.3a is a causal mean squared error prediction subtracted from the error which a good model of the PSTH makes. We obtain the PSTH model by truncating at five dimensions an SVD decomposition of the individual trial-averaged PSTHs which have been smoothed with a Gaussian filter of standard deviation 20ms. The number of dimensions kept and the standard deviation of the Gaussian filter have themselves been cross-validated to find the best performance. In other words, we are assessing the model's ability to predict spikes on a trial by trial basis.

As another measure of performance for the RLM, we evaluated the quality of probabilistic samples obtained from the fully fitted model. Figure 2.5 shows averaged noise cross-correlograms obtained from a large set of samples. Note that the PSTHs have been subtracted out from each trial to reveal only the extra correlation structure that is not repeatable from trial-to-trial. Even with very few hidden dimensions, the model captures the full temporal structure of the noise correlations very well.

Since the Ising model requires binarized data, we replace all spike counts larger than 1 with 1. The log-likelihood of the Ising model can only be estimated for a small number of neurons, so for comparison we only consider the 30 most active neurons. The measure of performance reported in figure 2.3b is the extra log-likelihood per spike compared to a model that makes constant predictions equal to the mean firing rate of each neuron. The CLM model with only three hidden dimensions achieves the best generalization performance and surpasses the

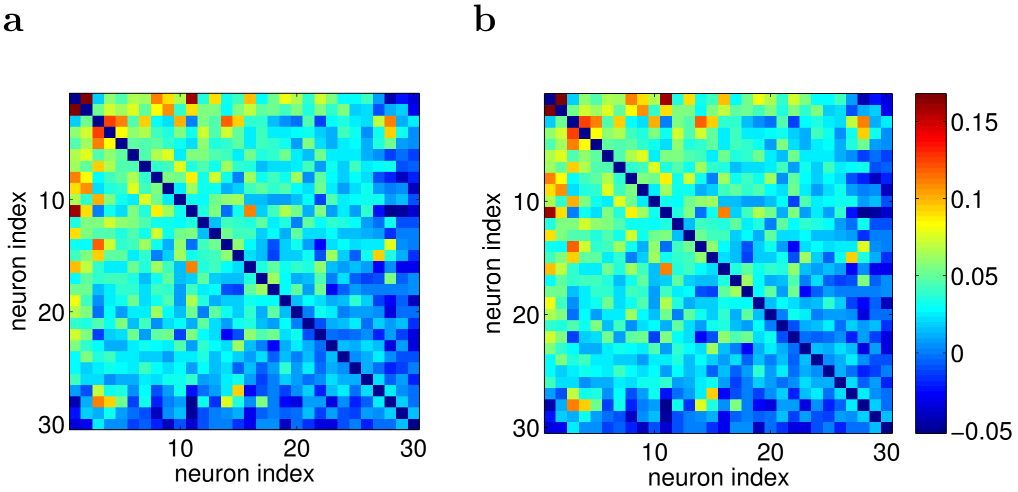

Figure 2.4: **Samples from cascaded linear model with 3 latent dimensions match the correlation structure of the real data**. **a)** Shows the true data pairwise correlations **b)** Shows pairwise correlations of samples drawn from the model distribution after fitting to the data.

Ising model. Similar results for the performance of the CLM can be seen on the full dataset of 92 neurons with non-binarized data, indicating that three latent dimensions suffice to describe the full space visited by the neuronal population on a trial-by-trial basis. Finally, figure 2.4 shows that samples drawn from a CLM model with only three dimensions almost perfectly captures the structure of pairwise noise correlations in the data.

2.7 Discussion

The gl-RLM model, while motivated similarly to the latent LDS model, can be fit more efficiently and without approximation to non-Gaussian data. We have shown that it yields superior performance on simulated data, as well as population recordings from the motor cortex of behaving monkeys. The model is easily extended to other output distributions (such as Bernoulli or negative binomial), to mixed continuous and discrete data, to nonlinear outputs, and to nonlinear dynamics. For the motor data considered here, the generalised-linear model performed as well as more completely non-linear versions.

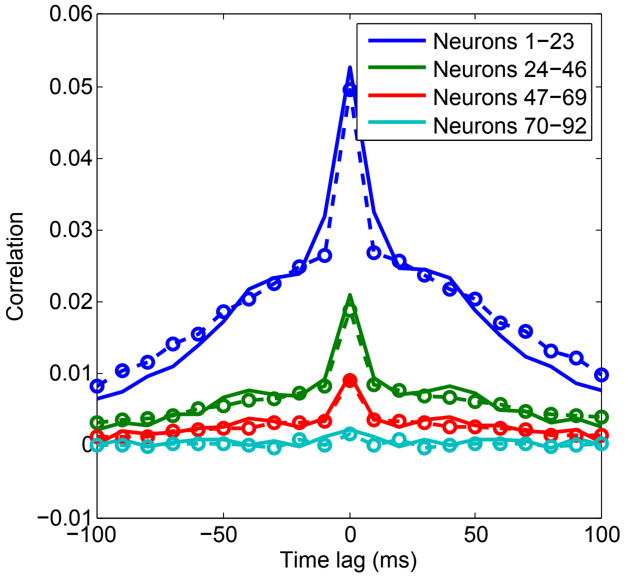

Figure 2.5: Samples from an RLM model resemble the (shuffle-corrected) cross-correlation structure of the data. Neurons were separated into four groups ordered by their total correlation and the average cross-correlograms within each group are shown. Continuous lines are the data and the model generated samples are in dashed lines. Although the peak at 0ms may be due to recording the same neuron multiple times on different electrodes, we have verified that in fact most pairs of units had such a peak and no two units had unproportionately large cross-correlation peaks, as would be expected for directly-connected neurons. Due to averaging over many pairs of neurons and trials, the error bars on the cross-correlograms were very small and are not shown.

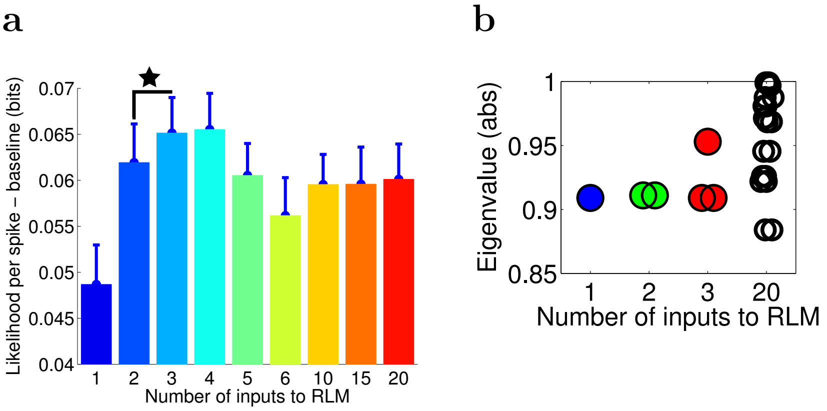

Figure 2.6: When a low-dimensional PSTH model (μ) is added to the RLM, log-likelihood saturates at a very small number of latent dimensions (three) and performs better than RLM and LDS models without PSTH terms. Without the PSTH model, we needed to use as many as ten or twenty latent dimensions to capture the full aspects of the data. Figure **b)** shows the magnitudes of the eigenvalues obtained with RLM3+PSTH. Most of the trial-by-trial variability is thus explained with timescales of 100 and 200 ms.

III

Recurrent linear analysis of multi-neuron recordings from motor cortex

Outline

We find two new single-trial correlates of hand movements in the motor cortex of primates. First, we show that trial-by-trial fluctuations in population responses during the delay period follow similar dynamics as those followed during actual movements. These fluctuations are concentrated in 100-200ms long dynamical events which activate the entire population. In one monkey, many of the fluctuations were associated with short movements that were very quickly stopped. Second, using a novel decoder of population activity, we find that one axis of neural dynamics controls the progression of movement. The neural activity along this axis correlated not only with reaction times but also with the fine details of movements like the shape of the speed profile. Our findings were made possible by new statistical and dynamical models of population neural activity which we developed, and their associated dynamics-based decoders of hand position. Using a model-derived estimate, we show that the redundant information due to correlated fluctuations across neurons drops by a factor of 50 to almost 0 during movements, indicating an almost complete lack of correlated fluctuations and a high degree of desynchronization in the responses. Such a desynchronized regime of neural dynamics might help cortex generate reliable and robust motor signals.

3.1 Neural dynamics in motor cortex

[1] In this chapter we analyze the dynamics of cortical populations recorded from motor cortex. Utah arrays were implanted into the motor cortices (primary M1

[1] The data used in this chapter has been generously made available by Krishna Shenoy and was recorded in his laboratory by Mark Churchland.

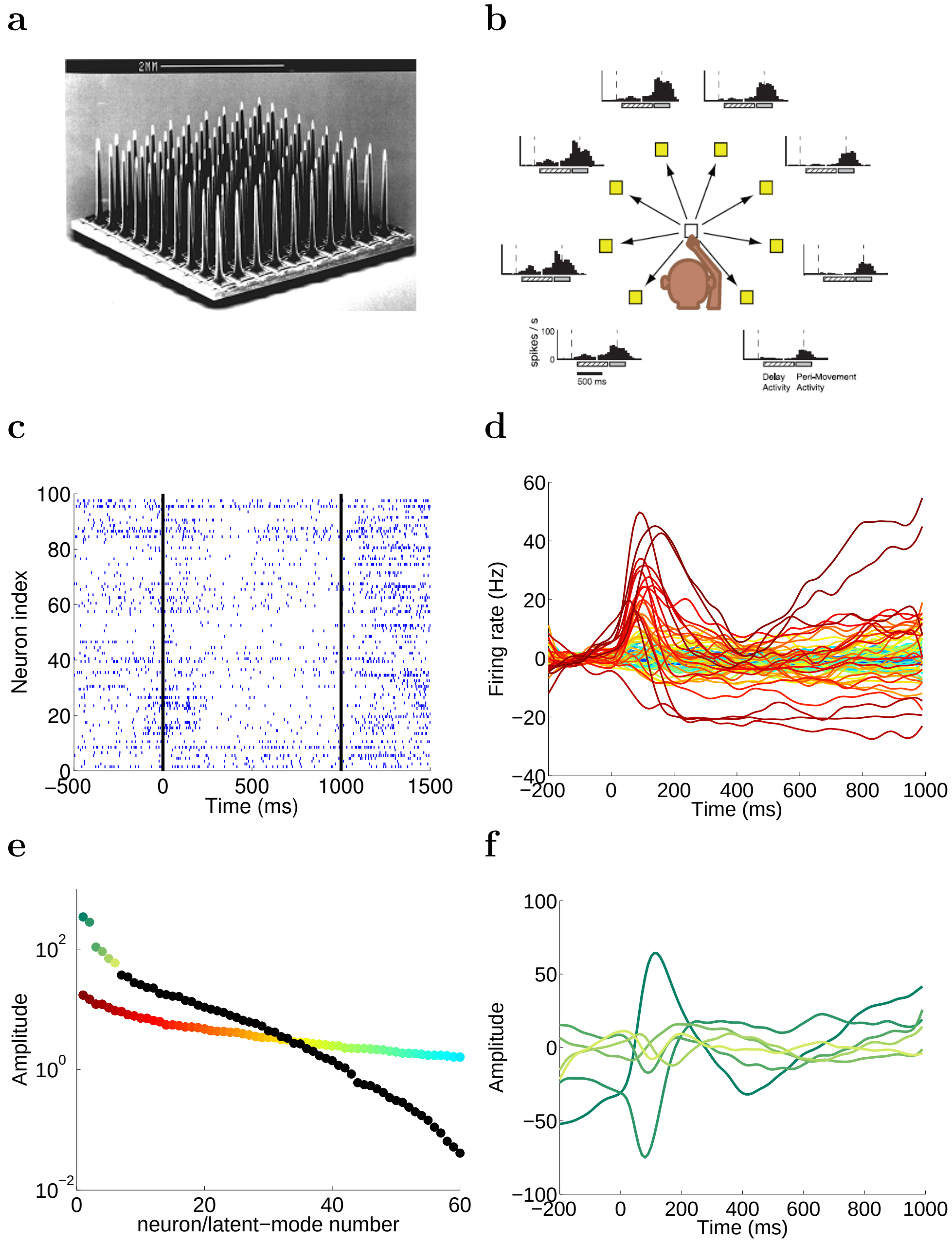

Figure 3.1: (Caption next page.)

Figure 3.1: **Example multi-neuron recording in motor cortex of primates.** **a)** Picture of the kind of Utah array implanted in motor cortex. **b)** Schematic of the delayed reach task to one of eight locations. **c)** Example array recording from a single trial of the task. Vertical bars indicate target onset and go cue onset. Rasters of 97 simultaneously-recorded neurons from a Utah-array implanted in the motor cortex of a rhesus macaque. **d)** Mean-subtracted firing rates over 108 repetitions of the same stimulus. Stimulus-onset at time 0 is followed by the delay period of one second. **e)** Singular value decomposition of PSTHs recover the principal temporal dynamics. The spectrum contains several singular values significantly large. The spectrum of white noise with equivalent power is also shown. **f)** The six temporal projections with largest singular values are shown. Together these account for over 95% of the variance of the population PSTHs.

and premotor dorsal PMd) of rhesus macaque monkeys (Fig. 3.1a). Animals were first trained to perform a delayed center-out task on a computer screen and became experts. Subsequent to array implantation, both neural activity and hand position were monitored during performance of the task. The task structure was designed to provide a number of advantages for neural recordings (Fig. 3.1b). First, the monkey had to initiate trials itself by holding its hand in the center of the screen and fixating on this center point. Following fixation, a target appeared while the monkey had to continue holding and fixating for a delay period. After this delay period, a go cue was displayed in the center and the monkey was allowed to move its hand to the target. Neural activity from a single trial (shown in figure 3.1c) corresponds to a target onset at time 0 and an ensuing delay period of one second. The Go cue appeared at time 1000ms and the monkey executed the reach with typical reaction times of $\sim$ 200ms. Neurons can be seen to have strong responses around stimulus onset (0 ms) and during movements (after 1000ms) but there is also ongoing activity during the delay period (0-1000ms). The peri-stimulus time histogram represents the stimulus-locked mean firing rates of neurons (Fig. 3.1d). It is already obvious from figure 3.1d that the major response features of neurons can be summarized succinctly from the PSTHs. Neurons that respond show firing rate increases at stimulus onset, after which they either get inhibited below their baseline, or start slowly ramping up their firing rates until the end of the trial. Although some variability exists in the dynamic shape of the stimulus-response, such PSTHs can typically be explained with very few dynamical modes. This would have not been the case for example if each neuron had their maximal firing rates at a different time during the trial, or if the increases and decreases in firing rates were less smooth in time and more temporally jagged.

We can decompose the dynamics of the PSTH using a singular value decomposition (SVD). Assume the firing rates of the neurons are represented in an array PSTH(nn, t) with nn the neuron number and t the time bin number. An SVD decomposition simply decomposes this matrix into PSTH $= USV$, with S a diagonal matrix of real singular values, U a matrix of orthogonal subspaces and V a matrix of orthogonal temporal trajectories. The singular values of S are sorted in order of their absolute magnitude, hence one can plot them as in figure 3.1, which shows that for this dataset, most of the variance in the PSTHs lies in the top two components, with perhaps additional significant variance in the next few components. Inspecting the timecourses of these dynamical modes in figure 3.1f reveals that indeed they mostly capture the patterns we have already pointed out in the previous paragraph.

This simplistic description of neural responses may be sufficient for some purposes, but ignores most of the recorded data. Our motivation in much of the work described here is to perform such low-dimensional analysis on single trials, and thus capture more detailed aspects of the neural responses.

3.2 Statistical models of delay-period activity extract consistent single-trial patterns

The peristimulus time histogram (PSTH) is useful for understanding neural responses under repeatable experimental conditions. However, the PSTH loses all single-trial information that might correlate with behavioral or perceptual variability. We would like to understand the trial-to-trial variability either as a consequence of different internal states, such as attentional states in sensory cortices,

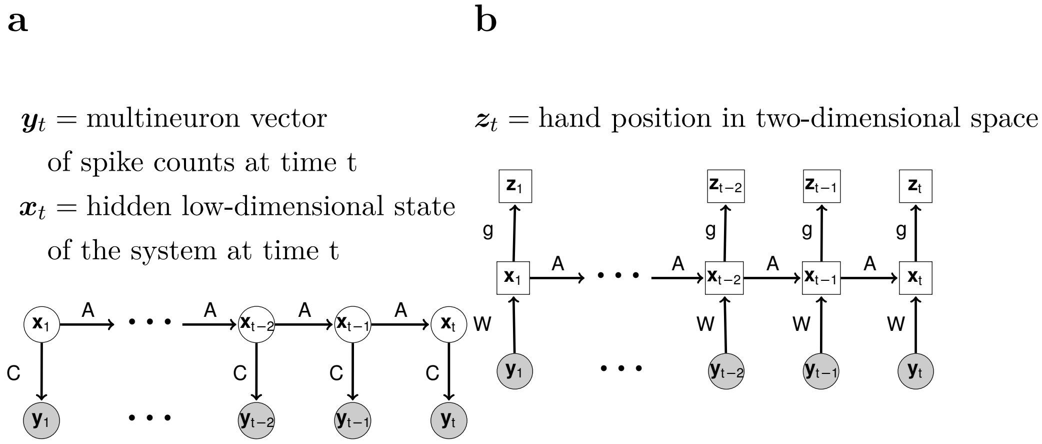
a
b
y_t = multineuron vector of spike counts at time t
x_t = hidden low-dimensional state of the system at time t
z_t = hand position in two-dimensional space
x1
xt−2
xt−1
xt
A
C
y1
yt−2
yt−1
yt
z1
zt−2
zt−1
zt
g
W

Figure 3.2: **Model structure.** **a)** Modelling framework for capturing trial-by-trial fluctuations in neural activity not controlled by the experimenter. The shading of the $\boldsymbol{y}_t$ nodes indicates that these are observed variables, while the underlying sources of fluctuations $\boldsymbol{x}_t$ are unobserved but we make the modelling assumption that they evolve with simple linear dynamics. This model is evaluated using a Kalman filter optimized for Poisson spike counts. **b)** Second modelling framework for capturing the dependence of hand position on spiking activity in M1. We use a decoder that incorporates low dimensional dynamics as before, but is driven exclusively by the observed data. The hand position $\boldsymbol{z}_t$ depends on the hidden states through a nonlinear function g that maps into the two-dimensional space of the hand location. The nonlinearity was parametrized as a one layer neural network with rectified linear units. The model parameters are fit from pairs $(\boldsymbol{y}_t, \boldsymbol{z}_t)$. On test data, the performance of the model is evaluated by computing the root mean squared error between the model's predictions and the actual reach trajectories.

or as a direct determinant of variable behavior, such as we might expect in motor cortex, where activity drives muscles and consequently enacts action. Such variability however is by definition not linked to the experimental conditions, therefore averaging over trials will cancel out the variability in neural responses. Hence, we need to analyze single-trial relationships between neural variability and behavioral events. Single-neuron recordings do not contain sufficient information to make single trial analysis feasible. Fortunately, large-scale recordings have recently made it possible to monitor the activity of sufficiently many neurons in motor cortex, that we might in principle understand the patterns of neural covariability from the single-trial population response.

In this work we focused on understanding and interpreting a reduced-dimensionality representation of the full array recordings (Fig. 3.2a). Our dimensionality reduction techniques are motivated from multiple observations.

First, we observed that a three-dimensional model of the shared covariability was sufficient to explain the patterns in the data. Models with higher dimensionality over-fitted to the training data, and did not increase the likelihood of the held-out data.

Second, concentrating all covariability into a small number of dimensions might allow us to track the typically small number of behavioral variables represented by motor cortex. In fact, we observed that most of the covariability in motor cortex in the delay period of the reach task could be accounted for by a single underlying trajectory that tracked the overall level of activation of the neural population (Fig. 3.3e). The main trajectory clustered neural single-trial fluctuations into events extended in time about 100 to 300ms (Fig. 3.3abc). The second and third trajectories tracked additional details of the spatial structure of these events and contained significant power (Fig. 3.3d). One might hypothesize that such large single-trial events would correlate with movements, and we show in the next section that, somewhat surprisingly, this was indeed the case in one monkey.

3.3 Delay period shared fluctuations are associated with micro-movements

Although the monkey was required to hold its hand in the center of the screen during the delay period, the effective allowed holding area was relatively large (Fig. 3.4d). Although typical movements required of the monkeys were about 10 cm, we found that during delay period activity the hand position shifted slightly in very brief hand drifts less than 1mm long that we call micro-movements (Fig. 3.4ef).

The micro-movements had a very stereotyped direction of drift towards the lower left direction for a monkey using its right hand. We found that these micro-movements were associated with large increases in the total activity of M1 neurons.

Furthermore, the micro-movements aligned in typical duration and onset with the events captured by our low-dimensional trajectories extracted from the array data. The micro-movement triggered multi-unit activity (MUA) had a prominent peak at a timelag of -30 ms (Fig. 3.4g).

We compared the population vector activated by the micro-movements to the population vectors of neural activity during distinct phases of the reaches. We found that the population vector activated during micromovements correlated highly to the population vector in M1 at the end of reaches (Fig. 3.4c).

This analysis suggests that the observed neural activity in M1 during micro-movements may either be of a sensory feedback origin, or sending a stopping signal to the arm to maintain fixation.

3.4 Fluctuations in M1 activity align with population patterns during movement

While we found a potential role for one of the three underlying trajectories, the question remains what the other two trajectories might be representing. We did a similar comparison as before with the population vectors during actual movements, but this time we compared them with the subspaces of neural covariability corresponding to the trajectories.

Like before, we found that one of the trajectories correlated strongly with the population vector at the end of movements. The other two also correlated with population activity during movements, but had maximal correlation at the onset and during movements respectively (Fig. 3.4ab). Together the three trajectories seemed to tile the temporal sequence activated during movements, suggesting that trial-to-trial covariability during the delay period actually activates the same subspaces of activity as those activated during movements.

This observation may be contrasted with recent reports by [Kaufman et al., 2014] showing that the PSTHs during the delay period activity actually span subspaces orthogonal to the movement subspaces. Note that the two observations are not incompatible: the average delay-period activity might be mostly tuned to the stimulus and/or showing an average preparatory activity.

However, responses varied significantly from trial to trial, and the PSTHs do not include information about this coordinated activity. We showed that the subspaces accounting for the variability on single trials do align with movement-related subspaces. In addition, sometimes the large single-trial neural events were associated with actual micro-movements of the arm, although many neural events did not result in movements.

3.5 Stimulus and movement onset drastically reduce mutual information in M1

It has been previously reported that stimulus and movement onsets in M1 reduce both single neuron variability across trials as well as noise correlations between pairs of neurons ([Churchland et al., 2010]). While the analysis of [Churchland et al., 2010] is suggestive of pervasive effects across cortex, the magnitude of the reduction has not been quantified in terms of the shared variability between neurons.

Our model provides an estimate of the redundant or mutual information in the population responses, as explained below, and we will use this quantity to track the total mutual information of neurons during the timecourse of the trial. Under the fully independent model of activity, all neurons would be spiking independently with firing rates determined completely by their baseline firing rate and self-coupling or refractory terms. At the other extreme, a fully-correlated model would have all neurons spiking at precisely the same times. In practice, as it can be seen in Fig. 3.1c, neurons tend to fire together a lot more than expected by chance from an independent model. Neurons tend to fire together during the brief 100-200ms events.

Given these correlations in firing, observing the activity of a subset of neurons provides information about the activities of the other neurons. This quantity is called mutual information and for high-dimensional variables it cannot be estimated exactly. However, an estimate can be achieved by computing the joint entropy of the distribution of neuron responses using a model. Since the true mutual information (MI) computation is intractable, we use the best available model (the RLM) to get a good lower bound. If a population of neurons is however driven by the same stimulus, then some of the mutual information between neurons will be information about the stimulus.

In analogy to noise and signal correlations, we define the noise MI as that portion of the mutual information between neurons that cannot be explained by time-locked responses to the stimulus MI_s = MI(x1,x2,s) - MI(x1,s) - MI(x2,s). The noise MI cannot be tractably estimated for large populations either, but model-based estimates can be obtained.

A lower bound of MI(x1,x2,s) can be obtained using an RLM model with driving inputs, such that each neuron receives an additional input that is a function only of time in the stimulus. We optimize these additional parameters to obtain our best estimate of MI(x1, x2, s). The RLM model performs best at estimating the noise MI, because it has the highest likelihoods on held-out data. The estimates of the mutual information between the neurons and the stimulus/movements are easier to compute since they can be estimated simply from smoothed PSTHs.

Tracking the noise MI over the timecourse of the trial shows that indeed stimulus and movement onsets reduced the amount of mutual information in the population (Fig. 3.3f), or at least our best estimate of it.

The shared covariability is reduced by a factor of 3 by stimulus onset, and by a factor of 50 by movement onset. Indeed, neural covariability is very small and close to 0 during the movements. This indicates all the inputs to the neurons are time-locked to the movements and no fluctuations in activity exist from other sources of input. The spatiotemporal patterns of neural responses during movements are thus reproducible from trial to trial, and much more so than the activity during the delay period of the task.

This is especially surprising since we do know some of the sources of neural covariability in M1 during movements: on every trial, the monkey performs the same reach with slightly different reaction times and speed profiles, which should be reflected in the neural responses.

Indeed we find that information does exist in the M1 responses that can be used to predict with high fidelity the trial-by-trial variations in hand trajectories (shown in the following section). The mutual information analysis suggests that this trial-by-trial covariability is in fact very small compared to that generated in the delay period of the task, where co-fluctuations dominate responses.

3.6 Comparison with noise correlation analysis

One might ask why we do not use noise correlations to describe population covariability over-and-above the PSTH instead of the noise MI. One advantage in using the noise MI is that it accounts for the shared mutual information between neurons over all timescales of activity, not just the arbitrarily defined temporal binning at which noise correlations are computed.

In addition noise correlations are always non-zero because they are estimated from finite data, even when the true noise correlations should be 0. The model-based noise MI can however be computed on test data not used for fitting the model and if the true noise MI is 0, then the model-based estimate cannot be significantly different from zero. As a note of caution, the noise MI will in general underestimate the true mutual information, as we discussed before. By using well-performing models we can attempt to bridge the gap between the estimate and the true value.

A further disadvantage of using the noise correlations is that all pairs of neurons are considered equal in the histogram. However, the low-firing neurons will have poorly estimated noise correlations. Even if the noise correlations were estimated perfectly, for an equal noise correlation, high-firing pairs of neurons will have large mutual information while low-firing neurons will have a small amount of mutual information, simply because high-firing neurons have larger information capacity in their spike trains. Large amounts of mutual information will in turn better reflect the underlying unobserved processes that correlate neurons.

3.7 The fine details of movements are encoded by motor cortex

Although the amount of noise mutual information between neurons is small during movements, we found that covariability in responses can be used to predict hand position on a trial-by-trial basis.

To capture the transformation between motor cortex and hand position we trained a decoder that accumulated information from the spikes into a hidden dynamical system that evolved with linear dynamics (Fig. 3.2b).

The hidden dynamical system representation was then used to predict hand position within the same time step, via a nonlinear one-layer neural network. The nonlinearity was necessary to convert the representation from a linear representation of M1 activity to the highly nonlinear mapping of space implicit in the muscles and joints of the arm. We fit this transformation model using standard backpropagation through time techniques.

The resulting model captured the relevant information from the M1 spikes into its low-dimensional internal representation. Further below we study this internal representation in order to understand what the relevant M1 information is, but first we show that the decoder captured trial-by-trial variability in movements.

We studied the performance of the decoder on held-out data (Fig. 3.5a). The decoder with 10 hidden states achieved an average root mean squared error of 6.5mm during movements. The decoder was able to perfectly predict the reach direction from M1 activity. However, an error of 12mm was achieved by a decoder that only perfectly predicted reach direction and then predicted the average path from the training set for that reach. It follows that our decoder must be capturing additional trial-by-trial variability over-and-above the reach direction.

To further show this point, we shuffled the held-out data such that the reach condition remained the same but the hand trajectory was chosen from another trial of the same reach randomly. The trained decoder only achieved 13.9mm error on the shuffled set.

One primary determinant of root mean squared (rms) error on the test trials was reaction time. To see if the decoder predicted features of movement beyond just the reaction time, we shuffled the data again but aligned the randomly drawn reach path so that its reaction time was equal to the reaction time of the trial from which neural data was used in the decoder. The decoder only achieved 8.75mm rms error on this shuffled dataset. It follows that while reaction time is an important factor for good decoding from M1, additional single-trial movement features were also captured by the decoder.

Inspecting the reaches on the test set we were able to find another major contributor to movement variability, namely the speed profile of the reach (Fig. 3.5C). Various features of the speed profiles are captured by the decoder, for example some reaches have narrow peaks around the maximum speed of the reach and the decoder captures these peaks, while other reaches have more flat and constant maximum speed.

3.8 What information from the population spiking does the decoder use?

Next we analyzed the hidden trajectories computed by the decoder in order to understand what features of the spiking were important to drive good motor predictions.

Although we trained a 10 dimensional decoder, we found that most of the variance of the hidden space was concentrated in only 3 components (Fig. 3.5e). 3D plots of this three-dimensional subspace gave us an understanding of the model's internal representation.

Two of these three dimensions had very long integration timescales (>1s) and effectively accumulated information about the two-dimensional direction of the reach (Fig. 3.5d). The two-dimensional plane also encoded significant lateral deviations from the desired reach direction. To our knowledge, such a simple two-dimensional representation of reach direction has not been shown before in M1. It is especially noteworthy to mention that the same two-dimensional projection encoded the same reach direction before and after movement onset.

To directly test the influence of neural spiking on the decoded movements, we added perturbations in the two dimensional hidden space along two orthogonal directions (Fig. 3.6ab). The perturbations biased the reaches significantly towards the direction represented by the perturbations, but left relatively unaffected the other details of the movements, like end point of the trajectory and the speed profile. What then stopped the hidden trajectories from generating movements before movement onset? In fact, the third dimension of the hidden state did not evolve at all before movement onset, and grew monotonically after onset (Fig. 3.5e). This dimension had a much shorter timescale of 200ms, on the order of the duration of the movement.

We hypothesized that this dimension controlled not only movement onset, but also the overall progression of movement during reach. Faster rates of increase in the latent trajectory would correspond to faster progression in movement space.

To test this hypothesis directly, we added small positive perturbations in the latent trajectory at various times during the movement, and analyzed the resulting direction of the perturbation in movement space (Fig. 3.6c).

Depending on the reach direction and hand position in space, positive perturbations in the third trajectory always advanced the hand position towards the correct target, resulting in a radial pattern of perturbations in movement space.

To our knowledge, this is the first evidence that motor cortex tracks the progression of movement and does so in a relatively straightforward fashion, controlled only by the cumulative projection of M1 spiking onto a single linear subspace.

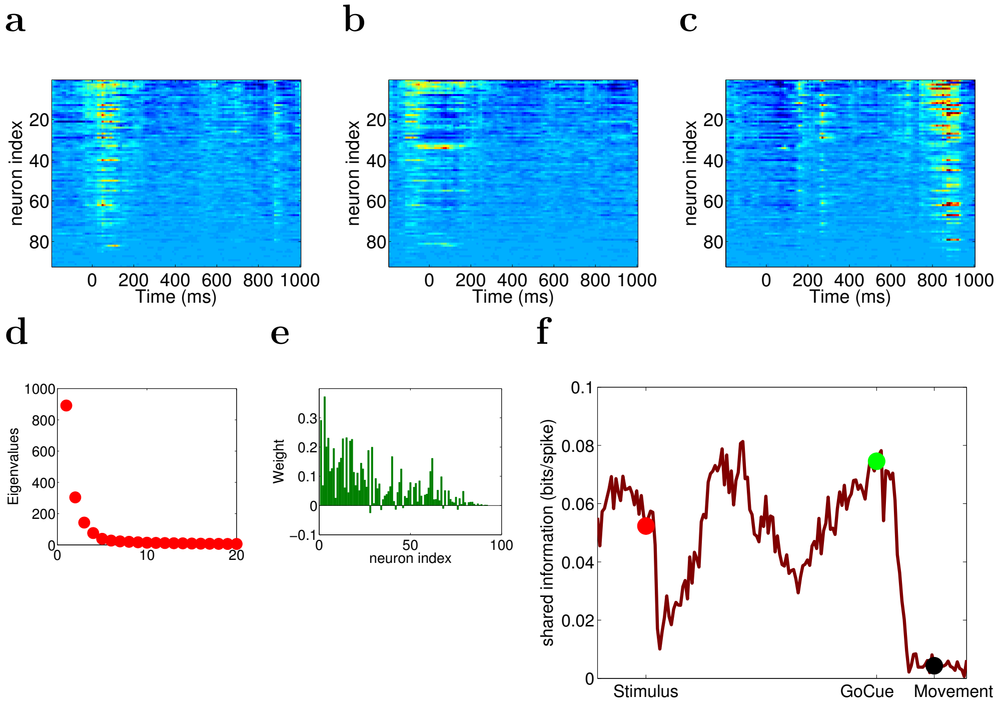

Figure 3.3: **Trial-by-trial variability in the delay period. abc)** Three examples of noise residuals in the delay period. For each neuron at each time point we plot the increase or decrease in probability of firing compared to the PSTH, predicted by the model based on past spiking. Neurons are sorted by their mean firing rates. **d)** Computing the SVD decomposition of all residuals, we see that most variability is in the first three dimensions of population activity. **e)** The singular vector associated with the largest singular value shows that most of the variability comes from correlated increases and decreases in the firing of most neurons. Furthermore, these increases tend to be proportional to firing rate (neurons are sorted by mean firing rate on the x-axis). **f)** Model-based estimate of the noise mutual information at each timepoint. This quantity is a measure of how much neurons co-fluctuate over-and-above the PSTH. There are sharp drops in the mutual information just after stimulus and movement onsets. Notice that the estimated mutual information during movements is very close to 0.

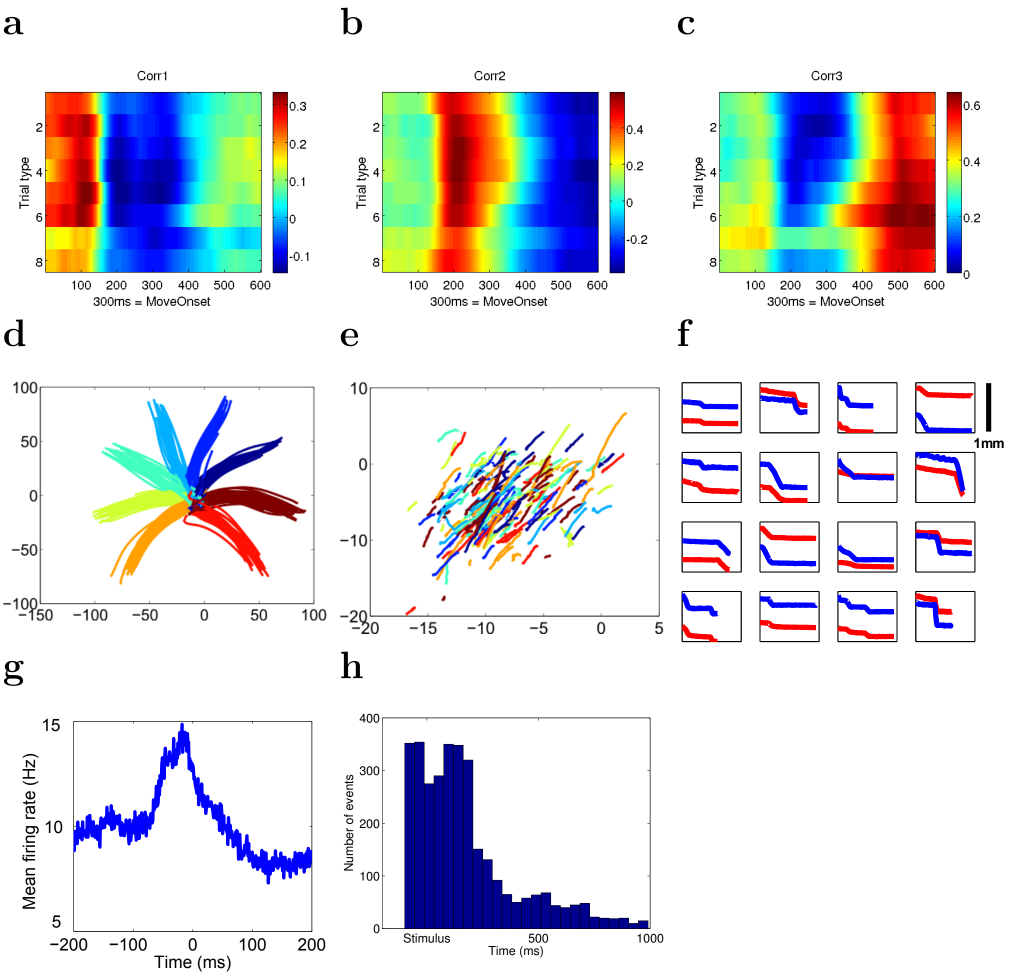

Figure 3.4: **Movement slips in the delay period correlate with neural events. abc)** All three dimensions of covariability in the delay period correlate with the population vectors during movements, at different delays. Third dimension of covariability correlates with the population vector during stopping at the end of the reaches. **d)** Subsets of movements to the eight targets. **e)** Zoom in of the center holding area and movements restricted to the delay period. Stereotypical small drifts in the south-west direction are now apparent during holding. **f)** (X,Y) position as a function of time for several delay periods. **g)** Averaged MUA aligned to the micro-movements. Rise in neural activity 50ms before a micromovement could imply a causal relationship between neural activity and behavior. **h)** Histogram of micro-movement times. Most micro-movements are triggered by the stimulus. The rate of micro-movement occurrence decays during the delay.

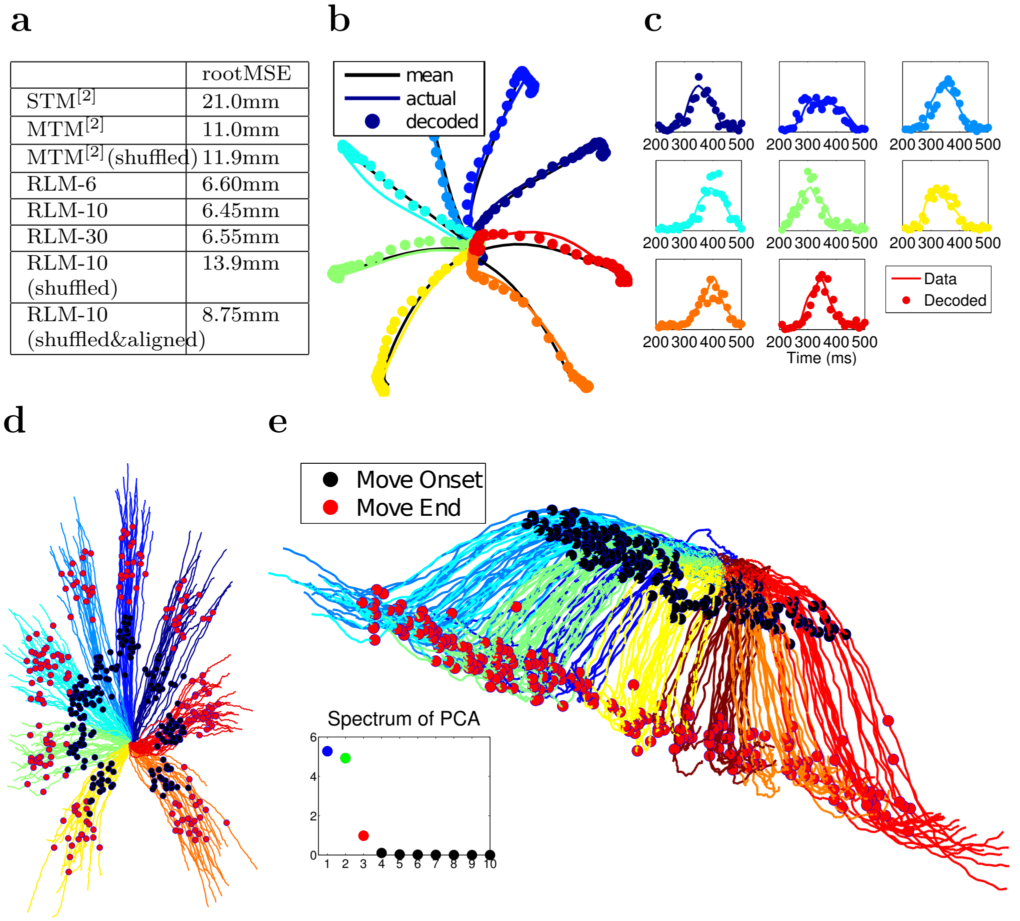

	rootMSE
STM[2]	21.0mm
MTM[2]	11.0mm
MTM[2] (shuffled)	11.9mm
RLM-6	6.60mm
RLM-10	6.45mm
RLM-30	6.55mm
RLM-10 (shuffled)	13.9mm
RLM-10 (shuffled&aligned)	8.75mm

Figure 3.5: **Single-trial decoding during reaches. a)** Root mean squared error results compared to previous state-of-the-art decoders on the same dataset, as well as results under various shuffling manipulations. **b)** Example decoded trajectories on held-out data, one for each direction of movement. Note the initial downward direction of the orange trajectory is decoded successfully. **c)** Examples of speed profiles of actual and decoded movements, one for each reach direction. Note the decoder captures not only reaction time variability, but also other shapes of the speed profile like the peakiness/flatness of the profile. **d)** Top view of the three-dimensional manifold tracked by the decoder during reaches. Colors like before. **e)** Side view of the same manifold.

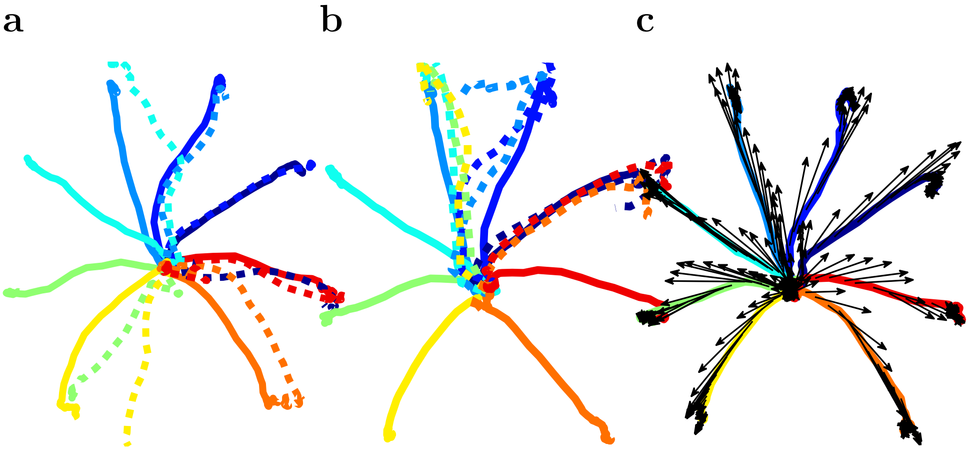

Figure 3.6: **Effect of perturbations on decoder.** Example perturbations at the onset of movements, in the two-dimensional plane that controls movement direction. **a)** Partial rightward perturbation. **b)** Upward perturbation. **c,** Perturbations in the third/oblique plane of the side view. At various points during movement the perturbation always has the effect of advancing the decoded trajectory forwards. Notice this is a highly nonlinear effect enabled by the nonlinear decoding step in the one-layer neural network represented by the function g.

IV

Quiescence in neural circuits enhances coding of continuous sensory streams

Outline

Animals immersed in their natural environments receive a continuous stream of sensory inputs. In passive animals, the sensory stream is corrupted by intrinsic large-scale fluctuations in neuronal activity. In the presence of ongoing fluctuations, neural responses to isolated sounds can still be robustly-triggered, but during continuous streaming stimulus information is lost. Here we identify and characterize a cortical state termed quiescent in which ongoing fluctuating activity is much reduced, while neural responses to continuously streaming stimuli are sparse, stable and high-dimensional. Putative inhibitory cells had two-fold activity increases relative to putative pyramidal in quiescent when compared to fluctuating states. We show that models of inhibition-dominated networks of neurons reproduce the coding benefits of quiescent states. However, when such model networks are insufficiently stabilized by negative feedback, they develop macroscopic chaotic behavior that we show is similar to the patterns of population-wide fluctuations present in fluctuating neural activity. Quiescent brain states are especially well-suited to encoding the fine patterns of sounds during continuous sensory stimulation and can encode tens of thousands of auditory stimuli. Recent experimental evidence suggests that the inhibition-dominated coding regime we analyze here may be employed in active and task-engaged animals.

4.1 Fluctuations exist and can be quenched in active states

[1] Population-wide fluctuations in neural excitability on multiple timescales are widely documented in neural recordings ranging from intracellular recordings to large-scale imaging[Constantinople and Bruno, 2011, Okun et al., 2012, Atencio and Schreiner, 2013, Beltramo et al., 2013b]. Intracellularly, fluctuations resemble spontaneous transitions from resting to hyperpolarized membrane potentials for durations of a few hundred milliseconds. In sensory areas, they give rise to positive noise correlations which impair coding[Luczak et al., 2009, Rothschild et al., 2010b, Sakata and Harris, 2009]. However, correlations are reduced when animals engage in tasks[Cohen and Maunsell, 2009, Gu et al., 2011]. Similarly reduced is the overall rate of ongoing activity in auditory cortex when animals are performing a task using that sensory modality. Ongoing fluctuations and overall firing rates are also reduced in auditory cortex when animals are running or vocalizing[Schneider et al., 2014, Eliades and Wang, 2008]. Enhancements of intracortical inhibition have been shown to improve coding of stimuli in anesthetized animals[Cardin et al., 2009, Hamilton et al., 2013]. Interestingly, it has been shown recently that awake and active states are characterized by significantly increased inhibitory conductances, which we propose here are an active network mechanism for quenching network excitability[Schneider et al., 2014, Haider et al., 2013, Kimura et al., 2014].

4.1.1 Hypothesis of unstable network activity

We hypothesized that random population fluctuations are caused by unstable recurrent network activity. The dynamics of neurons in unstable networks can amplify small perturbations exponentially and thus cause the whole network to activate spontaneously. Precise stimulus responses in unstable networks are not

[1] The work described in this chapter has been done in collaboration with Nicholas Lesica, Carsen Stringer, Jose Garcia-Lazaro and Dmitry Lyamzin. Nick, Jose an Dmitry expertly performed all experiments analyzed here. Carsen helped to develop and implement the network simulations.

possible, because a single exponentially amplified mode of network activity dominates the spatio-temporal structure of population responses. Stimulus-selectivity of ascending thalamic fibers is thus lost because neurons tuned to the stimulus activate many other neurons with no direct thalamic inputs.

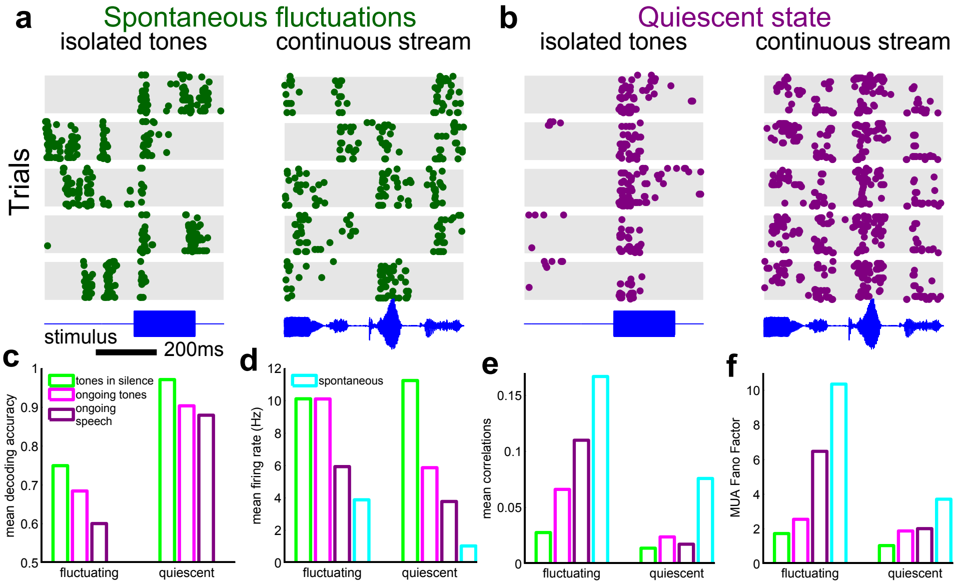

Figure 4.1: **Quiescent states respond reliably to continuous streams of sound.** Population rasters of recordings during stimulus presentations of either isolated sounds or a continuous stream of speech in either (**a**)) spontaneously fluctuating states or (**b**)) quiescent states. **c)** Decoding accuracy for both states for different types of stimuli. **d)** Mean firing rates of recorded neurons in both states and for different stimuli and during spontaneous activity. **e)** Pairwise noise correlations in stimulus responses or spontaneous correlations. **f)** The Fano Factor (variance divided by mean) of the multi-unit activity (MUA).

Unstable population activity can particularly hurt coding under the demands of active ecological behavior in a continuously streaming sensory environment. Intuitively, errors in neural responses to stimuli can accumulate over time, especially in areas such as auditory cortex where synaptic depression is known to significantly affect neural responses for hundreds of milliseconds.To test our predictions and further characterize the stability of neural network dynamics, we recorded spiking neural activity from auditory cortex under a fluctuating brain state and a quiescent brain state. The quiescent state was characterized by not only reduced mean firing rates both in spontaneous activity and in response to sounds, but also the complete abolishment of population-wide fluctuations during auditory stimulus presentation.

4.1.2 Fluctuating states do not code well in ongoing stimulation, but quiescent states do

Tones preceded by silence typically elicited responses from neurons in spontaneously fluctuating populations (Fig. 4.1a). However, responses failed to timelock to auditory events when tones were presented in quick succession every 150ms, or when a continuous stream of speech was played. Decoding accuracy in fluctuating states dropped as the complexity of the sound stream increased and the mean firing rates were also reduced (Fig. 4.1c and 4.1d). Pairwise noise correlations in response to stimuli progressively increased from 0.02 for isolated tones to 0.07 for streaming tones and 0.11 for ongoing speech, almost reaching the level of spontaneous correlations of 0.16 (Fig. 4.1e). The Fano Factor of the summed multi-unit activity showed a similar progression, indicating a large amount of variability in trial-to-trial evoked activity during ongoing stimulation (Fig. 4.1f). Neurons in quiescent populations also showed robust responses to tones preceded by silence, but in this case the spontaneous activity preceding the evoked response was also much reduced (Fig. 4.1b,d). Quiescent states also responded reliably and reproducibly to continuously streaming sounds (Fig. 4.1b). Coding capabilities were much enhanced overall when compared to the fluctuating populations and the drop in response reliability from isolated tones to continuous sounds was less pronounced (Fig. 4.1c,e,f) .

4.1.3 Possible mechanisms underlying quiescent states

What might produce the large discrepancies in stimulus responses between the two states? We hypothesized that the quiescent state was dominated by stabilizing negative feedback, both in the form of inhibition and short-term adaptation. The spike shapes of electrically recorded action potentials were clearly varying in spike width, and the trough-to-peak duration showed a clear bimodal distribution on the basis of which we classified cells as fast-spiking FS and regular-spiking RS (Fig. 4.3a). We found that the number of recorded FS units in the quiescent state doubled when compared to the fluctuating state, presumably reflecting their enhanced activity and increased detection rates with extracellular array recordings (Fig. 4.3b). The overall ratio of mean FS to mean RS activity correlated negatively with the level of mean noise correlations, such that populations with relatively more FS activity showed the least variability in responses (Fig. 4.3c).

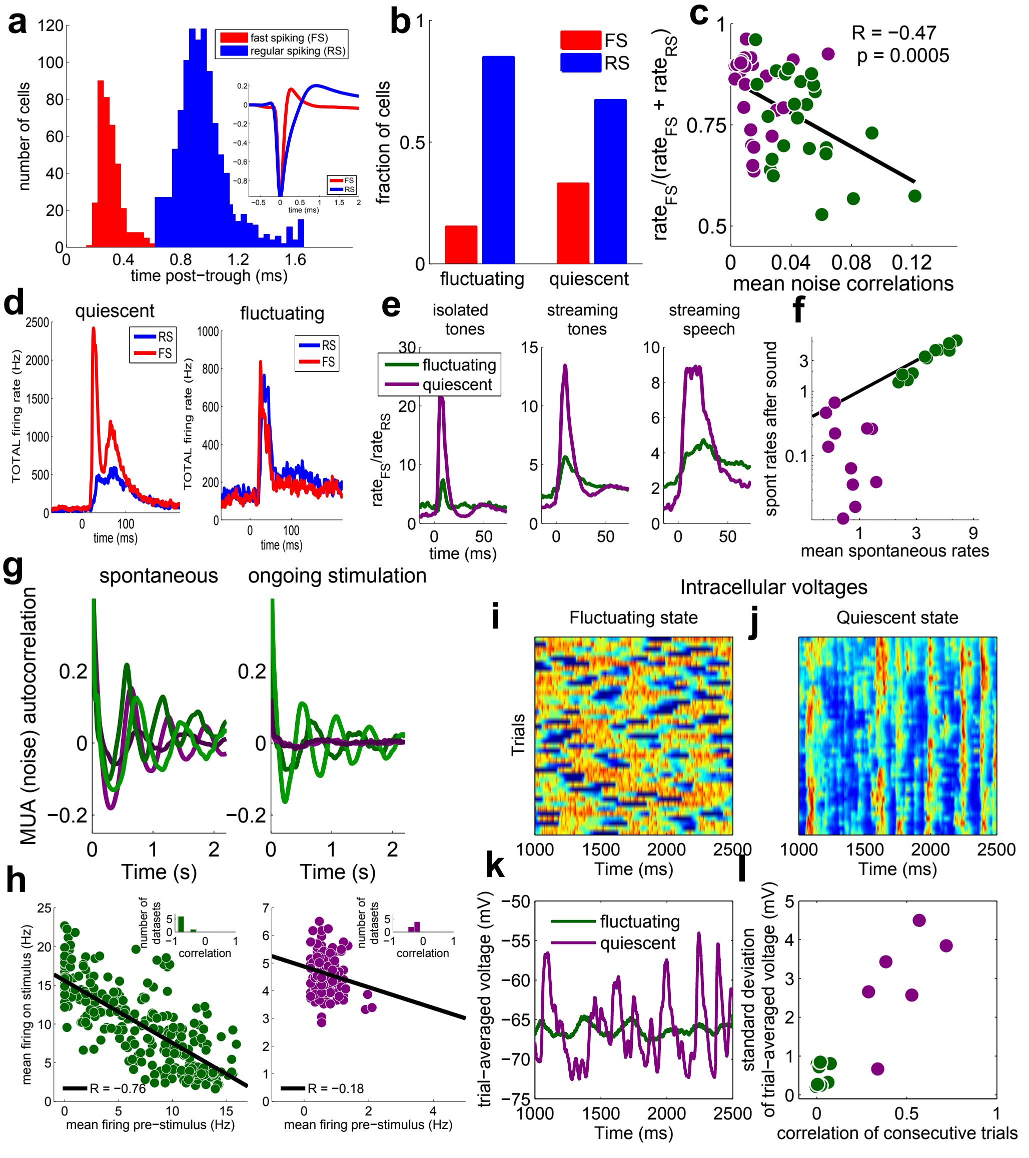

Figure 4.2: (Caption next page.)

Figure 4.3: (Previous page.) **Potential mechanisms for quiescent states: inhibition, adaptation and EPSP amplitude. a)** Putative inhibitory cells are classified based on their narrow spike waveforms. Spike width was measured as the trough-to-peak duration.**b)** The fraction of detected FS cells was twice greater in quiescent states. **c)** Ratio of FS to RS activity correlates negatively with the mean noise correlations. **d)** Example tone responses in quiescent and fluctuating states. **e)** Ratios of firing rates between FS and RS cells at stimulus-onset are greatly amplified in quiescent states. **f)** Spontaneous firing rates in quiescent states are suppressed for 500ms after stimulus presentation compared to mean rates in ongoing silence. **g)** Autocorrelation of the (PSTH-subtracted) MUA in (driven) and spontaneous activity. **h)** The firing rate in 500ms windows before stimulus onset affected the magnitude of stimulus responses in fluctuating but not in quiescent states. **ij)** Intracellular voltages in quiescent and fluctuating states. **k)** Trial-averaged voltages in fluctuating and quiescent states. **k)** Standard deviation of trial-averaged voltage plotted as a function of the similarity between continuous trials for 8 cells recorded in fluctuating states and 7 cells recorded in quiescent states.

Tones preceded by silence evoked large responses in FS and RS cells in both quiescent and fluctuating states, but the onset of the responses showed much larger activity in FS cells in quiescent state (Fig. 4.3d and e). The onset FS activity appears to be optimized to activate at very short latencies, perhaps by direct thalamic drive, and might thus serve to stabilize and sparsify the rest of the sensory-evoked response in the local neural population.

A second source of stabilizing negative feedback that has been documented in auditory cortex is short-term adaptation[Wehr and Zador, 2005, Destexhe et al., 2003]. We observed that firing rates in quiescent states were suppressed relative to spontaneous rates for hundreds of milliseconds after the stimulus was turned off (Fig. 4.3f). Similarly, the temporal autocorrelation of the spontaneous multi-unit activity showed oscillatory activity at typical delta band frequencies 1-2Hz but these were time-locked to the ongoing stimulation in quiescent states (Fig. 4.3g). In fluctuating states, the level of activity preceding a stimulus correlated negatively with the number of evoked spikes, showing that ongoing activity can suppress the sensory response over hundreds of milliseconds (Fig. 4.3h). The relationship did not hold in quiescent states, which had very low levels of ongoing activity, thus insufficient to cause depression (Fig. 4.3h).

4.1.4 Intracellular voltages

We performed in vivo intracellular recordings to better understand the underlying variability in membrane potential dynamics. We found that in both types of states the membrane potential underwent large excursions between hyperpolarized and depolarized levels, but in quiescent states these excursions were tightly locked to the ongoing stimulation (Fig. 4.3i, j). The trial-averaged membrane potential was modulated far more by the stimulus in quiescent compared to fluctuating states and upward stimulus transients were also larger (Fig. 4.3k). The temporal responses were similar in consecutive trials in quiescent states but quite dissimilar during ongoing fluctuations (Fig. 4.3l).

4.2 Deterministic network model reproduces the inherent randomness of fluctuations

We proceeded to verify in a neuronal network model that increased negative feedback can stabilize intrinsically fluctuating activity. The architecture of the model is described in Fig. 4.4a. Despite the wealth of studies of oscillatory and fluctuating networks, typical models do not capture the intrinsically random aspect of fluctuations. Even though on average population events last 200-300ms, the duration of an event can last anywhere from 50 to 1000 ms (Fig. 4.4b). Similarly the quiet periods between events can last for a variable interval of time, and these durations cannot be predicted on the basis of previous neural activity (Fig. 4.4c). To further exemplify the randomness of the fluctuations, we found matched segments of neural activity that underwent similar patterns of fluctuations for at least 3 seconds (Fig. 4.4f). The dynamics of these matched segments quickly diverged after the 3 matched seconds, indicating a high-degree of variability and potentially chaos in the timecourse of the fluctuations.

We constructed a network model with strong recurrent excitation, but relatively weak inhibition, which reproduced the spontaneous patterns of network fluctuations we observed in the data (Fig. 4.4a). The network exhibited long timescales

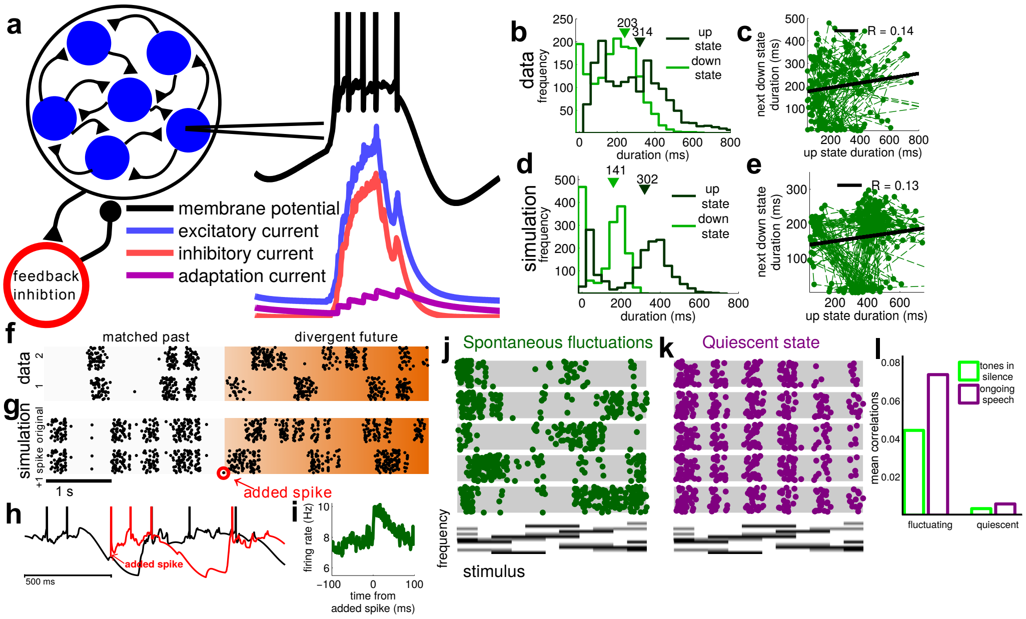

Figure 4.4: **Increased inhibition reproduces transition from fluctuating to quiescent states in network simulation. a)** Schematic of network architecture used throughout. **b)** Example distribution of up vs down state durations measured from the multi-unit activity. **c)** Down state duration plotted as a function of previous up state duration. **de)**, Same as (**bc)**) but for data simulated from the model. **f)** Two example periods of spontaneous activity matched for the first two seconds of the rasters. **g)** Adding a single spike during a simulation completely changes the future behavior of the network. **h)** Example simulation of the membrane voltage with added spike. **i)** Trial-averaged firing rates of neurons in the network after adding one spike to ongoing spontaneous fluctuations. **jk)** Population rasters for fluctuating and quiescent simulations in response to stimulus inputs. **l)** Noise correlations in simulations with isolated and streaming sounds.

of fluctuations, owing to adaptation currents in single neurons, but importantly these fluctuations came at random intervals, despite the lack of external sources of variability (Fig. 4.4d,e). In other words, the network produced its own variability through deterministic chaotic behavior, and such a behavior was unavoidable in networks with weak feedback inhibition. A single spike added randomly during ongoing spontaneous activity almost always changed the time course of the fluctuations, in some cases triggering population-wide events (Fig. 4.4g). Replicating a recent in vivo experiment[London et al., 2010], a single inserted spike was amplified into many more network spikes before the recurrent activity was shut off (Fig. 4.4i). Responses to stimuli were not reliable across repeated presentations, but were more reliable when stimuli were presented after prolonged silence (Fig. 4.4j,l).

4.2.1 Inhibition stabilizes network activity

We were able to stabilize the fluctuations in network activity by increasing inhibitory feedback, such that the spontaneous activity was much reduced but stimulus-driven activity was time-locked to the auditory stream and exhibited near-zero trial-to-trial noise correlations (Fig. 4.4k). We could stabilize the network either by increasing the inhibitory feedback gain or by adding tonic inputs to inhibitory neurons. The network responded with equal reliability to isolated sounds and to ongoing continuous streams of inputs (Fig. 4.4l). Adding a single spike during evoked activity did not cause an outburst of spikes in the rest of the network, but instead slightly inhibited network activity. Adding sufficiently many spikes eventually shut down activity briefly due to the strong non-selective feedback inhibition.

4.3 Quiescence enables sharp tuning, high-dimensional stimulus response and temporal integration

Tuning curves to sound frequency in quiescent states had on average half the width of the tuning curves in fluctuating states and these were reproduced in our network simulations of the two states (Fig. 4.5a). The more precisely tuned neural responses in quiescent states enabled high decoding accuracy in a decoding task with 29,040 different stimuli, where we pooled the responses of all neurons recorded in quiescent states (Fig. 4.5b). To achieve good decoding accuracy in this task at least 10-20 neural dimensions of activity were needed, indicating that the high-dimensional population activity can encode high-dimensional stimuli (Fig. 4.5c).

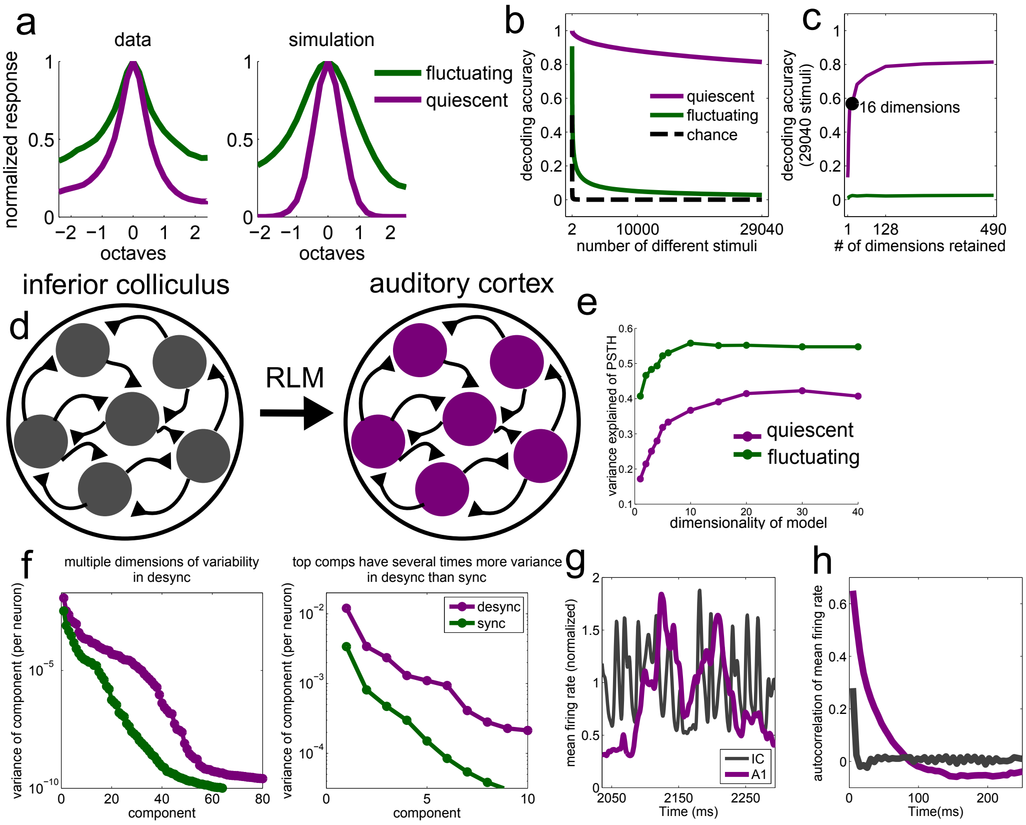

Figure 4.5: **Quiescent states enable network to use high dimensions for coding. a)** Aligned and population-averaged tuning curves to sound frequency in data and simulations. **b)** Decoding accuracy of up to 29040 stimuli. Training stimuli were selected as continuous 250ms long periods during a long ongoing speech stimulus. Test stimuli were selected from a second repetition of the speech stimulus. **c)** Decoding accuracy with 29040 stimuli as a function of dimensions of population responses retained. **d)** Schematic of a statistical model capturing the transformation of subcortical spiking inputs into cortical spikes. **e)** Percent variance explained of the PSTH by RLM transformation in a test dataset. **f)** Absolute variance captured by identified components of RLM transformation. **g)** PSTH of MUA of the inferior colliculus and auditory cortex in response to sounds without temporal structure. **h)** Autocorrelation of MUA in response to 180 seconds of ongoing sounds without temporal structure.

We related evoked cortical responses to long segments of ongoing speech to evoked responses to the same stimulus in the subcortical auditory pathway in the inferior colliculus. We used a statistical modelling approach which can fit dynamical models directly to data (Fig. 4.5d). We assumed the feedforward projection from the level of IC and through thalamus becomes input to a set of reduced-dimensionality neural network dynamics in cortex, from which the recorded cortical neurons are sampled sparsely. This model was fit directly to the data using the statistical framework we developed in the previous chapters (the recurrent linear model, RLM). The RLM accounted for more variance of the responses compared to a direct feedforward model, and also accounted for more variance compared to a more classical spectrotemporal model based on the frequency content of the stimulus.

In fluctuating network states, an RLM with a single underlying dynamical mode performed almost as well as the best RLM we could train on that dataset (Fig. 4.5e). In contrast it took up to 10-20 dimensions to maximize the performance of the model in predicting the activities of neurons in quiescent states, and the single top dynamical mode explained only about a third of all the explained variance. This shows that sensory-driven responses in fluctuating states are largely one-dimensional, while a higher-dimensional response can be encoded by quiescent states. The absolute variance of the responses predicted from subcortical inputs was three times higher in quiescent states compared to fluctuating, and dropped off more slowly with dimension (Fig. 4.5f).

We observed that statistical models with recurrent dynamics were able to take advantage of their long timescales to better predict neural activity, which suggests that cortical dynamics are integrating and transforming inputs over hundreds of milliseconds. To test this hypothesis directly, we presented stimuli which, unlike speech, had very short autocorrelation timescales. In every 10ms interval a different randomly chosen frequency-modulated sweep was presented . Subcortical responses in the IC followed these sweeps faithfully, modulating their firing rates on the same timescales as the stimulus, but cortical responses in quiescent states were more sluggish, and instead integrated the stimuli with an autocorrelation timescale of 100ms followed by a negative autocorrelation at long delays, presumably from short-term adaptation (Fig. 4.5g,h).

4.4 Conclusion

Our analysis suggests quiescent states are ideally suited to encoding sensory stimuli in the face of two sources of ongoing noise: the external world with its vast amount of information bombarding the senses, and the internal world of the brain's own internal dynamics. Although evidence for quiescent states already exists in active animals, more in-depth characterization of neural activity in awake behaving animals is required to further our understanding of computations in the engaged brain. Across brain area comparisons would also be informative. Although quiescent states have been reported in auditory and barrel cortex, the opposite has been reported in engaged visual cortex, where firing rates increase in attentive animals. Understanding the different computational advantages of quiescent and depolarized states might thus pave a way for understanding why they are differentially preferred by brain areas corresponding to different senses.

4.5 Methods

4.5.1 Integrate-and-Fire Network

The results in figure 4.4 were generated through numerical simulation of a network of conductance-based leaky integrate and fire neurons. There are three currents in the model: an excitatory, an inhibitory and an adaptation current. The subthreshold membrane potential for a single neuron i obeys the equation

$$\tau_m \frac{\mathrm{d}V_i}{\mathrm{d}t} = -(V_i - E_L) - g_{Ei}(V_i - E_E) - g_{Ii}(V_i - E_I) + -g_{Di}(V_i - E_D).$$

When $V > V_{th}$, a spike is recorded in the neuron and the neuron's voltage is reset to $V_{reset} = 0.9V_{th}$. For simplicity, we set $V_{th} = 1$ and the leak voltage $E_L = 0$. The excitatory voltage $E_E = 2V_{th}$ and $E_I = E_D = -0.5V_{th}$. Each of the conductances has a representative differential equation which is dependent on the spiking of the neurons in the network at the previous time step, $\boldsymbol{s}_{t-1}$. The excitatory conductance obeys

$$\tau_E \frac{\mathrm{d}\boldsymbol{g}_E}{\mathrm{d}t} = -\boldsymbol{g}_E + A\boldsymbol{s}_{t-1} + b.$$

where A is the matrix of excitatory connectivity and b is the vector of tonic inputs to the neurons. The matrix of connectivity is all-to-all for the network of 128 neurons and their connectivities are randomly chosen from a uniform distribution between 0 and w_E. The tonic inputs b are uniformly distributed between 0 and b_{max}. The inhibitory conductance obeys

$$\tau_I \frac{\mathrm{d}\boldsymbol{g}_I}{\mathrm{d}t} = -\boldsymbol{g}_I + \left(c + \sum \boldsymbol{s}_{t-1}\right)^p .$$

The adaptation conductance obeys

$$\tau_E \frac{\mathrm{d}\boldsymbol{g}_D}{\mathrm{d}t} = -\boldsymbol{g}_D + w_D \boldsymbol{s}_{t-1}.$$

For all the simulations in figure 2, $\tau_m = 26$ ms, $\tau_E = 44$ ms, $\tau_I = 39$ ms, $\tau_D = 261$ ms, $w_E = 0.15$, $b_{max} = 0.025$, and $p = 1.25$. For the spontaneous fluctuations simulations (parts d, e, g, h, i, j and l), $w_D = 0.09$, $w_I = 0.047$, $c = 0$. For the quiescent simulations shown in part k and l, $w_D = 0.1$, $w_I = 0.07$, and $c = 0.02$. Part a shows example currents from a spontaneous fluctuation simulations. Parts d and e were produced from 8 minute simulations of the spontaneous fluctuations state not driven by stimulus. For parts g, h, and i, single spikes were inserted into the spontaneous fluctuations state. Part h is the membrane potential trace for the neuron in part g which has an added spike. Part i is the average firing rate of the network in 256 trials of 3 seconds each with a spike added in the middle. Parts j and k are driven by a stimulus of magnitude 0.06 distributed across 3 frequencies at a given time out of 20 possible frequencies. The tuning of the input to each cell has a standard deviation of 4 frequencies. The tones in silence are 100 ms long and separated by 1 s. The tones in silence were used to compute the tuning curves in figure 4 part a.

V

Recurrent linear analysis of state-dependent A1 population activity

Outline

In this section we further investigate the dynamical properties of neural responses in different brain states. We make a finer distinction between different types of multi-neuron patterns and reproduce them in network simulations. We use our statistical modelling framework to directly characterize dynamics in anesthetized recordings, awake-passive recordings as well as network simulations of these recordings. We introduce a reduced population model with four variables corresponding to excitation, inhibition, adaptation and facilitation and use it to show that changes in inhibitory strength can drive state-transitions in the system.

5.1 Cortical states

[1] Cortical state varied throughout the experiments and substantially affected the multi-neuron patterns recorded. Although typically distinguished into synchronized and desynchronized, we found there was a more fine distinction between different types of synchronized and desynchronized states. The state we referred to as fluctuating in the previous chapter would typically subsume most synchronized states, but the state we referred to as quiescent is only a particular subtype of the desynchronized states. In the previous chapter we referred to states as fluctuating and quiescent in order to refer directly to their phenomenology, but in this chapter and the next we situate cortical states into the existing literature and thus refer to states as different types of synchronized and desynchronized.

We recorded neural activity under a few different anesthetics and observed at least four qualitatively different patterns of multi-neuron responses. A single anesthetic typically only induced one or two different states.

The desynchronized depolarized state is characterized by an ongoing high spontaneous firing rate without fluctuations (Fig. 5.1a). Stimulus responses occur reliably on every presentation. Such states have been described in Urethane anesthetized, sleeping and passive animals and modelled by Renart et al as a classical balanced excitatory-inhibitory network ([Renart et al., 2010]). With appropriate choices of parameters, such networks can cancel out correlations in inputs, at the expense of introducing chaotic behavior and responding more to the onsets and offsets of stimuli. The more tame version of balanced network originally described by van Vreeswijk and Sompolinsky, has a slightly different computational role and faithfully tracks inputs instead of responding only at onsets and offsets ([van Vreewijk and Sompolinsky, 1996]). Later on we will show that our data favors the second version. In addition, recent results in subcortical areas suggest there are no correlations in inputs to be cancelled out by a balanced

[1] The work described in this chapter has been done in collaboration with Nicholas Lesica and Carsen Stringer. Nick expertly performed all anesthetized experiments analyzed here. Carsen helped to develop and implement the network simulations. Awake passive data was generously provided by Peter Bartho.

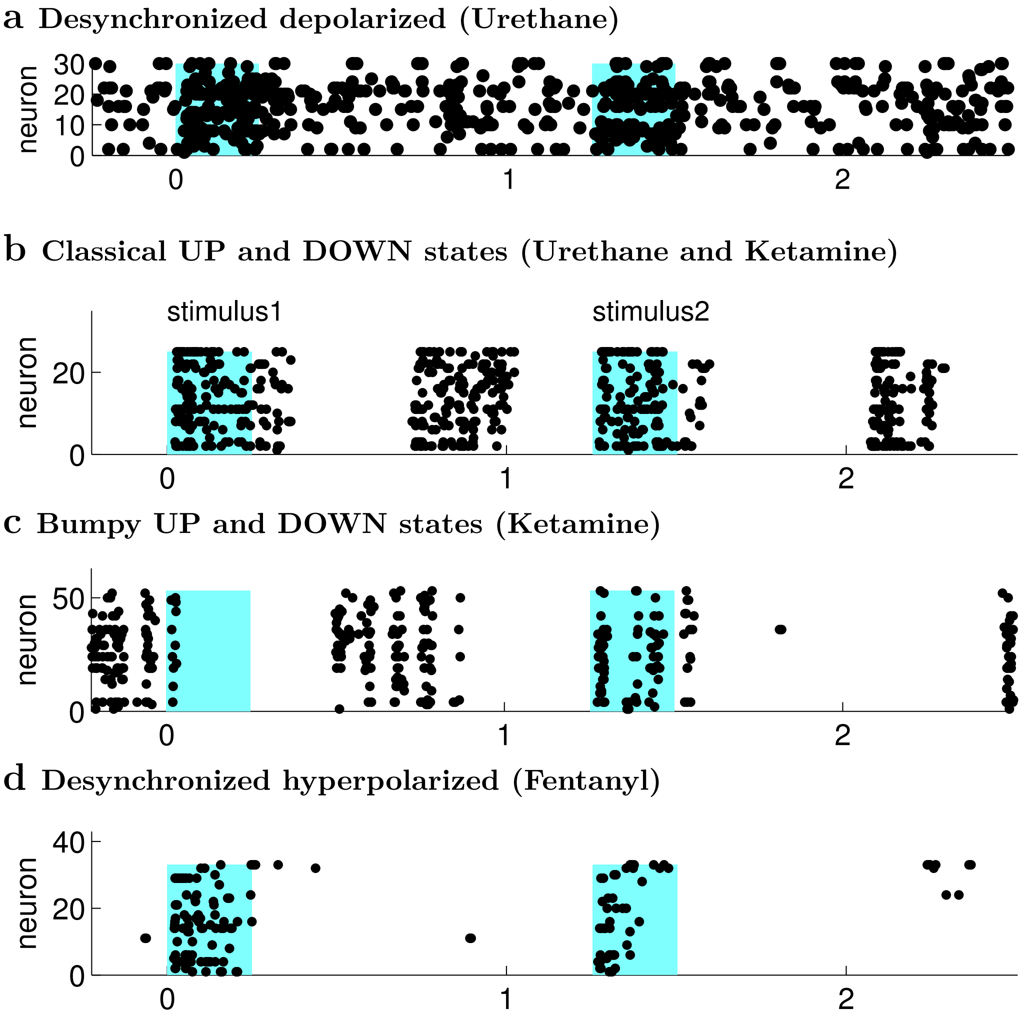

a Desynchronized depolarized (Urethane)

b Classical UP and DOWN states (Urethane and Ketamine)

c Bumpy UP and DOWN states (Ketamine)

d Desynchronized hyperpolarized (Fentanyl)

Figure 5.1: **Cortical state varies throughout experiments and substantially affects the multi-neuron patterns recorded.** **a)** The desynchronized depolarized state. **b)** The classical UP and DOWN states. **c)** Bumpy UP states. **d)** The quiescent states.

network, so the primary motivation of Renart et al has little actual relevance ([Renart et al., 2010]).

The classical UP and DOWN states have been described as ongoing transitions between hyperpolarized and depolarized states (Fig. 5.1b). These transitions occur randomly and stimuli presented on DOWN states may fail to elicit a response. They contain significant power at frequencies of 1-2Hz, owing to the slow alternations between UP and DOWN states. Such states have been described broadly in anesthetized animals, as well as in passive animals, though they are not usually distinguished from the bumpy UP states we describe next. Most classical anesthetics based on urethane, isoflurane or ketamine induce such up states.

Bumpy UP states are relatively short, synchronized periods of population spiking for durations of 30-100ms (Fig. 5.1c). We observed that they tend to come together in packets of 2 or 3, and in this particular dataset even six. They contain significant power at theta frequencies of about 10Hz, in addition to still having power at 1-2Hz, like classical UP/DOWN states. It is possible the up states described by Hromadka et al, 2013 in awake animals are bumpy, because the authors of the study describe them as short and rare ([Hromadka et al., 2013]). We only saw these types of UP states in ketamine anesthesia.

The desynchronized quiescent states are more suppressed than the other states in both spontaneous activity and stimulus responses (Fig. 5.1d). Like depolarized states they have zero pairwise noise correlations, and significantly increased activity in fast-spiking cells. We only saw such states in Fentanyl-based anesthesia, but they might have been described in previous studies of awake and active animals (see previous section). These states code stimuli very sparsely, efficiently and reliably.

5.2 Model performance

We applied the model of dynamics we described in chapter 2 to the state-dependent data to analyze the nature of the statistical patterns encountered. Most of our data was obtained with either ketamine-based or fentanyl-based anesthesia, so we will focus our analysis on these. Ketamine-based anesthesia induces fluctuations in neural activity, while fentanyl-based anesthesia induces a stable, desynchronized regime of activity.

Figure 5.2 shows the performance of the RLM at capturing the multi-neuron patterns of spikes present in the datasets. The performance of the model varies as a function of the number of underlying trajectories. A single dimension of

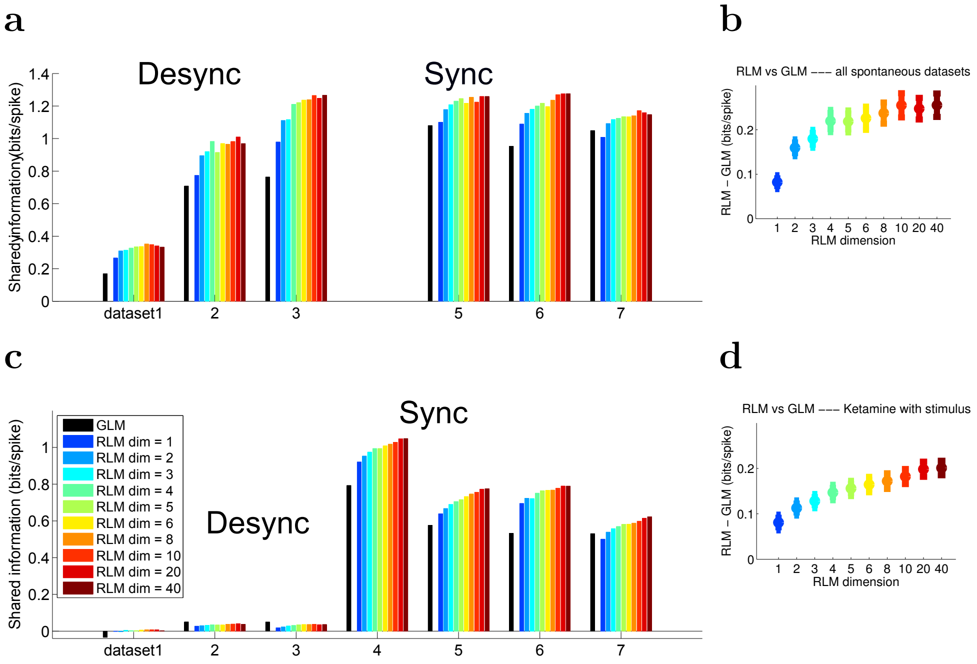

Figure 5.2: **Recurrent linear model predictive performance, compared with GLMs. a)** Model likelihoods as a function of dimensionality of underlying dynamics. Data was recorded in complete silence. **b)** Likelihood advantage of RLM models over the popular GLM framework. **cd)** Same as (a),(b) for continuous stimulus-driven activity.

dynamics already accounts for a large portion of the shared population variability, but the higher dimensions also contain information. We compared our framework with the popular generalized linear models (described in section 2), and found that the RLM offered vast improvements in prediction performance (Fig. 5.2).

5.3 The phenomenology of dynamics

In most datasets recorded, underlying dynamical trajectories were clearly organized into slow (>500ms autocorrelation) and fast trajectories (30-100ms autocorrelation). Examples are shown in figure 5.3a. The slow trajectories controlled the periodicity of the UP and DOWN states, while the fast trajectories controlled fast fluctuations within UP states. The eigenvalues of the dynamics matrix in spontaneous activity of both Fentanyl and Ketamine anesthesia were used to divide trajectories into a pair of fast and a pair of slow dynamics (Fig. 5.3b). The

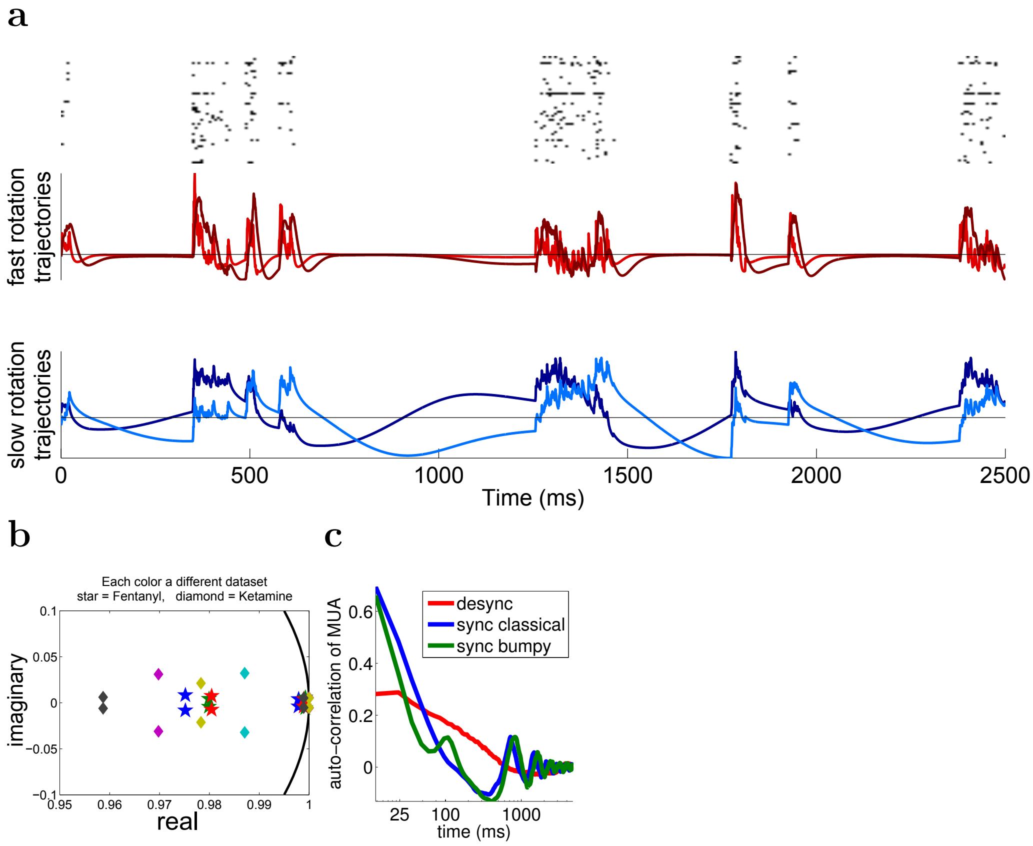

Figure 5.3: **Example trajectories in spontaneous activity. a)** Slow (>500ms autocorrelation) and fast trajectories (30-100ms autocorrelation). **b)** Eigenvalues of the dynamics matrix. **c)** Peaks in the autocorrelation function of the multi-unit activity.

pairing was obtained because each eigenvalue occurred together with its complex-conjugate eigenvalue. The slow and fast trajectories sometimes (but not always) corresponded to peaks in the autocorrelation function of the multi-unit activity (Fig. 5.3c). Even when the peak at 50-100ms lag was absent, the statistical model typically still found trajectories in that frequency range. We believe the underlying randomness of the fluctuations dissipates their power across many frequency bands thus making them hard to pick out from autocorrelation functions of power spectra. However, the RLM can still find such underlying temporal patterns because it relies on other sources of information, for example the spatial distribution over neurons of the 10Hz oscillation. We will add more details below on the underlying spatial distribution of the fast oscillation.

The time-lagged cross-correlation functions between the activity of a single cell and the summed activities of all the other cells can be organized in order of their temporal center of mass (Fig. 5.4a). Neurons with negative (positive) centers of mass tend to spike earlier (later) than the rest of the network. Such representations have been used to describe spike sequence patterns in hippocampus as well as in auditory cortex. In figure 5.4 the first row shows the spike sequence patterns for synchronized and desynchronized populations in response to a particular stimulus (a speech phone). The second row of cross-correlograms uses the sorting derived from the first row to show the spike sequence patterns in response to a second stimulus (a different speech phone). In synchronized states, the spikes sequences on different phones are largely similar, while in desynchronized states they are quite dissimilar.

The average MUA cross-correlogram latencies are similar between spontaneous and driven activity in both states (Fig. 5.4b). Importantly, the latencies computed in figure 5.4b represent the mean activities of responses to a large number of stimuli. The specific latency changes observed in figure 5.4(a) for desynchronized populations average out in figure 5.4b revealing a latency ordering much more similar to that observed in spontaneous activity.

The model-derived trajectories capture these spike sequences in the pair of fast complex-conjugate trajectories (Fig. 5.4c). We noticed that the fast trajectories were out-of-phase with each other during neural responses. Neurons represented by the first trajectory thus had an overall earlier latency on each short population UP state. In fact, there was a continuum of phases of alignment between single units and the trajectories, such that most neurons responded as a positively-weighted combination of the two (Fig. 5.4d). Figure 5.4d represents each neuron's pair of coefficients, projected onto the unit circle, and slightly perturbed off the circle for visualization purposes.

Latencies extracted from the cross-correlograms were well correlated with the phases derived from the model (5.4e). Figure 5.4f shows example cross-correlograms sorted by MUA cross-correlation latencies, while figure 5.4g shows

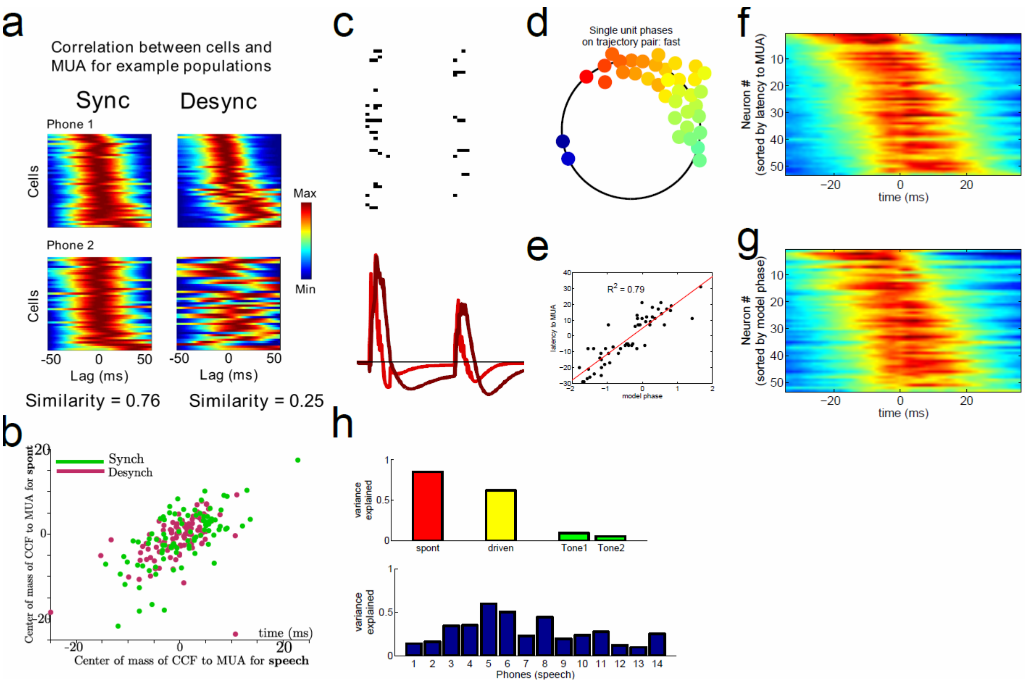

Figure 5.4: **Spike sequences.** **a)** The time-lagged cross-correlation between the activity of a single cell and the summed activities of all the other cells (more description in the main text). **b)** The average MUA cross-correlogram latencies in spontaneous and driven activity in both states. **c)** The model-derived trajectories capture spike sequences. **d)** Phases of alignment between single units and the trajectories. **e)** Latencies extracted from the cross-correlograms were well correlated with the phases computed in (d). **f)** Example cross-correlogram sorted by MUA cross-correlation latencies. **g)** The same cross-correlogram sorted by derived model phases.**h)** Explained latency variance was high for both spontaneous and average driven activity, but low for each individual phone.

the same cross-correlogram sorted by derived model phases. In desynchronized states, the R^2 value betwen latencies and model phases was high for both spontaneous and average driven activity, but low for each individual phone (figure 5.4f). This suggests that although the fast trajectories describe the average responses of the network to stimuli, each individual phone powerfully further modulates the temporal patterns of responses with additional population dimensions of variation. This is unlike the synchronized state, where each phone's cross-correlograms mostly look similar.

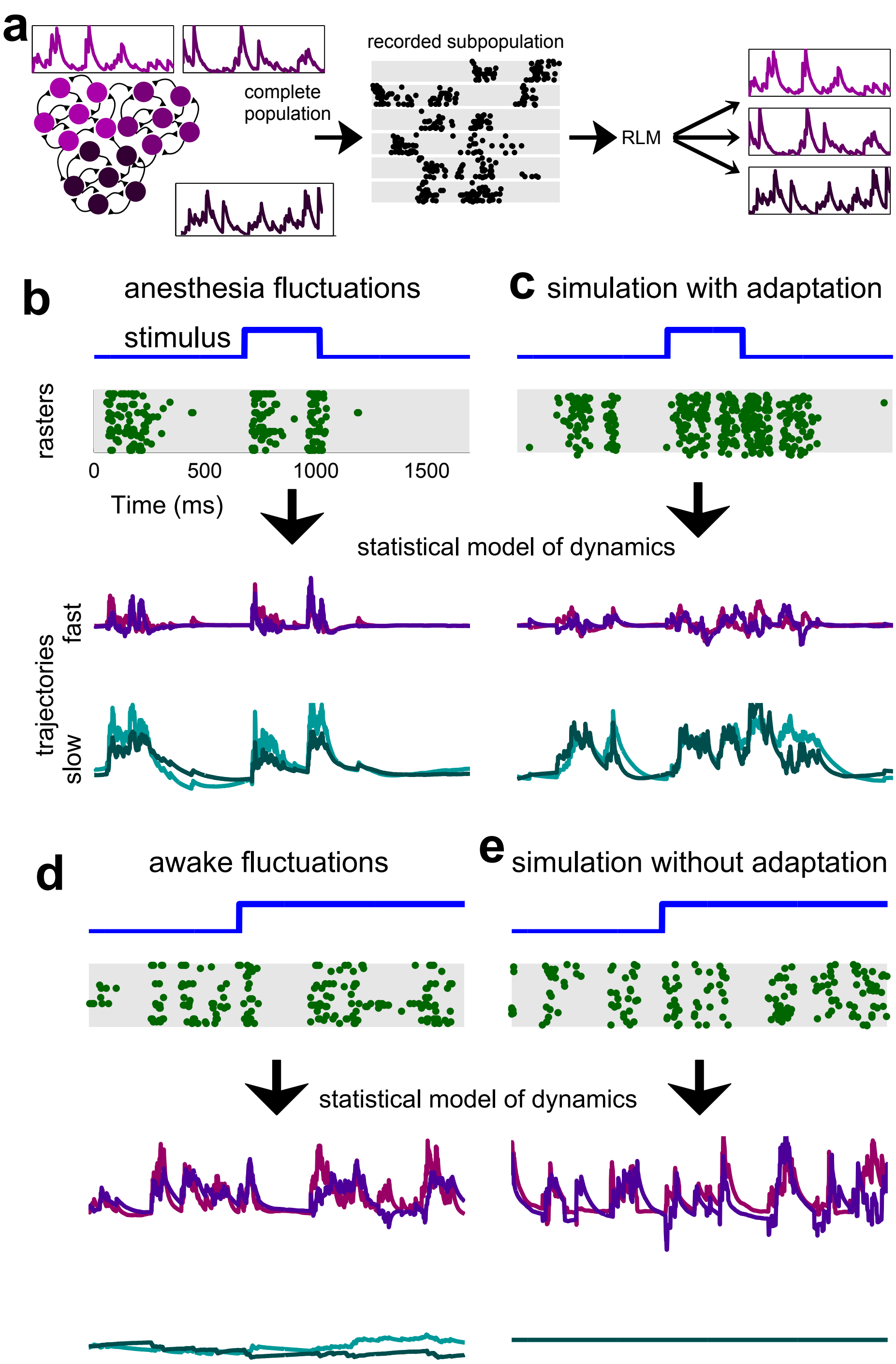

Figure 5.5: **Dynamical models capture fluctuating states and their periodicity. a)** Schematic of RLM model of population activity. **bcd)** Example of rasters and trajectories extracted from the corresponding populations.

5.4 Fluctuating states in awake-passive recordings

We used the RLM to analyze a dataset of multi-neuron recordings from the auditory cortex of awake-passive rats and compared it with the fluctuating anesthetized recordings. In addition, we used the RLM to analyze spike patterns from network simulations which we built to model the fluctuations in both anesthesia and awake states. The RLM methodology allows us to directly validate our network simulations by analyzing the underlying dynamics in both simulations and data.

Figure 5.5a shows a simplified schematic of the RLM model of population activity, while figures 5.5b-d show examples of rasters and trajectories extracted from four populations: anesthesia, simulations of anesthesia patterns, awake and simulations of awake patterns. Trajectories were divided into slow and fast on the basis of their associated eigenvalues. The main difference between the anesthetized and awake recordings was the complete absence of long timescale trajectories in the awake data. This seems to agree with the effect of wakefulness-inducing agents like acetylcholine, which are known to block long timescale adaptation processes. Similarly, it was observed that adaptation processes were absent in engaged rodents while they were learning a discrimination task, but returned once the animals became skilled and performed the task with less engagement.

However, the fast-timescale trajectories were still present in awake states and had similar temporal timecourses on the order of 30-50 ms. Although more analysis is required, we postulate that these fast timescales are generated by excitatory-inhibitory dynamics. In fact, we used this idea to generate awake-like fluctuating states, by greatly reducing adaptation in our network simulation (see previous section), while retaining a balance of excitation and inhibition. Note that the awake-passive state still shows ongoing fluctuations and responds unreliably to stimuli (not shown). Only when we also increased inhibition in the network simulation were we able to stabilize the responses and get near-zero noise correlations in stimulus responses. The state with decreased adaptation and increased inhibition thus resembled the urethane-anesthetized desynchronized state shown in figure 5.1a. Further increasing inhibition put the network simulation into a quiescent-like state, with little spontaneous activity (5.1).

To further verify our understanding of cortical states, we hypothesized that we

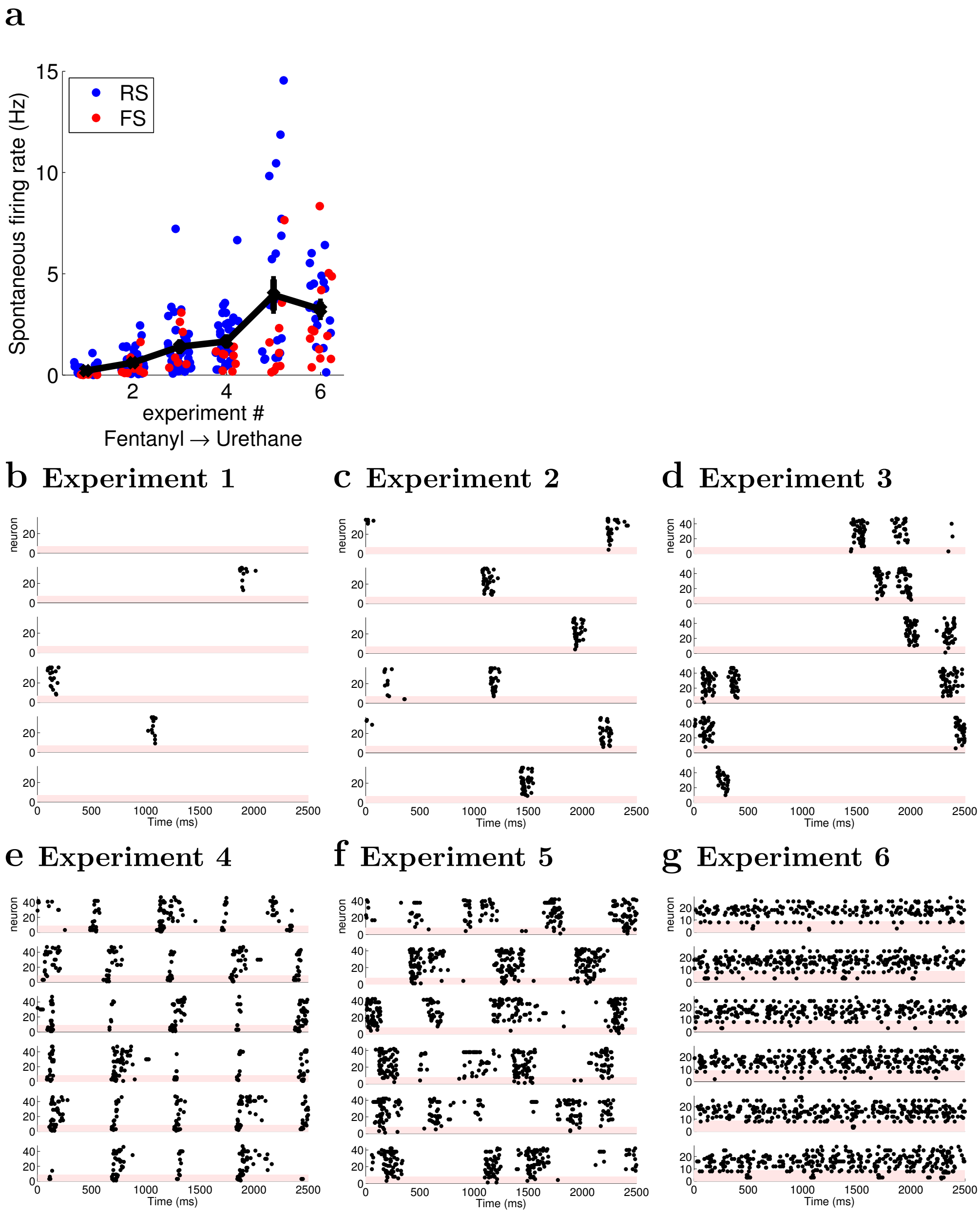

Figure 5.6: **Fentanyl to Urethane transitions. a)** Spontaneous firing rates of both FS and RS cells gradually recovered during the course of several hours. **b-g)** Multi-neuron rasters of spontaneous activity during the entire experimental session.

might observe all the brain states in the same cortical population if we gradually change the anesthetic during a long experimental session. An experiment was started with Fentanyl anesthesia (used during surgery) and continued with Urethane anesthesia. As the Urethane anesthetic started having a stronger effect and the Fentanyl anesthetic wore off, the patterns of spontaneous multi-unit activ-

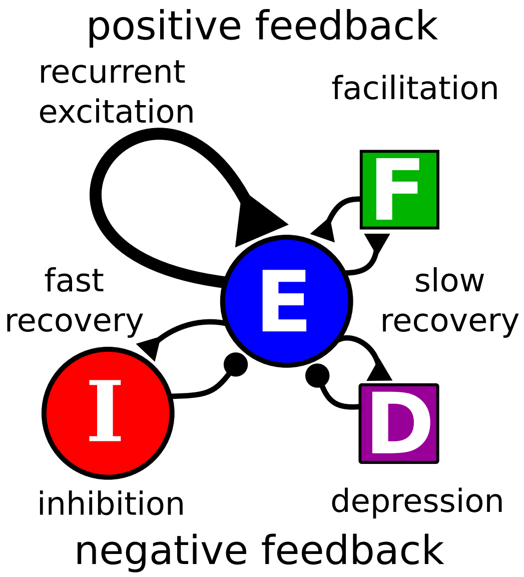

Figure 5.7: Schematic of the sources of positive and negative feedback, divided into fast and slow-acting mechanisms. While excitation and inhibition act and recover quickly, facilitation and adaptation operate on longer timescales.

ity transitioned through all the cortical states described, as shown in figure 5.6. Spontaneous firing rates of both FS and RS cells gradually recovered during the course of the experiment (Fig. 5.6a). In the beginning of the experiment firing was extremely sparse, but as neurons started to fire, they did so in synchronous short bursts. As the spontaneous activity further recovered, the bursts started coming in pairs separated by 100-200ms. For a short period of time, a state was observed in which neurons fired regularly in short bursts that followed each other with significant regularity about every 500ms. Eventually UP states became more extended in time and their onsets became random and apparently chaotic. Later on, the continuously depolarized state started replacing the fluctuating states.

5.5 Four-dimensional reduced simulation of network states

To gain an intuitive understanding of the RLM trajectories and the full network behavior, we constructed a four-dimensional reduced rate-based model of dynamics. This required both slow and fast terms in the differential equations to capture the two timescales of dynamics recognized by the RLM (Fig. 5.7). The fast dynamics arise from an excitatory and an inhibitory population of cells which are each represented by the rates of their populations. The rate of the excitatory population ν_E is controlled by the inhibitory population rate ν_I and the slow timescale variables, depression d and facilitation f, which represent intrinsic properties of the excitatory cells. The change in ν_E over time is

$$\tau_E \frac{\mathrm{d}\nu_E}{\mathrm{d}t} = -\nu_E + g(Z_E)$$

where

$$g(x) = \log(1 + x)$$

and

$$Z_E = [a_{EE}\nu_E + a_{EI}\nu_I - a_D d + a_F f + \text{tonic input}]_+.$$

The nonlinearity in g is necessary to obtain hysteresis in the nullclines of the system to produce the synchronized classical up and down states (Fig 5.9a). The inhibitory population differential equation takes the form

$$\tau_I \frac{\mathrm{d}\nu_I}{\mathrm{d}t} = -\nu_I + [a_{IE}\nu_E + a_{II}\nu_I]_+.$$

The facilitation and depression terms are dependent on only the excitatory rate:

$$\begin{aligned} \frac{\mathrm{d}d}{\mathrm{d}t} &= -d/\tau_D + \nu_E \\ \frac{\mathrm{d}f}{\mathrm{d}t} &= -f/\tau_F + \nu_E. \end{aligned}$$

The timescales are set such that $\tau_D > \tau_F \gg \tau_I, \tau_E$. For figure 5.8, the different states are produced by increasing the feedback from the inhibitory population onto the excitatory population, constant a_{EI}. In part (d), the inhibitory population also receives increased thalamic input. External noise is introduced to the excitatory population in order to produce trial-to-trial variability in the responses.

The same magnitude of noise and stimulus drive the excitatory population in each simulation.

The example nullclines in figure 5.9 explain how the system can exhibit these diverse patterns of activity. Part (a) qualitatively describes the behavior of the system in the synchronized classical state in the phase space of the excitatory rate ν_E and the inhibitory rate ν_I. When the system is in a down state (not firing), it is at the stable fixed point of the system at the origin. As the slow depression variable recovers, the excitatory nullcline moves upwards and the unstable fixed point of the system approaches the origin (#1). When it reaches the origin, the system undergoes a saddle node bifurcation and the two fixed points annihilate each other (#2), leaving only a single positive stable fixed point. The system approaches that fixed point and remains there until the depression variable builds up sufficiently to push the nullcline downwards (#3-4). Again, a saddle node bifurcation occurs with the upper stable fixed point disappearing and the system returning to the stable fixed point at the origin (#5-6).

Part (b) of figure 5.9 explains how the system can produce bumpy up states when slightly more inhibition is introduced to the system. The slope of the excitatory nullcline is reduced, and the excitatory and inhibitory nullclines only intersect at a single unstable fixed point. The system oscillates around this fixed point when the fixed point sits above zero (the trajectories are bounded in space and thus a limit cycle exists). However, when depression increases sufficiently and overcomes the facilitation variable, the excitatory nullcline is pushed downwards and the limit cycle is abolished. The system then sits at the stable fixed point at the origin until the depression variable recovers.

Figure 5.10 shows that the reduced system with external noise can reproduce the trial-to-trial variability observed in the synchronized datasets. The model reproduces both qualitative and quantitative features of the data.

Finally, figure 5.11 shows simulated rasters of networks with sufficient inhibitory feedback. Responses to step inputs are reliable on each trial despite external noise.

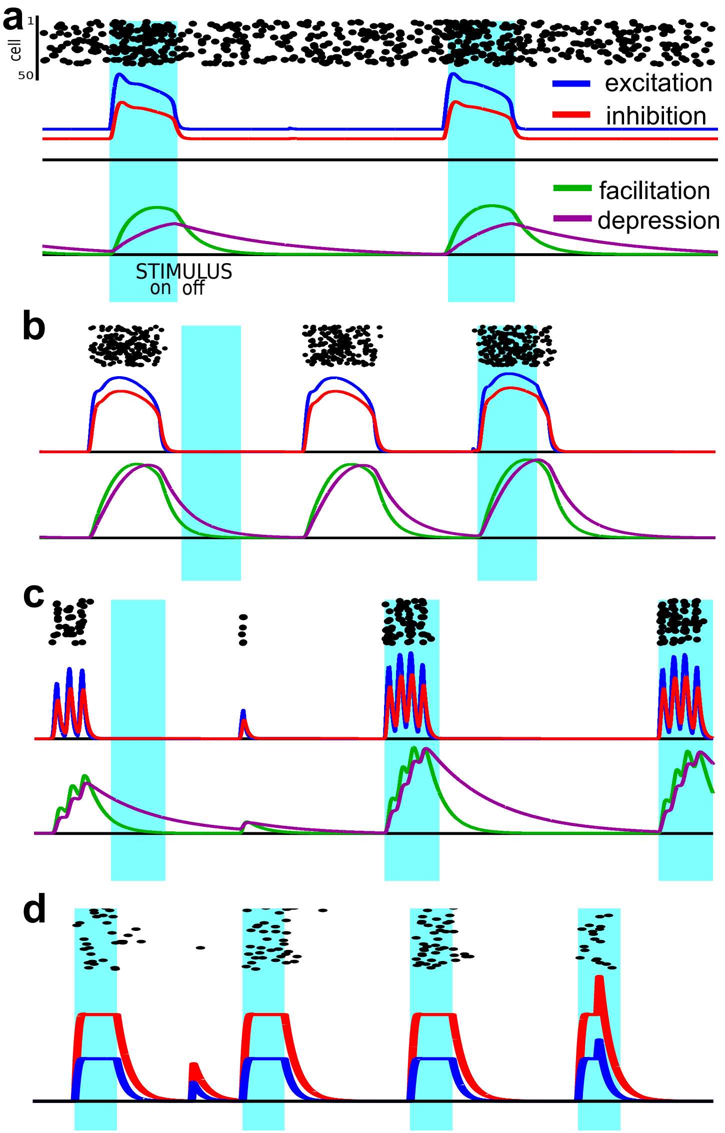

Figure 5.8: Population dynamics simulated from the model resemble the states observed in the data. Access to the simulated variables allows us to understand the phenomenology of dynamics. **a-d)** were obtained by successively increasing the inhibitory feedback to the excitatory population. **a)** Simulation of the depolarized desynchronized state. **b)** Simulation of the classical UP/DOWN state fluctuations. **c,** Simulation of the bumpy UP states. **d)** Simulation of the quiescent network state.

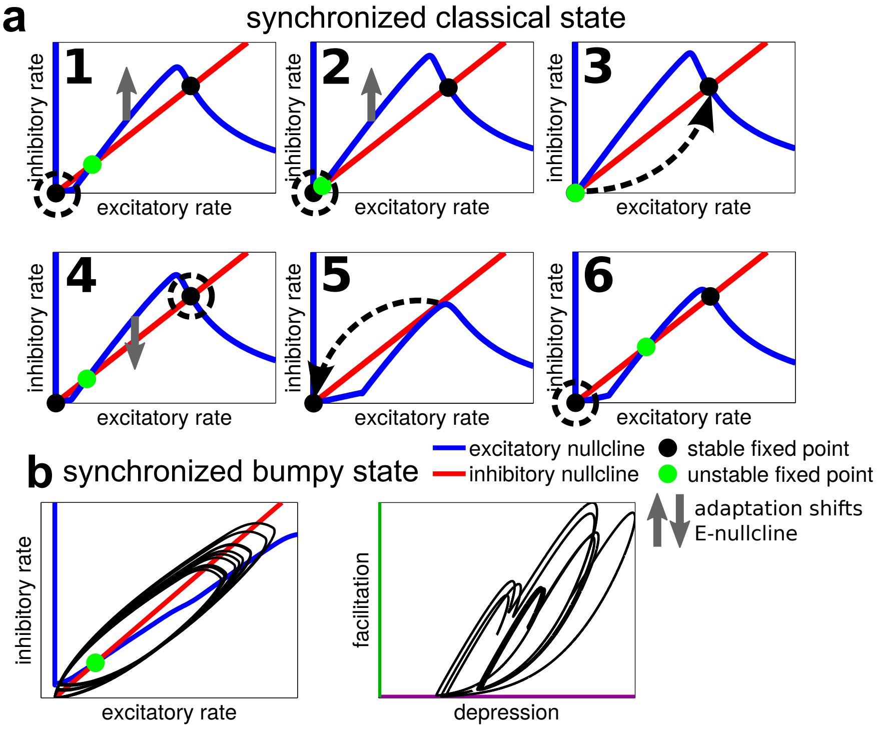

Figure 5.9: **a)** Nullcline dynamics of synchronized classical states. **b)** Nullclines of synchronized bumpy states.

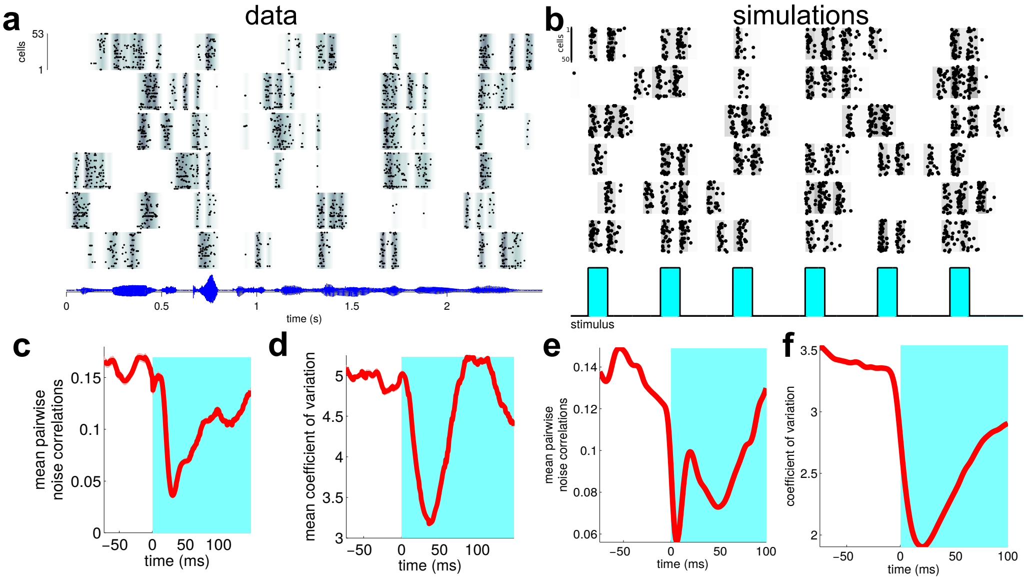

Figure 5.10: **a)** Data population rasters of neural activity driven by speech. **b)** Simulation of the data in **a** in the synchronized bumpy regime, driven by step inputs. **cd)** Pairwise noise correlations and the mean coefficient of variation are significantly reduced at stimulus onset. **ef)** Similar reductions are observed in our simulations.

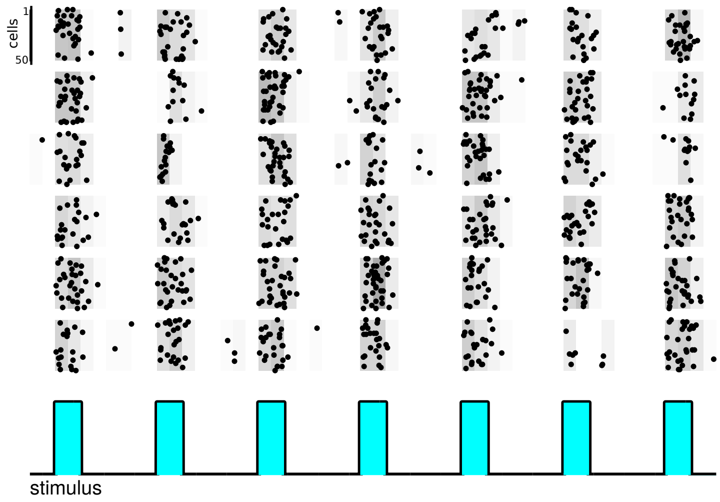

Figure 5.11: Population rasters of simulations of responses in the quiescent state. Noise correlations are abolished and trial-to-trial variability is low.

VI

State-dependent population coding in primary auditory cortex

Outline

Sensory function is mediated by interactions between external stimuli and intrinsic cortical dynamics that are evident in the modulation of evoked responses by cortical state. A number of recent studies across different modalities have demonstrated that the patterns of activity in neuronal populations can vary strongly between synchronized and desynchronized cortical states, i.e. in the presence or absence of intrinsically generated up and down states. Here we investigated the impact of cortical state on the population coding of speech in the primary auditory cortex (A1) of gerbils, and found that responses were qualitatively different in synchronized and desynchronized cortical states. Activity in synchronized A1 was only weakly modulated by sensory input, and the spike patterns evoked by speech were unreliable and constrained to a small range of patterns. In contrast, responses to speech in desynchronized A1 were temporally precise and reliable across trials, and different speech tokens evoked diverse spike patterns with extremely weak noise correlations, allowing responses to be decoded with nearly perfect accuracy. Restricting the analysis of synchronized A1 to activity within up states yielded similar results, suggesting that up states are not equivalent to brief periods of desynchronization. These findings demonstrate that the representational capacity of A1 depends strongly on cortical state, and suggest that cortical state should be considered as an explicit variable in all studies of sensory processing.

6.1 Introduction

[1] The representation of sensory inputs in the activity of primary cortical areas provides the basis for higher level processing. Characterizing this primary representation is critical for understanding sensory function, as its nature determines the suitability of different strategies for subsequent computations, and its fidelity constrains behavioral performance. The study of sensory representations is complicated by the fact that neuronal activity is determined not only by external inputs, but also by other sources that are internal to the brain. In cortex, the processing of incoming stimuli can depend strongly on brain state ([Steriade et al., 2001]; [Castro-Alamancos, 2004b]; [Haider and McCormick, 2009]; [Harris and Thiele, 2011]). In asleep, anesthetized, and awake animals, the state of the cortex can vary along a continuum of synchronized and desynchronized states with different population dynamics. When the cortex is in a synchronized state (also known as an inactivated state), activity is characterized by slow fluctuations between intrinsically generated up and down states, corresponding to periods of concerted spiking and silence across large areas, and these up and down states play a major role in shaping activity patterns ([Marguet and Harris, 2011]; [Okun et al., 2012]). Synchronized states are commonly observed during slow-wave sleep and under certain anesthetics, but recent studies have shown that the cortex can also be in a synchronized state when animals are awake ([Crochet and Petersen, 2006]; [Greenberg et al., 2008];[Poulet and Petersen, 2008]; [Xu et al., 2012];[Luczak et al., 2013]; [Polack et al., 2013]; [Sachidhanandam et al., 2013]; [Tan et al., 2014];[Zhou et al., 2014a]).

During active sensory processing in awake animals, the cortex often transitions to a desynchronized (or activated) state in which up and down states are suppressed and activity is strongly modulated by sensory inputs. Studies in the visual and somatosensory systems have observed dra-

[1] The work described in this chapter has been done in collaboration with Nicholas Lesica. Nick performed all experiments analyzed here. The analysis was developed jointly with Nick and Nick wrote the text.

matic differences between responses in synchronized and desynchronized states ([Castro-Alamancos, 2004a]; [Hasenstaub et al., 2007]; [Goard and Dan, 2009]; [Hirata and Castro-Alamancos, 2011]), and there are indications that such differences may also be present in A1 ([Ter-Mikaelian et al., 2007]; [Otazu et al., 2009]; [Marguet and Harris, 2011];[Guo et al., 2012];[Zhou et al., 2014a]). In this study, we measured the activity of populations of single units in gerbil A1 in synchronized and desynchronized states under different anesthetics and observed strong effects that were evident at both the single cell and population level. We found that cortical state modulated the selectivity, reliability, and diversity of spike patterns, as well as the strength of noise correlations, in a manner that greatly impacted the fidelity of the population code.

6.2 Synchronized and desynchronized states in A1

To study the impact of cortical state on the population coding of speech, we compared activity recorded with a multi-tetrode array in gerbil A1 (Fig.6.1a) under several different anesthetics. The cortical states imposed by anesthesia may, of course, differ from those that occur naturally. However, comparisons of spontaneous and evoked activity in rodent A1 have revealed similar dynamical properties in the synchronized and desynchronized states observed under anesthesia and those in awake animals ([Bermudez Contreras et al., 2013]; [Luczak et al., 2013]). Furthermore, the use of anesthesia enabled us to control synchronization and desynchronization without additional influences related to the particular task in which an animal is engaged, thus allowing us to perform a general comparison of A1 responses in the presence or absence of intrinsically generated up and down states.

To achieve a stable and consistent synchronized or desynchronized state throughout an entire experiment, we recorded activity under either ketamine/xylazine (KX) or fentanyl/medetomidine/midazolam (FMM). The up and down states that are typical of a synchronized cortical state were always evident in the populations recorded under KX, but were largely absent in those recorded under

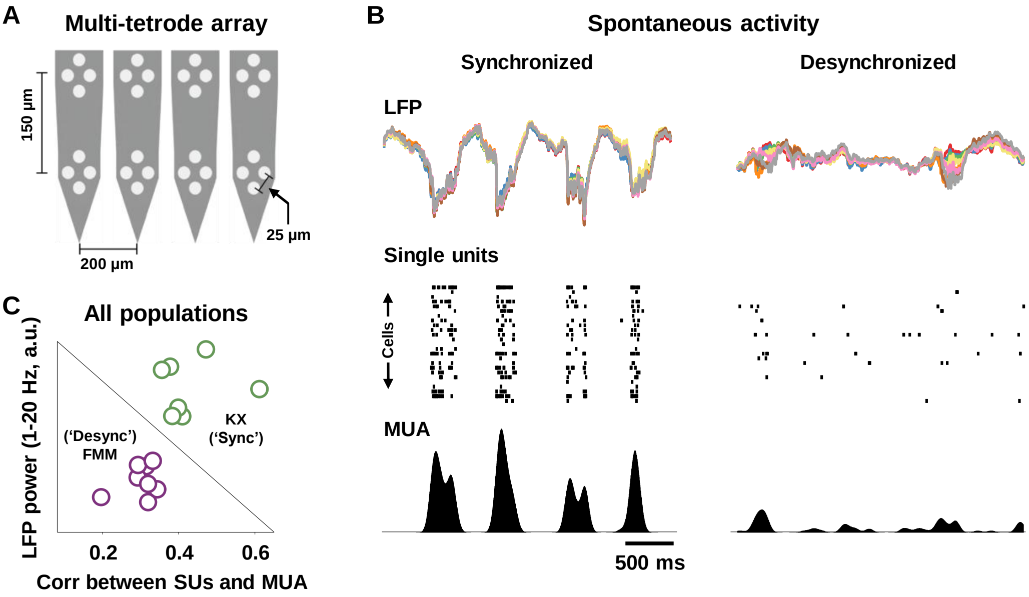

Figure 6.1: **Synchronized and desynchronized states in A1 a)** A schematic diagram of the multi-tetrode array used to record A1 activity. **b)** Examples of a short segment of activity recorded in synchronized (under ketamine/xylazine) and desynchronized (under fentanyl/medetomidine/midazolam) A1. The top row shows the local field potential (LFP; 0.1-100 Hz) recorded on each of the 8 tetrodes with the signal for each tetrode shown in a different color. Each tetrode signal is the sum across its four electrodes. The middle row shows a raster plot of the spiking of all of the single units in the population. Each row shows the spike times for one cell. The bottom row shows the multi-unit activity (MUA; the sum of the activity of all isolated single units after smoothing with a Gaussian window with a width of 50 ms). **c)** A scatter plot showing the low frequency LFP power (1-20 Hz) and average correlation between the MUA and spiking of each single unit for all of the synchronized (green) and desynchronized (blue) populations that were analyzed.

FMM. Short segments of the spontaneous local field potential (LFP), single-unit spiking, and multi-unit activity (MUA) for two example populations are shown in Fig. 6.1b. To determine the cortical state for each population, we assessed the strength of up and down states by measuring the low frequency power in the LFP and the degree to which the spiking of individual cells was similar to the MUA, as shown in Fig. 6.1c. The majority of our analysis (all figures but the last) is based on the sound-evoked responses of 7 populations recorded under KX (245 cells in total) and 8 populations recorded under FMM (284 cells in total) that exhibited stable synchronized and desynchronized states, respectively. To confirm that the state-dependent effects that we observed when comparing different populations were also evident when comparing synchronized and desynchronized states within the same population, we also recorded from 3 populations (131 cells in total) under urethane in which A1 exhibited spontaneous fluctuations between synchronized and desynchronized states ([Curto et al., 2009]; [Marguet and Harris, 2011]; [Okun et al., 2012]; [Bermudez Contreras et al., 2013]). Our analysis of these populations is summarized in the final figure.

6.3 The impact of cortical state on responses to tones

We began by examining A1 responses to tones. While, on average, the spike rates evoked by tones were higher than spontaneous rates in both states (median increase: 0.68 spikes/s for synchronized, n =251, 1.24 spikes/s for desynchronized, n = 224), the relative increase was much higher in the desynchronized state, as illustrated in the frequency responses areas (FRAs) for two example populations shown in Fig. 6.2a. For tones presented at 56 dB SPL, we measured the fraction of cells in each population that responded significantly above their spontaneous rate to the best frequency for that population (i.e. the frequency that evoked a significant response from the largest fraction of cells), as well as the fraction of cells that responded significantly to at least one of the frequencies tested. As shown in Fig. 6.2b, only a small fraction of cells in synchronized A1 responded significantly above their spontaneous rate (median values: 13% for best tone, 18% for any tone, n = 6 populations), consistent with previous studies, but in desynchronized A1, nearly all cells responded significantly in some populations (median values: 83% for best tone, 93% for any tone, n = 8 populations). These differences in population medians between synchronized and desynchronized A1, as well as all of the other differences in population medians between synchronized and desynchronized A1 reported in figures 1 through 5, were significant with $p < 0.001$ (Wilcoxon rank-sum test).

It is possible that increased responsiveness in desynchronized A1 could be accompanied by a loss of selectivity, but this was not the case. As shown in Fig.

6.2c, frequency tuning (width of spike rate tuning at half max for tones at 56 dB SPL) was much sharper in desynchronized A1 (median value: 1 octave, n = 224 cells) than in synchronized A1 (median value: 2.4 octaves, n = 251 cells). For some populations, we also examined the selectivity to the speed and direction of frequency modulations (FMs). The responses of example cells from synchronized and desynchronized A1 to FM tones are shown in Fig. 6.2d. We quantified selectivity for speed (or direction) based on the maximum and minimum spike rates observed across all speeds (or directions) as (max rate - min rate) / (max rate

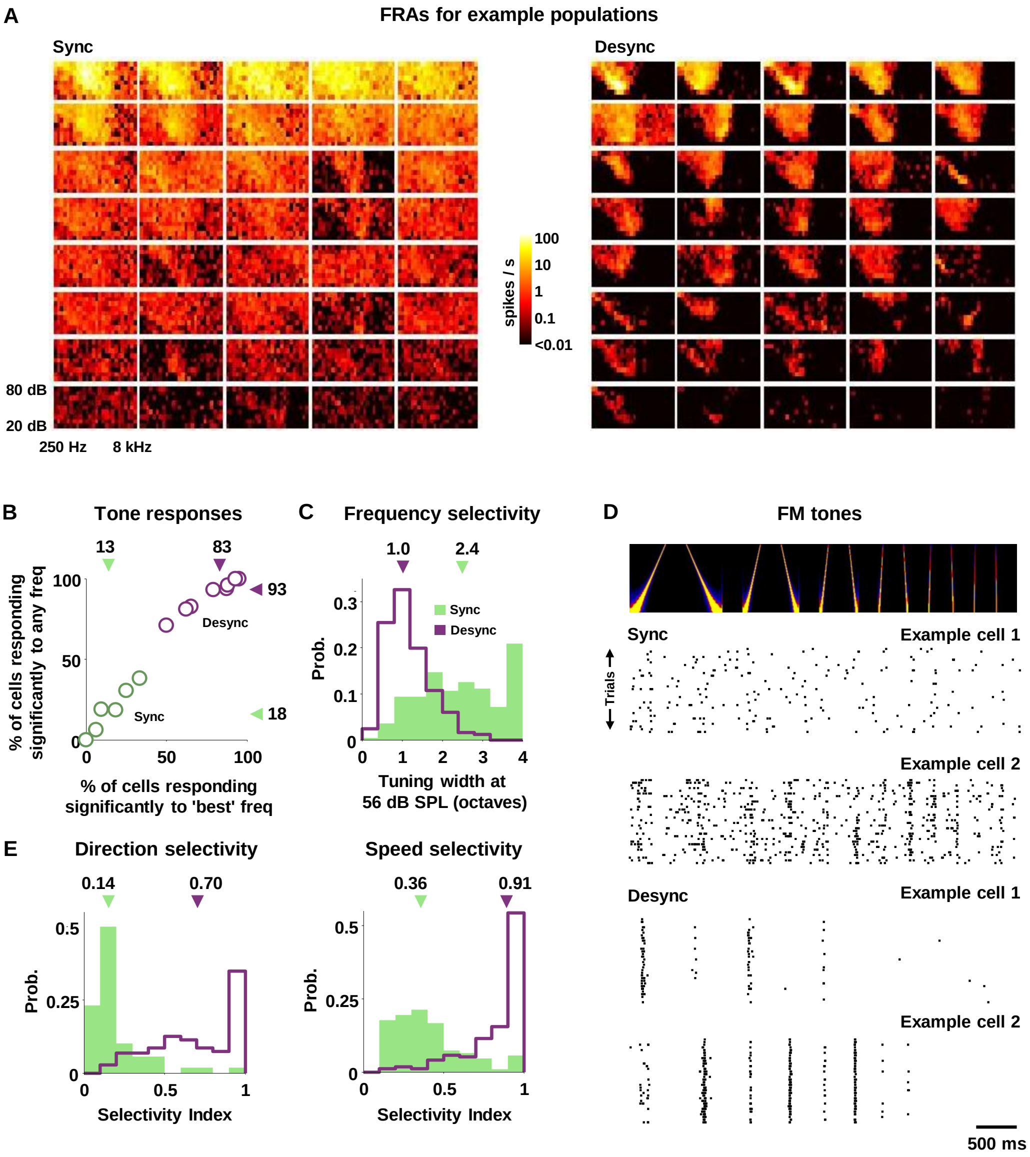

Figure 6.2: (Caption next page.)

Figure 6.2: (Previous Page). **The impact of cortical state on responses to tones. a)** Frequency response areas (FRAs) for example populations in synchronized and desynchronized A1. Each image shows the average spike rate of responses to tones of different frequencies and intensities for one cell. Cells were ordered according to how strongly their activity was modulated by the tones as measured by the variance in their average spike rates across all frequencies and intensities. The two cells that were most weakly modulated in the synchronized population and the one cell that was most weakly modulated in the desynchronized population are not shown. **b)** A scatter plot showing the percentage of cells in each synchronized (green) and desynchronized (blue) population that responded to the best frequency for that population (i.e. the frequency that evoked a significant response from the largest fraction of cells) and the fraction of cells that responded significantly to at least one of the frequencies tested. A response was considered significant if the average spike rate was more than 2 standard deviations above the average spontaneous rate. The median values are indicated by the arrows. **c)** The distribution of the frequency tuning widths for cells in synchronized (green) and desynchronized (blue) A1. Tuning width was measured as the range of frequencies for which the average spike rate was at least half of its maximum value for tones at 56 dB SPL. The median values are indicated by the arrows. **d)**Responses of example cells from synchronized and desynchronized A1 to repeated presentations of frequency-modulated (FM) tones. The top row shows the spectrogram of the sounds, the bottom rows show raster plots for individual cells. Each row in the raster plots shows the spike times for one trial. **e)** Distributions of the speed selectivity index and direction selectivity index for responses of individual cells in synchronized and desynchronized A1 to FM tones, plotted as in C.

+ min rate). Cells in synchronized A1 were generally either non-responsive or weakly selective (median selectivity index: 0.14 for direction, 0.36 for speed, n = 108 cells), while cells in desynchronized A1 were highly selective for both speed and direction (median selectivity index: 0.7 for direction, 0.91 for speed, n = 175 cells), as shown in Fig. 6.2e.

6.4 The impact of cortical state on the temporal precision and reliability of responses to speech

The fidelity of the A1 representation depends on the degree to which responses to any given sound are reliable across repeated trials. We found that responses in synchronized A1 were highly variable, while responses in desynchronized A1

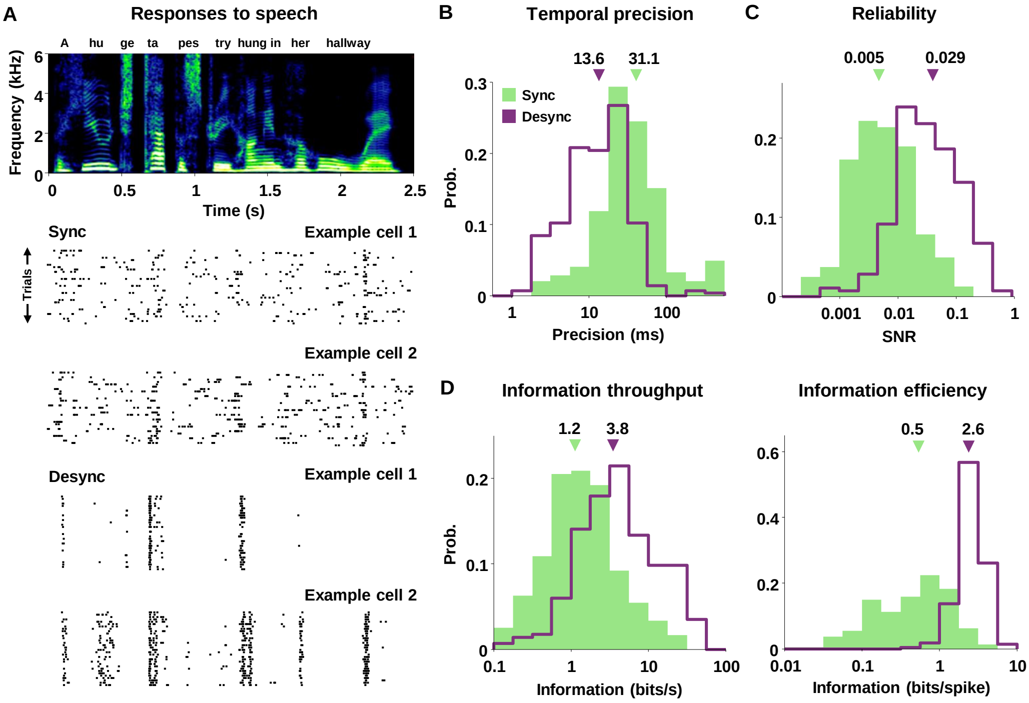

Figure 6.3: **The impact of cortical state on the temporal precision and reliability of responses to speech. a)** Responses of example cells from synchronized and desynchronized A1 to repeated presentations of speech. The top row shows the spectrogram of the sound, the bottom rows show raster plots for individual cells. Each row in the raster plots shows the spike times for one trial. **b-d)**Distributions of the temporal precision, reliability, information throughput, and information efficiency of responses of individual cells in synchronized and desynchronized A1 to speech, plotted as in figure 2.

contained temporally precise firing events that were reliable across trials. The responses of two example cells from synchronized and desynchronized A1 to a short segment of speech are shown in Fig. 6.3a. To quantify the temporal precision of the responses, we measured the timescale at which spike timing needs to be considered to capture the information in single spikes (i.e. the information in the PSTH) from each cell. We defined the precision for each cell by jittering the spike times with successively larger amounts of noise until the information in the responses decreased to 95% of its original value ([Garcia-Lazaro et al., 2013]). As shown in Fig. 6.3b, the median precision was 31 ms in synchronized A1 (n = 245 cells) and 13 ms in desynchronized A1 (n = 284 cells).

To quantify the reliability of the responses across trials, we measured the signal to noise ratio (SNR) defined as the ratio of unbiased estimates of the signal (repeatable) and noise (not repeatable) response power ([Sahani and Linden, 2003]), with responses represented as binary vectors with 2 ms bins. As shown in Fig. 6.3c, cells in desynchronized A1 were, on average, six times more reliable than those in synchronized A1 (median values: 0.005 for synchronized, 0.029 for desynchronized), with the SNR of the most reliable cells in desynchronized A1 approaching values typically observed in sub-cortical areas ([Horvath and Lesica, 2011]). Finally, to quantify the overall fidelity of A1 responses in a manner that combines precision and reliability, we measured the throughput and the efficiency of the single spike information for each cell. The information throughput (bits/s) in desynchronized A1 cells was three times higher than that in synchronized A1 cells (median values: 1.2 bits/s for synchronized, 3.8 bits/s for desynchronized) and the information efficiency (bits/spike) in desynchronized A1 cells was 5 times higher than that in synchronized A1 cells (median values: 0.5 bits/spike for synchronized, 2.6 bits/spike for desynchronized), as shown in Fig. 6.3d.

6.5 The impact of cortical state on the similarity of spike patterns evoked by different speech tokens

The above results demonstrate that individual cells in desynchronized A1 respond reliably to repeated presentations of the same sound. However, the representation in A1 depends not only on the fidelity of individual cells, but also on the extent to which different sounds evoke different spike patterns across the population. Previous studies in rodent A1 have shown that responses can be highly constrained, with different sounds evoking spike patterns that are remarkably similar ([Luczak et al., 2009];[Bathellier et al., 2012]). We examined the similarity of responses evoked by different segments of speech and found that, while there was a high degree of similarity between responses in synchronized A1, responses in desynchronized A1 were much more diverse.

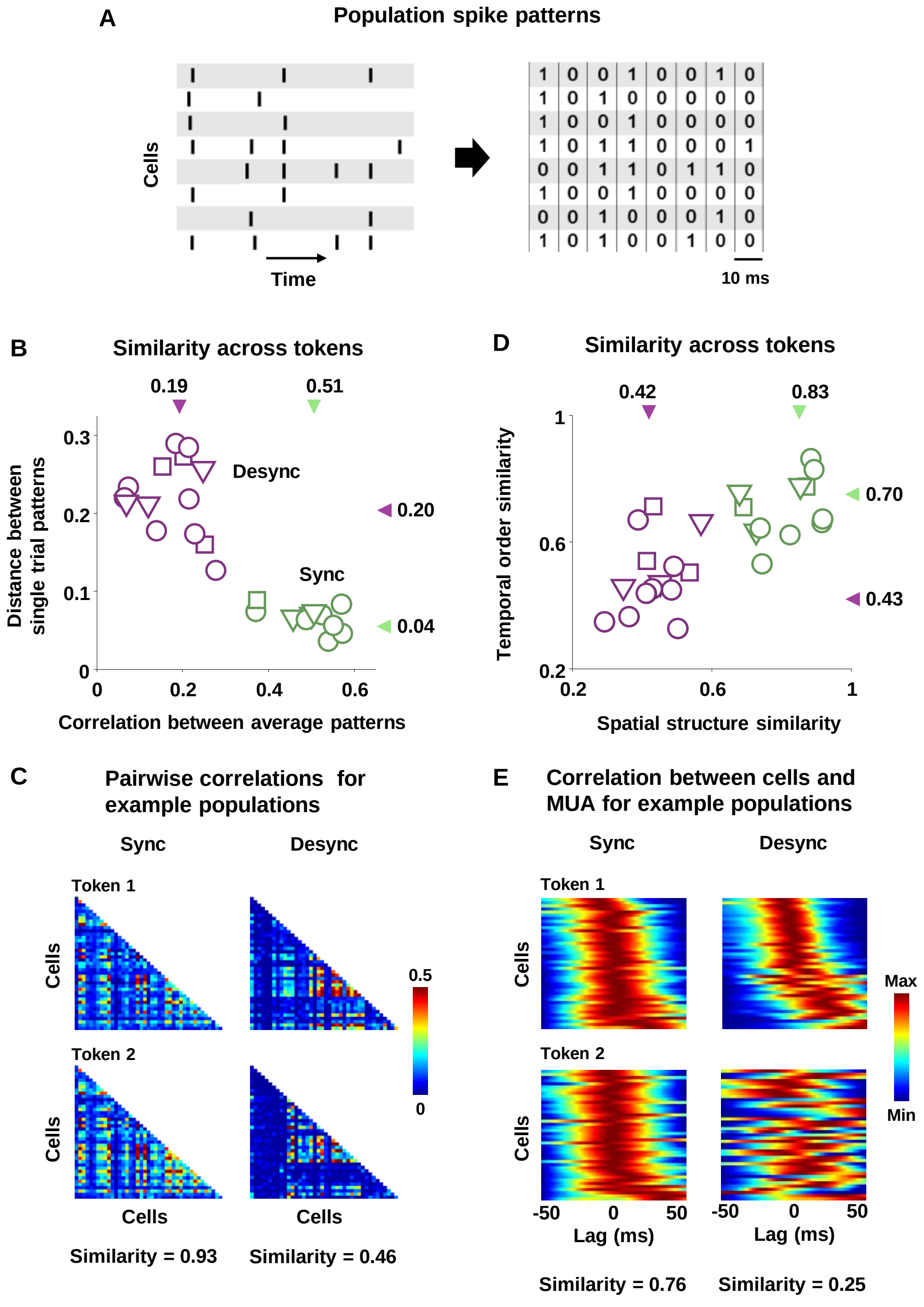

Figure 6.4: (Caption next page.)

We represented population spike patterns as binary matrices (see Fig. 6.4a) and measured the average similarity between both the single-trial and trial-averaged patterns evoked by different speech tokens. The spike patterns in synchronized

Figure 6.4: (Previous page.) **The impact of cortical state on the similarity of spike patterns evoked by different speech tokens. a)** The responses of each population to each trial of each token were represented as binary matrices with rows corresponding to cells and columns corresponding to 10 ms time bins. **b)** A scatter plot showing the similarity of the spike patterns across speech tokens for each synchronized (green) and desynchronized (blue) population for both single trial responses and responses averaged across trials. For trial average similarity, values are the average correlation between the average spike patterns evoked by each pair of tokens. For single trial similarity, values are the average fractional increase in the distance between spike patterns evoked by each pair of tokens relative to the average distance between patterns evoked by the same token. For those populations for which responses were recorded for more than one set of tokens, multiple symbols are shown (circles for token set 1, squares for token set 2, and triangles for token set 3). The median values (with each token set for each population treated as a separate measurement) are indicated by the arrows. **c)** The pairwise correlations for the responses of example synchronized and desynchronized A1 populations to different speech tokens. Each square in each image shows the correlation for one pair of cells. The images in the top row show the correlations for the first token and the images in the bottom row show the correlations for the second token. The similarity of the correlations for token 1 and token 2 are shown. Similarity was measured as the correlation between the set of pairwise correlations for each token. **d)** A scatter plot showing the similarity of the spatial pattern and temporal order of spiking across speech tokens for each synchronized (green) and desynchronized (blue) population, plotted as in B. **e)** The correlation function between the spiking of individual cells and the multi-unit activity for the responses of example synchronized and desynchronized A1 populations to different speech tokens. Each row in each image shows the correlation function for one cell. For plotting, the correlation functions for all cells were scaled to have the same maximum and minimum values, and the cells were ordered according to their latency with respect to the MUA for the first token. The latency was measured as the center of mass of the correlation function. The ordering of the images was the same for the first and second tokens. The similarity of the latencies for token 1 and token 2 is shown. Similarity was measured as the correlation between the set of latencies for each token.

A1 were much more similar across tokens than those in desynchronized A1, both for the average patterns evoked by each token across trials and for the patterns evoked on single trials. As shown in Fig. 6.4b, the median correlation between average patterns for each pair of tokens was 0.51 for synchronized A1 (7 populations each with between 1 and 3 sets of 7 different tokens for total n = 12) and 0.19 for desynchronized A1 (8 populations for total n = 14). This result indicates a qualitative difference between synchronized and desynchronized A1:

if the intrinsic dynamics in synchronized A1 simply added ’noise’ to the responses observed in desynchronized A1, the similarity between the trial-averaged patterns in the two states would be the same. The difference between synchronized and desynchronized A1 was also evident when comparing the spike patterns evoked on single trials. As shown in Fig 6.4b, the median fractional increase in the average distance between single trial patterns for each pair of tokens relative to the average distance between patterns for the same token was 4% for synchronized A1 and 20% for desynchronized A1 (note that while the distances may seem small even for desynchronized A1, they are sufficient to support nearly perfect classification in the high dimensional response space, as shown below).

To examine the similarity of spike patterns in more detail, we followed the approaches of previous studies for comparing patterns based on their spatial and temporal structure ([Luczak et al., 2009]; [Luczak et al., 2013]). We represented the spatial structure of spiking for each token by the set of correlations between the spike patterns of each pair of cells in the population (i.e. the correlations between the rows of the binary spike pattern matrices). Fig 6.4c shows the set of pairwise correlations for two example populations for two different speech tokens (each square in each image shows the correlation between one pair of cells for a given token). In synchronized A1, the spatial structure of spiking was largely preserved across tokens, while in desynchronized A1, the spatial structure varied from token to token. To quantify the degree to which the spatial structure of spiking for each population was similar across tokens, we measured the correlation between the spatial structures for each pair of tokens and averaged across all pairs of tokens. As shown in Fig. 6.4d, the spatial structure of spiking in synchronized A1 was twice as similar across tokens as that in desynchronized A1 (median values: 0.83 for synchronized, 0.42 for desynchronized).

We also examined the degree to which the temporal order of spiking for each population was similar across tokens. We represented the temporal order of spiking for each token by the set of latencies measured from the center of mass of the correlation function between the spiking of each cell in the population and the MUA (i.e. the correlation function between each row of the binary spike pattern matrices and the sum of all rows). Fig. 6.4e shows the set of correlation functions for two example populations for two different speech tokens (each row in each image shows the correlation function between one cell and the MUA). In synchronized A1, the temporal order of spiking was largely preserved across tokens, while in desynchronized A1, the temporal order varied from token to token (for the images in Fig. 6.4e, the cells in each population were ordered according to their latency for the first token and plotted in the same order for the second token). To quantify the degree to which the temporal order of spiking for each population was similar across tokens, we measured the correlation between the latencies for each pair of tokens and averaged across all pairs of tokens. As shown in Fig. 6.4d, the temporal order of spiking was much more similar across tokens in synchronized A1 than in desynchronized A1 (median values: 0.7 for synchronized, 0.43 for desynchronized).

6.6 The impact of cortical state on noise correlations and population decoding

The above results demonstrate that the degree of similarity in the spike patterns evoked by different sounds differs strongly between synchronized and desynchronized A1. However, the extent to which A1 can support discrimination of different sounds depends not only on the range of evoked patterns, but also on the strength of the correlations in the trial-to-trial variability in these patterns across the population. Fig. 6.5a shows the distributions of pairwise noise correlations in responses to speech for each population (i.e. the difference in the correlations between the rows of the binary spike pattern matrices before and after shuffling the trial order). While noise correlations in synchronized A1 were relatively strong (median value: 0.07, n = 6451 pairs), those in desynchronized A1 were extremely weak (median value: 0.002, n = 6101 pairs). These results were consistent across a wide range of time scales (see Fig. 6.5b). To quantify how the differences between spike patterns in synchronized and desynchronized A1 impact the representation of speech, we trained a support vector machine to

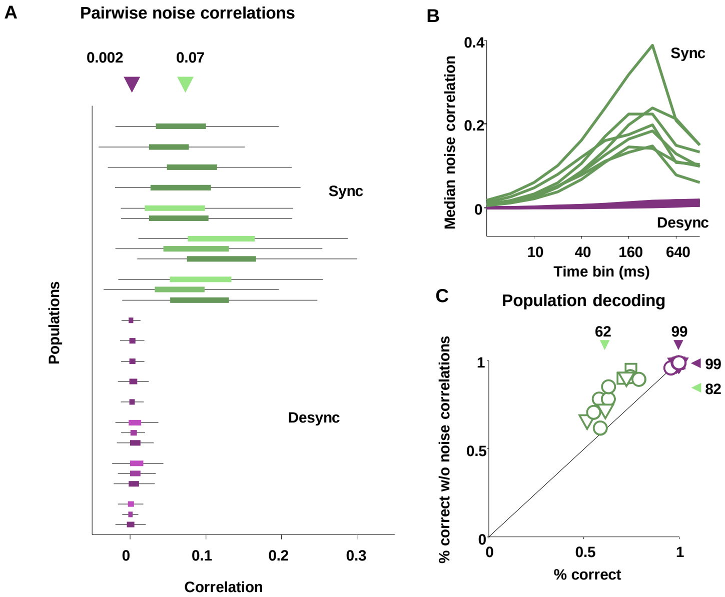

Figure 6.5: **The impact of cortical state on noise correlations and population decoding a)** Box and whisker plots showing the distribution of pairwise noise correlations for each synchronized (green) and desynchronized (blue) population. The box spans the 25th to 75th percentiles, and the whiskers span the 5th to 95th percentiles. For those populations for which responses were recorded for more than one segment of speech, multiple distributions are shown (darkest color for token set 1, middle color for token set 2, and lightest color for token set 3). The median values for all pairs across all populations are indicated by the arrows. **b)** The median pairwise noise correlations in responses to speech for each synchronized (green) and desynchronized (blue) population. The response of each cell to each trial was represented as a binary vector with a range of time bins as indicated on the horizontal axis. **c)** A scatter plot showing the performance of a support vector machine in decoding the responses of each synchronized (green) and desynchronized (blue) population to different speech tokens with and without noise correlations, plotted as in figure 4B.

predict which speech token evoked a given single trial response. As shown in Fig. 6.5c, decoding of population spike patterns from desynchronized A1 was highly accurate (median performance: 99% correct), while decoding of patterns from synchronized A1 was substantially worse (median performance: 62% correct). Decoding of synchronized A1 responses was also impacted by noise correlations; when noise correlations were removed by shuffling the trial order before training the classifier and decoding, median performance increased from 62% correct to 82% correct ($p < 0.001$, Wilcoxon signed-rank test).

6.7 Spike patterns evoked by different speech tokens in synchronized A1 are similar and have strong noise correlations even within up states

It has been hypothesized that up states in synchronized cortex may be equivalent to brief periods of desynchronization ([Destexhe et al., 2007]; [Castro-Alamancos, 2009]). This implies that the differences in the spike patterns in synchronized and desynchronized A1 that we have observed can be accounted for by the global dynamics of up and down states in synchronized A1, and that if only the activity within up states is considered, the differences between synchronized and desynchronized A1 should be small. We found, however, that restricting the analysis of synchronized A1 to activity within up states had little impact on our results.

Fig. 6.6a shows the probability of being in an up state for an example population from synchronized A1 during repeated presentations of a short segment of speech. The timing of up and down states in this population was strongly modulated by the sound, and this effect was consistent across all of the populations that we studied in synchronized A1; the reliability of the timing of up and down states across trials measured as the SNR for binary vectors specifying whether the population was in an up or down state in 10 ms time bins was 0.17?0.09 (7 populations each with between 1 and 3 different speech segments for total n = 12). Fig. 6.6b shows the MUA for an example population from synchronized A1 across repeated presentations of two different speech tokens. Each row of the image shows the MUA for one trial, and the trials are ordered by the time of the earliest activity. There were very few trials in which the tokens evoked no response (median value: 4% of trials across 7 populations each with between 12 and 18 different tokens for total n = 96). In most trials, either the response to the onset of the token occurred during an ongoing up state (median value: 43% of trials) or the onset of the token triggered an up state (median value: 50% of trials).

We repeated the analyses of population spike patterns described in the previous section after separating trials in which the response to a token occurred during an ongoing up state from those in which the token triggered an up state. Whether considering the similarity in the spike patterns evoked by different sounds (Fig. 6.6c), noise correlations (Fig. 6.6d), or decoding performance (Fig. 6.6e), the differences between different classes of responses in synchronized A1 were small, and the differences between synchronized and desynchronized A1 were large. Surprisingly, although the differences between the different classes of responses in synchronized A1 were small, the responses on trials in which an up state was

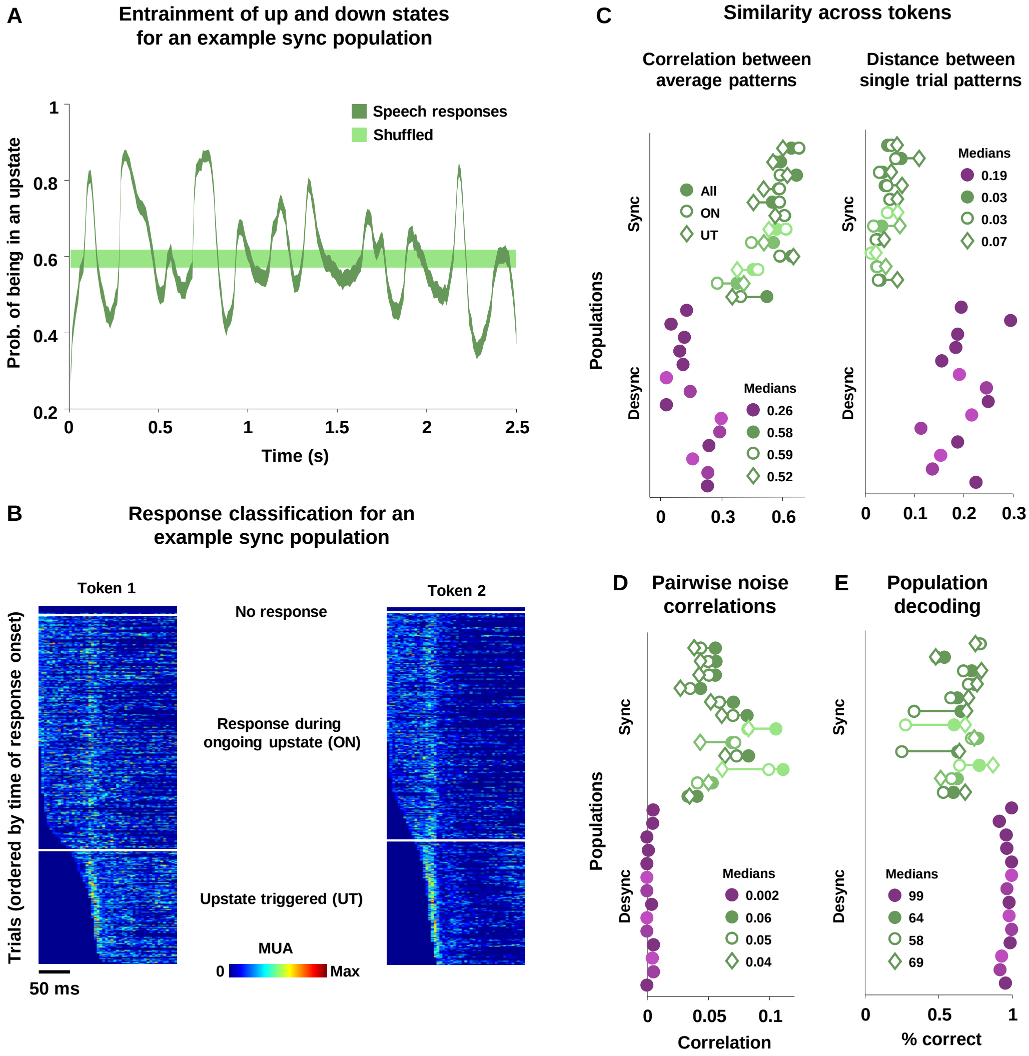

Figure 6.6: (Caption next page.)

Figure 6.6: (Previous page.) **Spike patterns evoked by different speech tokens in synchronized A1 are similar and have strong noise correlations even within up states a)** The probability of being in an up state in 10 ms time bins for an example population from synchronized A1 during repeated presentations of a short segment of speech. The dark line shows the probabilities for the actual responses. The light line shows the probability computed after shuffling the order of time bins on each trial and indicates the overall probability of being in an up state. The thickness of lines indicate 95**b)** The MUA for an example population from synchronized A1 across repeated presentations of two different speech tokens. Each row of the image shows the MUA for one trial, and the trials are ordered by the time of the earliest activity. Trials were separated into those with no response, those in which the response occurred during an ongoing up state, and those in which the token triggered an up state. **c)** Plots showing the similarity of the spike patterns across speech tokens for each synchronized (green) and desynchronized (blue) population for both responses averaged across trials (left) and single trial responses (right). For trial average similarity, values are the average correlation between the average spike patterns evoked by each pair of tokens. For single trial similarity, values are the average fractional increase in the distance between spike patterns evoked by each pair of tokens relative to the average distance between patterns evoked by the same token. For those populations for which responses were recorded for more than one set of tokens, multiple symbols are shown (darkest color for token set 1, middle color for token set 2, and lightest color for token set 3). The symbols indicate the median value for each population across all pairs of tokens. The median values across all populations are noted on the figure (with each token set for each population treated as a separate measurement). Responses from synchronized A1 were analyzed for all trials (All), trials in which the response occurred during an ongoing up state (OG), and those in which the token triggered an up state (UT). **de)** Plots showing the pairwise noise correlations and the performance of a support vector machine in decoding responses, plotted as in C.

triggered were more like desynchronized responses (i.e. had more diverse spike patterns, weaker noise correlations, and allowed for better decoding performance) than those that occurred during ongoing up states (see figure for population medians, all differences were significant with $p < 0.001$, Wilcoxon signed-rank test).

6.8 Differences between synchronized and desynchronized states in the same population

All of the above results are based on comparing synchronized and desynchronized states in different populations. To confirm that the same state-dependent effects on population coding were also evident when comparing synchronized and desynchronized states within the same population, we recorded from 3 populations under urethane in which A1 exhibited spontaneous fluctuations between synchronized and desynchronized states ([Curto et al., 2009]; [Marguet and Harris, 2011]; [Okun et al., 2012]; [Bermudez Contreras et al., 2013]). Fig. 6.8a shows the spontaneous MUA for an example population over a period of approximately 1 hour (each 10 second trial

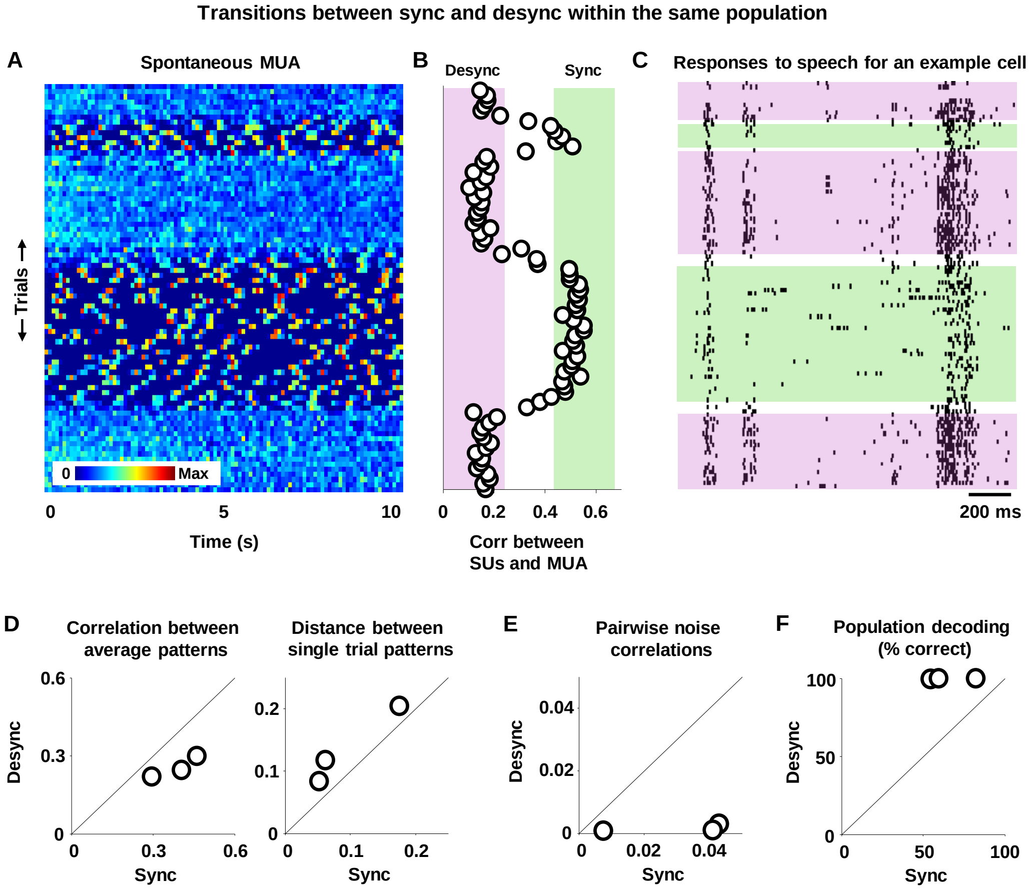

Figure 6.7: (Caption next page.)

Figure 6.8: (Previous page.) **Differences between synchronized and desynchronized states in the same population a)** The spontaneous MUA for an example A1 population under urethane over a period of approximately 1 hour. Each 10 second trial of spontaneous activity was followed by 40 seconds of speech. The MUA was defined as the sum of the activity of all of the individual cells in the population. **b)** The median value of correlation between the spiking of each cell in the population and the MUA for each 10 second trial of spontaneous activity shown in A. The activity of each cell was represented as a spike count vector with 50 ms bins. During periods when the value was less than 0.25, the cortex was classified as desynchronized, and during periods when the value was greater than 0.4, the cortex was classified as synchronized. **c)** Responses of an example cell to repeated presentations of speech in synchronized and desynchronized states. Each row in the raster plots shows the spike times for one trial. The periods during which the cortex was classified as synchronized and desynchronized are indicated by the shading. Only every tenth trial is shown. **d)** Plots showing the similarity of the spike patterns across speech tokens for each of the 3 populations recorded under urethane in synchronized and desynchronized states. For trial average similarity, values are the average correlation between the average spike patterns evoked by each pair of tokens. For single trial similarity, values are the average fractional increase in the distance between spike patterns evoked by each pair of tokens relative to the average distance between patterns evoked by the same token. The median values for each population across all pairs of tokens are shown. **ef)** Plots showing the pairwise noise correlations and the performance of a support vector machine in decoding responses, plotted as in D.

of spontaneous activity was followed by 40 seconds of speech). The transitions between synchronized and desynchronized states for this population were clearly evident in the correlation between the spiking of each cell in the population and the MUA (Fig. 6.8b). We classified the cortical states during each block of speech trials as synchronized or desynchronized based on the surrounding spontaneous activity and repeated the analyses of population spike patterns described above. With respect to the similarity in the spike patterns evoked by different sounds (Fig. 6.8d), noise correlations (Fig. 6.8e), and decoding performance (Fig. 6.8f), the differences between responses in synchronized and desynchronized states for these three populations mirrored those that we observed when comparing states across different populations above.

6.9 Discussion

We have shown that the population coding of speech in A1 depends strongly on cortical state. We found that responses to speech in desynchronized A1 were temporally precise and reliable across trials, with median precision that was three times higher than in synchronized A1. While different speech tokens evoked similar spike patterns in synchronized A1, we found that responses in desynchronized A1 were much more diverse, with similarity in both the spatial structure and the temporal order of spiking across tokens that was approximately half that in synchronized A1. This diversity of spike patterns, together with extremely weak noise correlations, allowed us to decode responses to different speech tokens from desynchronized A1 with nearly perfect performance. These state-dependent differences in the population coding of speech were evident in comparisons both across different populations, as well between synchronized and desynchronized states within the same populations.

Our finding that gerbil A1 has the capacity to represent sounds with high fidelity in the desynchronized state is consistent with behavioral studies in rodents that have demonstrated the essential role of A1 in auditory processing ([Wetzel et al., 1998]; [Cooke et al., 2007]; [Porter et al., 2011]) and learning ([Bao et al., 2004]; [Reed et al., 2011]; [Aizenberg and Geffen, 2013]; [Banerjee and Liu, 2013]). Several previous studies of synchronized and desynchronized rodent A1 have reported differences that are qualitatively consistent with our results. In rats anesthetized with urethane, the change from synchronized to desynchronized states was accompanied by a decrease in the trial-to-trial variability of A1 responses to clicks ([Curto et al., 2009]) and amplitude-modulated noise ([Marguet and Harris, 2011]), as well as a decrease in noise correlations ([Renart et al., 2010]). A study in awake rats found that the temporal order of population spiking was conserved across synchronized and desynchronized states ([Luczak et al., 2013]), which may seem inconsistent with our finding that the temporal order of spiking was similar across different sounds in synchronized A1, but not in desynchronized A1. However, the comparison by Luzcak et al. was based on the average temporal order across all sounds tested in the two states, rather than on the order for individual sounds as in our study. We also observed a consistent temporal order in desynchronized A1 when averaging across two separate 5 minute segments on ongoing speech (data not shown), but our results show that the intrinsic factors that impose this consistency across sounds provide only a weak constraint on the temporal order in responses to any particular sound.

Another study in awake rats found that A1 responses in engaged animals were suppressed relative to those in passive animals ([Otazu et al., 2009]). While this study did not explicitly measure cortical state, the results of previous studies suggest that engaged and passive behavioral conditions in rodents are typically associated with desynchronized and synchronized states, respectively ([Harris and Thiele, 2011]). Our data are consistent with the results of Otazu et al.; the average spike rates in responses to speech were lower in desynchronized A1 than in synchronized A1 (median values: 5.2 spikes/s for synchronized, n = 245, 3.3 spikes/s for desynchronized, n = 284).

Our results differ from those of previous studies with respect to differences between activity in desynchronized cortex and activity during up states in synchronized cortex. Previous studies have shown that membrane potential dynamics during up states in anesthetized animals are similar to those during prolonged periods of desynchronization in awake animals, suggesting that up states may be equivalent to brief periods of desynchronization ([Destexhe et al., 2007];[Castro-Alamancos, 2009]). Our results argue against this hypothesis, at least at the level of population spike patterns, as restricting our analysis of synchronized A1 to activity within up states had little impact on our results. Our finding that noise correlations in synchronized A1 persist even when only up states are considered also differ from those of recent studies that have shown that noise correlations within up states in synchronized cortex are weak ([Renart et al., 2010]; [Ecker et al., 2014]). The anesthetic used to achieve a synchronized state in our study (ketamine/xylazine) differed from those used in the other studies (sufentanil and urethane) and, while the dynamics of up and down states induced by these different anesthetics appear to be similar, there may be other, more subtle differences in their effects on network dynamics that impact noise correlations. To resolve these discrepancies, further studies of population activity across different synchronized states are required.

Our results add to a growing body of evidence demonstrating the importance of cortical state for sensory processing ([Harris and Thiele, 2011]). Early evidence suggested that the interactions between spontaneous and evoked activity in the synchronized state were additive ([Arieli et al., 1996]; [Azouz and Gray, 2003]; [Ringach, 2009]), but recent studies have shown that these interactions can be much more complex, with sensory inputs causing transitions between up and down states and intrinsic dynamics placing strong constraints on activity patterns ([MacLean et al., 2005]; [Hasenstaub et al., 2007]; [Rigas and Castro-Alamancos, 2007]; [Curto et al., 2009]; [Luczak et al., 2009]; [Luczak et al., 2013]; [Bathellier et al., 2012]). The ability of stimulus onsets to trigger an up state may facilitate the detection of stimulus onsets; indeed, in our sample of populations in synchronized A1, trials in which the onset of a speech token triggered an up state contained an average of 18% more spikes than those in which responses occurred during an ongoing upstate ($p < 0.001$, Wilcoxon signed-rank test). Recent studies have also provided evidence that network dynamics can aid in the processing of ongoing stimuli. For example, the entrainment of slow rhythms in A1 has been shown to facilitate the processing complex sound streams ([Kayser et al., 2009]; [Giraud and Poeppel, 2012]; [Lakatos et al., 2013]; [Zion Golumbic et al., 2013]) and our finding that the dynamics of up and down states in synchronized A1 are entrained by speech are consistent with these results. Thus, rather than simply reflecting a general suppression of network dynamics, the high fidelity representation of sounds that we observed in desynchronized A1 may result from network dynamics being strongly driven by sound rather than by intrinsic sources. Elucidating the role of network dynamics in desynchronized cortex and characterizing how they interact with sensory inputs are challenges for future studies.

6.10 Materials and Methods

Low frequency local field potential power: The low frequency power in the LFP for each population was measured from spontaneous activity (sound 1 described above). For each tetrode on the array, the voltage signals were averaged across the 4 channels. For each of these tetrode signals, the power spectrum was computed using Welch's averaged, modified periodogram method for 6 s segments with 50 % overlap. The low frequency power was measured as the sum of the power between 1 and 20 Hz. The values reported for each population are the average across the 8 tetrodes on the array. The units associated with the reported values are arbitrary, but are the same for all populations.

Correlation between single-unit spiking and multi-unit activity in spontaneous activity: The degree of concerted spiking in each population was measured from spontaneous activity (sound 1 described above) as the average value of the correlation between spiking of each cell and the MUA. The activity of each cell was represented as a spike count vector with 50 ms bins. The MUA for each population was defined as the sum of the activity of all of the individual cells in the population. The correlation between the single-unit spiking and MUA in spontaneous activity was used to classify the cortical state as synchronized or desynchronized for urethane experiments: during periods when the value was less than 0.25, the cortex was classified as desynchronized, and during periods when the value was greater than 0.4, the cortex was classified as synchronized.

Tone responsiveness: Responses to tone set 2 (sound 3 described above) were evaluated in two ways: 1) the fraction of cells in each population that responded significantly (average spike rate more than 2 standard deviations above average spontaneous rate) to the best frequency for that population (i.e. the frequency that evoked a significant response from the largest fraction of cells), and 2) the fraction of cells that responded significantly to at least one of the frequencies tested.

Frequency tuning width: The width of the frequency tuning curve for each cell was measured from responses to tone set 1 (sound 2 described above) at 56 dB SPL as the range of frequencies for which the spike rate averaged over all trials was at least half of its maximum value. Spontaneous spike rates were not subtracted before measurement.

Direction selectivity: The direction selectivity index (DSI) for each cell was measured from responses to FM tones (sound 4 described above). For each of the six FM speeds, the direction selectivity index was measured from the average spike rate of responses to the six speeds as (highest rate - lowest rate) / (highest rate + lowest rate). The DSI reported for each cell is the higher of the values measured for the two directions. Spontaneous spike rates were not subtracted before measurement.

Speed selectivity: The speed selectivity index (SSI) for each cell was measured from responses to FM tones (sound 4 described above). For each of the two FM directions, the speed selectivity index was measured from the average spike rate of responses to the two directions as (higher rate - lower rate) / (higher rate + lower rate). The SSI reported for each cell is the highest that was measured for the two directions. Spontaneous spike rates were not subtracted before measurement.

Temporal precision: The critical level of spike timing precision for each cell was measured from responses to speech (sound 5 described above) using a method that we have described previously (Garcia-Lazaro et al., 2013). The responses for each cell were represented as binary vectors with 2 ms bins and the single spike information (Brenner et al., 2000) was measured as described below. The original spike times were then jittered by adding noise drawn from a uniform distribution and the information was recomputed. The critical level of precision was defined as the amount of jitter (i.e. the width of the noise distribution) that reduced the information in the responses to 95% of its original value.

Reliability: The reliability of responses across trials for each cell was measured from responses to speech (sound 5 described above) using a method that we have described previously (Sahani and Linden, 2003). To quantify reliability, we measured the signal to noise ratio (SNR) defined as the ratio of unbiased estimates of the signal (repeatable) and noise (not repeatable) response power with responses represented as binary vectors with 2 ms bins.

Information throughput and efficiency: The mutual information between the stimulus and the responses of each cell was measured from responses to speech (sound 5 described above). The mutual information between two variables measures how much the uncertainty about the value of one variable is reduced by knowing the value of the other. The mutual information between a sensory stimulus and a neural response can be computed as the difference between the entropy of the response before and after conditioning on the stimulus:

$$I(r;s) = H(r) - H(rs) = -\sum_r p(r)\log_2 p(r) + \sum_s p(s)\sum_r p(r)\log_2 p(r)$$

To measure the information that is carried by spike trains about speech without having to specify which features of the speech were relevant, we used the approach pioneered by Strong et al. (Strong et al., 1998) of discretizing a continuous stimulus into separate 'stimuli' in time. To measure information, the total entropy of the response is compared to the average entropy of the response in each time bin (the 'noise' entropy):

$$I(r;s) = H(r) - H(rt) = -\sum_r p(r)\log_2 p(r) + \langle\sum_r p(r(t))\log_2 p(r(t))\rangle_t$$

We measured the single spike information for each cell, which is equivalent to the information in the PSTH (Brenner et al., 2000), by representing responses as binary vectors with 2 ms bins and computing the information in single bin 'words'. All information calculations were performed using the Direct Method via infoToolbox for Matlab (Magri et al., 2009) with bias correction via the shuffling method and quadratic extrapolation (Panzeri et al., 2007). The stability of all calculations was verified by ensuring that the values obtained using only half of the recorded trials differed from those obtained using all trials by less than 5%.

Spike pattern similarity: The similarity of the spike patterns evoked by different speech tokens for each population was measured from responses to speech (sound 5 described above). From each 2.5 s segment of speech, responses to seven 0.25 s tokens were extracted. The responses of each population to each trial of each token were represented as binary matrices with rows corresponding to cells and columns corresponding to 10 ms time bins (see figure 4A). The similarity of trial-averaged spike patterns was measured as the average value of the correlation between the average responses across all pairs of tokens. The similarity of single trial spike patterns was measured as the fractional increase in the average value of the Euclidean distance between the responses across all pairs of tokens relative to the average value of the Euclidean distance between spike patterns evoked by the same token.

The similarity of the spatial structure of the spike patterns was measured following the approach of Luczak et al. (Luczak et al., 2009). The spatial structure of spiking for each token was measured as the set of correlations between the responses of each pair of cells (i.e. the correlations between the rows of the binary response matrices). The similarity of the spatial structure across tokens was measured as the average value of the correlation between the set of pairwise correlations for all pairs of tokens.

The similarity of the temporal order of the spike patterns was measured following the approach of Luczak et al. (Luczak et al., 2009). The responses of each cell to each trial of each token were represented as binary vectors with 1 ms bins. The MUA for each population was defined as the sum of the activity of all of the individual cells in the population. The temporal order of spiking for each token was measured as the set of latencies obtained by taking the center of mass of the correlation function between each cell and the MUA (after smoothing with a Gaussian window with a width of 8 ms). The similarity of the temporal order was measured as the average value of the correlation between the sets of latencies for all pairs of tokens.

Noise correlations: The noise correlations between each pair of cells in each population were measured from responses to speech (sound 5 described above). The response of each cell to each trial was represented as a binary vector with 10 ms time bins. The total correlation for each pair of cells was obtained by computing the correlation coefficient between the actual responses. The signal correlation was computed after shuffling the order of repeated trials for each time bin. The noise correlation was obtained by subtracting the signal correlation from the total correlation.

Population decoding: A support vector machine was trained (using the LIBSVM package from http://www.csie.ntu.edu.tw/c̃jlin/libsvm with default parameters) to decode the single trial responses of each population to speech (sound 5 described above). From each 2.5 s segment of speech, responses to seven 0.25 s tokens were extracted. The responses of each population to each trial of each token were represented as binary matrices with rows corresponding to cells and columns corresponding to 10 ms time bins (see figure 4A). The classifier was trained on responses to 75% of trials and used to predict which token evoked the responses on other 25% of trials. The values reported for each population are the average performance obtained using 10 different subsets of trials for training and prediction. To test the effects of noise correlations on decoding, the order of repeated trials for each cell for each time bin were shuffled before training and prediction.

Classification of up and down states: To classify up and down states in synchronized A1, the MUA was computed as described above and represented as a spike count vector with 10 ms time bins. The MUA was filtered with a 10 bin median filter and the population was considered to be in an up state in any bin in which the filtered MUA was greater than zero.

Separation of trials in which the response to a speech token occurred during an ongoing up state from those in which the token triggered an up state: For responses to speech in synchronized A1, the MUA was computed as described above and represented as a spike count vector with 5 ms time bins. The MUA was filtered with a 3 bin median filter and, for each token, the time of the first peak in the mean MUA across trials that was a least 75% as large as the maximum overall value was determined. Trials in which there was no activity within ?25 ms of this peak were ignored. For the remaining trials, if there was any activity in the period from 75 ms to 25 ms before this peak, the response was classified as having occurred during an ongoing up state; otherwise, the response was classified as having triggered an up state.

VII

Learning visual motion in recurrent neural networks

Outline

We present a dynamic nonlinear generative model for visual motion based on a latent representation of binary-gated Gaussian variables. Trained on sequences of images, the model learns to represent different movement directions in different variables. We use an online approximate inference scheme that can be mapped to the dynamics of networks of neurons. Probed with drifting grating stimuli and moving bars of light, neurons in the model show patterns of responses analogous to those of direction-selective simple cells in primary visual cortex. Most model neurons also show speed tuning and respond equally well to a range of motion directions and speeds aligned to the constraint line of their respective preferred speed. We show how these computations are enabled by a specific pattern of recurrent connections learned by the model.

7.1 Introduction

Perhaps the most striking property of biological visual systems is their ability to efficiently cope with the high bandwidth data streams received from the eyes. Continuous sequences of images represent complex trajectories through the high dimensional and nonlinear space of two dimensional images. The survival of animal species depends on their ability to represent these trajectories efficiently and to distinguish visual motion on a fast time scale. Neurophysiological experiments have revealed complicated neural machinery dedicated to the computation of motion [Mikami et al., 1986]. In primates, the classical picture of the visual system distinguishes between an object-recognition-focused ventral pathway and an equally large dorsal pathway for object localization and visual motion. Here we propose a model for the very first cortical computation in the dorsal pathway: that of direction-selective simple cells in primary visual cortex [Livingstone, 1998]. We continue a line of models which treats visual motion as a general sequence learning problem and proposes asymmetric Hebbian rules for learning such sequences [Abbott and Blum, 1996, Rao and Sejnowski, 2000]. We reformulate these earlier models in a generative probabilistic framework which allows us to train them on sequences of natural images. For inference we use an online approximate filtering method which resembles the dynamics of recurrently-connected neural networks.

Many previous low-level generative models of image sequences have treated time as a third dimension in a sparse coding problem [Olshausen, 2003]. These approaches have thus far been difficult to map to neural architecture as they have been implemented with noncausal inference algorithms. Furthermore, the spatiotemporal sensitivity of each learned variable is determined by a separate three-dimensional basis function, requiring very many variables to encode all possible orientations, directions of motion and speeds. Cortical architecture points to a more distributed formation of motion representation, with temporal sensitivity determined by the interaction of neurons with different spatial receptive fields. Another major line of models of video analyzes the slowly changing features of visual input and proposes complex cells as such slow feature learners

[Berkes et al., 2009], [Wiskott and Sejnowski, 2002]. However, these models are not expressive enough to encode visual motion and are more specifically designed to encode image dimensions invariant in time.

A recent hierarchical generative model for mid-level visual motion separates the phases and amplitudes of complex coefficients applied to complex spatial basis functions [Cadieu and Olshausen, 2009]. This separation makes it possible to build a second layer of variables that specifies a distribution on the phase coefficients alone. This second layer learns to pool together first layer neurons with similar preferred directions. The introduction of real and imaginary parts in the basis functions is inspired by older energy-based approaches where pairs of neurons with receptive fields in quadrature phase feed their outputs with different time delays to a higher-order neuron which thus acquires direction selectivity. However, the model of Cadieu and Olshausen, and models based on motion energy in general, do not reproduce direction-selective *simple* cells. Here we propose a network in which local-motion computation is calculated in a more distributed fashion than is postulated by feedforward implementations of energy models.

7.1.1 Recurrent Network Models for Neural Sequence Learning.

Another view of the development of visual motion processing sees it as a special case of the general problem of sequence learning [Dayan and Abbott, 2001]. Many structures in the brain seem to show various forms of sequence learning, and recurrent networks of neurons can naturally produce learned sequences through their dynamics [Barber, 2002, Brea et al., 2011]. Indeed, it has been suggested that the reproduction of remembered sequences within the hippocampus has an important navigational role. Similarly, motor systems must be able to generate the sequences of control signals that drive appropriate muscle activity. Thus many neural sequence models are fundamentally generative. By contrast, it is not evident that V1 should need to reproduce the learned sequences of retinal input that represent visual motion. Although generative modelling provides a powerful mathematical device for the construction of inferential sensory representations, the role of actual generation has been debated. Is there really a potential connection then, to the generative sequence reproduction models developed for other areas?

One possible role for explicit sequence generation in a sensory system is for prediction. Predictive coding has indeed been proposed as a central mechanism to visual processing [Rao and DH, 1999] and even as a more general theory of cortical responses [Friston, 1999]. More specifically, as a visual motion learning mechanism, sequence learning forms the basis of an earlier simple toy but biophysically realistic model based on STDP at the lateral synapses in a recurrently connected network [Rao and Sejnowski, 2000]. In another biophysically realistic model, recurrent connections are set by hand rather than learned, but they produce direction selectivity and speed tuning in simulations of cat primary visual cortex [Douglas et al., 1995]. Thus, the recurrent mechanisms of sequence learning may indeed be important. In the next section, we give a short demonstration of the history-dependent dynamical computations which can be implemented by a network of linear neurons with instantaneous feedforward visual input. The rest of the paper will elaborate the learning mechanisms that might lead to such representations. We will mathematically define a probabilistic sequence modelling network which can learn patterns of visual motion in an unsupervised manner from 16 by 16 patches with 512 latent variables connected densely to each other in a nonlinear dynamical system.

7.2 Linear neurons with recurrent connectivity enable history-dependent computations

Figure 7.2a shows examples of typical spatiotemporal receptive fields used to model the responses of cortical visual neurons. They consist of an independent filter estimated for each of a number of timelags between a presented stimulus and the neural response. Because neurons respond to specific spatiotemporal features of visual images, stimuli presented tens and up to hundreds of milliseconds in the

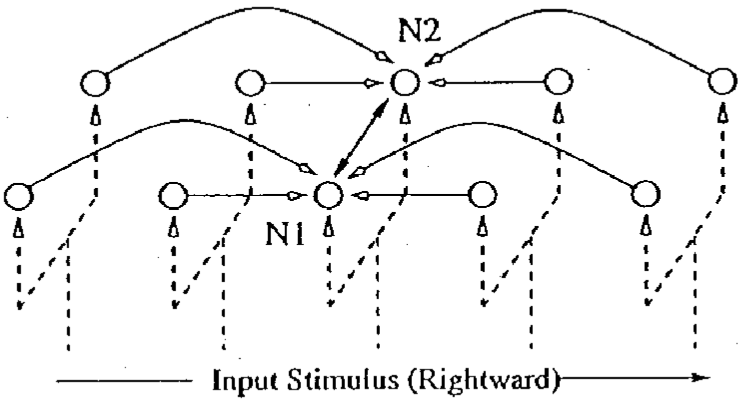

Figure 7.1: Toy sequence learning model with biophysically realistic neurons (from [Rao and Sejnowski, 2000]). Neurons N1 and N2 have the same RF as indicated by the dotted line, but after STDP learning of the recurrent connections with other neurons in the chain, N1 and N2 learn to fire only for rightward and leftward motion.

past can affect their activity. The filters shown in figure 7.2a have been obtained from the Gabor function, a well-known parametric model of spatial receptive fields, which has been shifted spatially at constant speeds in fixed directions. They can be used to compute a receptive field's response to an external stimulus in a similar dot-product computation represented graphically in figure 7.2b.

Although spatiotemporal filters are popular representations of V1 neuron receptive fields, such representations have little computational appeal, as well as little documented biophysical evidence. Firstly, spatiotemporal receptive fields require the specification of a different filter for every timelag in the past a neuron wants to consider, which results in an unnecessarily large number of feedforward connections that have to be learned or specified. Secondly, the computation requires lagged copies of inputs to be kept available for durations of up to hundreds of milliseconds. Although it has been suggested that these lagged inputs are relayed by the LGN ([]), lagged LGN neurons have proved to be elusive and not very well represented. In addition, lagged LGN cells would be a poor choice of storage location for the lagged stimulus copies, as the LGN has few neurons available and the optical radiation already presents a bottleneck of information transmission, before and after the thalamus. No evidence of true delay lines has been found in cortex yet.

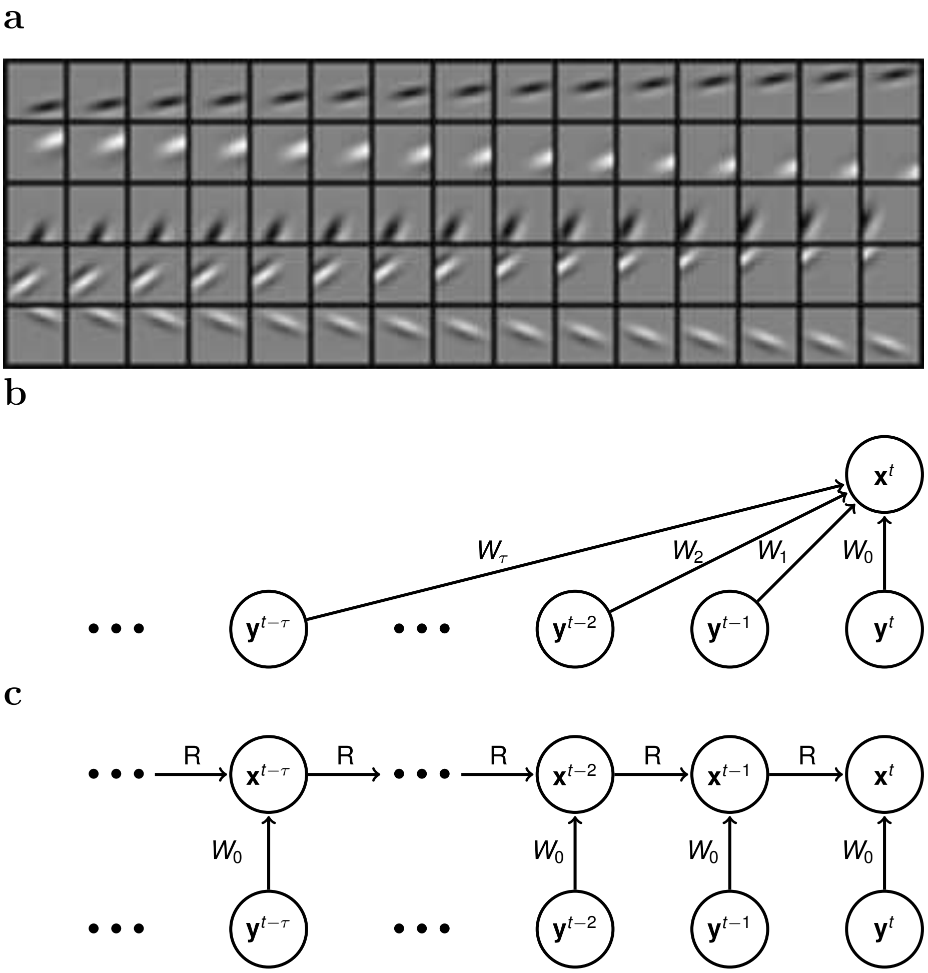

Figure 7.2: **Conversion from a bank of spatio-temporal receptive fields to a recurrent network with instantaneous inputs**. **a)** Five filters out of a bank of 1,024 randomly-drawn Gabor spatio-temporal filters. The spatial parameters of the Gabors were chosen randomly from distributions that qualitatively match reported simple cell receptive fields, while the speeds of movements were also drawn independently from a kurtotic distribution with many receptive fields moving relatively slowly, also in agreement with the relative preference of simple cells to slow motion. **b)** Schematic of the feedforward computation where the variable $\boldsymbol{x}_t$ represents the output of a simple cell at time t that receives feedforward input from lagged retinal/LGN cells at many previous temporal lags. **c)** Schematic of a computation performed intrinsically by the network. The activity of a population of neurons $\boldsymbol{x}_t$ depends not only on the instantaneous input, but also on the recent activities of the population $\boldsymbol{x}_{t-1}$.

However, an alternative computation that produces the same output can be devised, as represented graphically in figure 7.2c. Since neurons are recurrently highly inter-connected in cortex, it is possible to use the dynamics they create to store the relevant information required to estimate the same spatiotemporal patterns. Intuitively, if we discretize time in 10 ms bins, the activity of neurons at time t is available for computations at time $t + 1$. If at time t the activity of neurons represents a function of the stimulus many timepoints in the past, by propagation the activity of neurons at time $t+1$ will also represent the past stimulus. In addition, the instantaneous thalamic input will bring new information about the current spatial stimulus which can be integrated with the old information to produce an estimate of the linear spatiotemporal receptive field. Such a solution to history-dependent computations in visual cortex does not require lagged copies of the input, has fewer parameters than the purely feedforward filters, can integrate inputs over long periods of time and actually has reduced computational complexity, in terms of how many addition/multiplication operations have to be executed per second (flops). At the end of this section we will give a back of the envelope calculation of the orders of magnitude complexity of the two proposed computations.

The equations below show a simple derivation that can reparametrize any given set of spatiotemporal basis functions (such as those shown in 7.2) to a set of parameters used in a linear recurrent neural network with instantaneous input filters W_0 and recurrent pairwise connections R. Although the transformation is not biophysically motivated, it serves to show a mathematical correspondence between the two solutions to visual-history dependence discussed above.

Consider parametrizing the a full set of 1,024 spatiotemporal receptive fields by their spatial receptive fields (2-dimensional, n_{pix} by n_{pix}) at all timelags (a 3rd dimension). We can vectorize the 2-dimensional filters into a single one-dimensional vector with $n_{pix} * n_{pix}$ entries and cumulate all filters at time t from the entire population of 1,024 neurons into a matrix of size n_{pix}^2 by 1,024 and call this matrix W_t. Similarly we obtained $[W_1, W_2, ... W_t ...]$. The linear response of the population of 1,024 neurons can be represented by a 1,024-dimensional vector

$\boldsymbol{x}_t$ that is computed as the following sum

$$\boldsymbol{x}^t = \sum_{\tau=0}^{\infty} \boldsymbol{W}_\tau \ \boldsymbol{y}^{t-\tau}$$

We make the following ansatz: each of these timelagged matrices W_t can be rewritten in terms of single recurrent matrix R and the initial feedforward matrix at instantaneous timelag W_0.

$$\boldsymbol{W}_\tau = (\boldsymbol{R})^\tau \ \ \boldsymbol{W}_0$$

The sum computed in variable x_t can now be rewritten as follows

$$\boldsymbol{x}^t = \boldsymbol{W}_0 \ \boldsymbol{y}^t + \boldsymbol{R} \ \sum_{\tau=0}^{\infty} (\boldsymbol{R})^\tau \ \ \boldsymbol{W}_0 \ \boldsymbol{y}^{t-1-\tau}$$
$$\boldsymbol{x}^t = \boldsymbol{W}_0 \ \boldsymbol{y}^t + \boldsymbol{R} \ \boldsymbol{x}^{t-1}$$

The last equation exactly represents a linear recurrent neural network, with instantaneous feedforward input $W_0\boldsymbol{y}_t$ and recurrent matrix connectivity R. Although we have made the ansatz such that each W_t should be rewritten as $\boldsymbol{W}_\tau = (\boldsymbol{R})^\tau \ \ \boldsymbol{W}_0$, such a matrix R may not generally exist. However, under mild assumptions it can be shown that any finite set of sufficiently many spatiotemporal receptive fields can be reparametrized with a matrix R. Instead of showing the proof, below we show that the reparametrization is easy to obtain under more practical concerns of a finite and relatively small number of spatiotemporal filters (1024). Under such conditions the reparametrization will not be perfect, but the representation error is sufficiently small to be negligible.

Specifically, we can solve for $\boldsymbol{R}$ by linear regression

$$\boldsymbol{W}_1 \approx \boldsymbol{R} \ \boldsymbol{W}_0$$
$$\boldsymbol{W}_2 \approx \boldsymbol{R} \ \boldsymbol{W}_1$$
$$\dots$$
$$+ \text{L1-regularization}$$

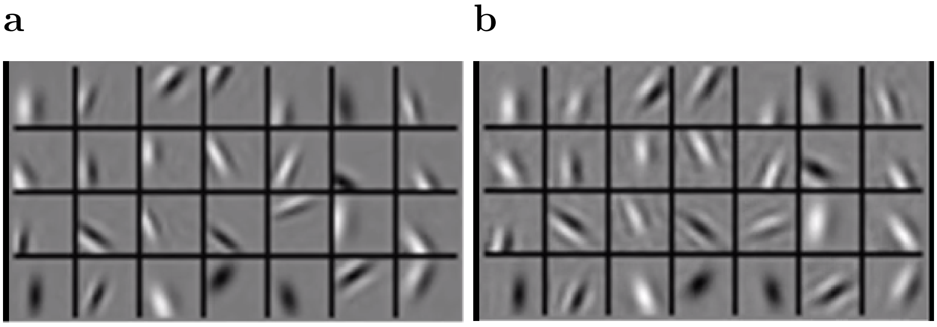

Figure 7.3: **Spatial reconstructions of the bank of filters with intrinsic representations of the recurrent dynamics.** **a)** The reconstructed spatial filters at short timelags (10 frames into the past) are exact. **b)** The reconstructions at longer timelags (20 frames into the past) are relatively more noisy and begin developing ripples. In general, the quality of the reconstructions is a function of the number of recurrent connections in the network that can store information.

Already this offers sufficiently exact matrices R to reconstruct the entire spatiotemporal profiles of the population at all timelags starting just with the feedforward filter W_0, but it does not maximize the representational capacity of the network because approximation errors from each independent linear regression add up over each consecutive application of the matrix R to the ongoing product $R^t \boldsymbol{W}_{t-1}$. A more exact solution can be obtained by solving the complete linear regression equations

$$\begin{aligned}
\boldsymbol{W}_1 &\approx \boldsymbol{R}\ \boldsymbol{W}_0 \\
\boldsymbol{W}_2 &\approx \boldsymbol{R} * R\ \boldsymbol{W}_0 \\
\boldsymbol{W}_3 &\approx \boldsymbol{R} * R * R\ \boldsymbol{W}_0 \\
&\ldots \\
&+ \text{L1-regularization}
\end{aligned}$$

We won't detail or emphasize here the nature of the fitting procedure, except to say that it resembles closely the backpropagation through time optimization procedure used to fit recurrent linear models to neural population data in an earlier section. Figures 7.3a and b show the reconstructed spatial filters for a few selected neurons at timelags of 10 and 20 frames. Note that the reconstruction is perfect at 10 frames in the past, but begins to degrade at 20 frames, with some

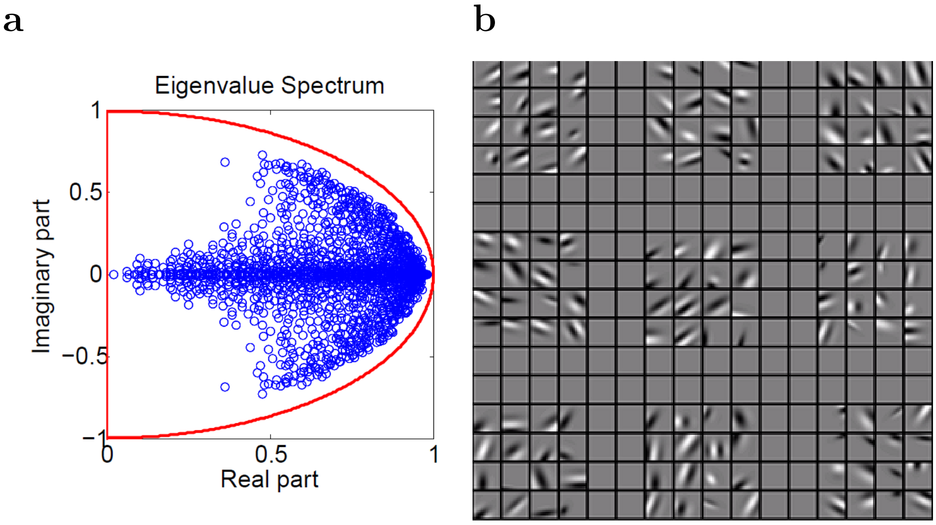

Figure 7.4: **Properties of recurrent connections. a)** The eigenvalue decomposition of the recurrent matrix shows a large number of eigenvalues close to 1, which result in long timescales in spatiotemporal filters. Such long timescales can generate spatial selectivity of a target cell at timelags of 10-20 frames and thus maintain stimulus-information for extended periods of time.**b)** We can directly inspect what pairs of neurons wire together by looking at their spatiotemporal receptive fields. Neurons with similar preferred directions and orientations wired together preferentially. The figure shows only the instantaneous receptive fields of 9 groups of neurons with the strongest connections to 9 target neurons (always shown as the first neuron in the group). All neurons in the same group have similar receptive field properties, and the target receptive field is a linear combination of their receptive fields.

obvious rippling introduced into the filters. Eventually, the filters at long timelags degrade even more, but they do so in a relatively smooth manner, eventually degrading to 0 because we have penalized the magnitude of the connections R. We should also emphasize the particular fits shown in 7.3 have been performed with large $L1$ regularization penalties on the parameters, for the purpose of obtaining a sparse R matrix with less than 5% overall connectivity (which may more faithfully represent the regime of computation by realistic neural networks in the cortex). Allowing full and unpenalized connectivity with as little as 1,024 neurons allowed the 1,024 by 1,024 matrix R to reconstruct almost any basis of spatiotemporal filters we empirically tried. Can we learn anything from the matrix of pairwise connections R determined in this fashion? Figure 7.4a shows the eigenvalue spectrum of a typical matrix R fit with the optimization procedure detailed above. Most eigenvalues are relatively close to 1, which indicates long timescales present in the dynamics of the linear recurrent network. The complex parts of the eigenvalues show that the dynamics are not merely relaxing over time but in fact gradually shifting the stimulus representation from one eigenvector to its pair. Direction-selective simple cells have previously been proposed and implemented with complex-valued basis functions by [Cadieu and Olshausen, 2009] specifically to allow responses to rotate across the support vectors provided by the instantaneous receptive field and its 90° phase-shifted pair. Our implementation provides a more realistic representation in terms of scalar real-valued quantities that can in fact be represented by the brain.

Figure 7.4b illustrates the types of neurons with large recurrent connections in the matrix R. Each of the 9 groups of neurons shown represents the most strongly-connected neurons to a target randomly chosen neuron (always shown as the first neuron in the group). The figure shows only the spatial profiles of the connected neurons, but a video of the timecourse of the receptive fields is available at www.gatsby.ucl.ac.uk/marius. The video shows that not only neurons that wire together have similar spatial receptive fields, but they also prefer similar directions of motion. Intuitively, a Hebbian learning rule would account for such connectivity patterns in cortex, although the rest of the paper shows that the details of the connectivity patterns need to be slightly more complicated to allow visual motion direction estimation. Neurons connecting strongly need to prefer similar directions of motion, and to be spatially aligned in the direction of preferred motion of the presynaptic neuron. More details will be provided towards the end of this chapter.

7.2.1 Complexity order for recurrent networks versus feed-forward filters

Floating point operations per second (FLOPS) are an objective measure of the efficiency of an algorithm. We use a similar measure to estimate the efficiency of computing spatiotemporal neural responses from spatiotemporal visual stimuli. Note that matters of efficiency are extremelly important in vision. The raw amount of visual information available to the senses far exceeds even the computational capacity of the brain and only by selective attention (not discussed in this thesis) can it be well encoded by the brain. Neurons in the fovea and up to 5° of the visual field represent less than 1° portions of visual space, and many columns of neurons need to be replicated throughout striate visual cortex to cover the entire visual space. Finally, direction-selectivity is just one of the many functions of V1 neurons. Orientation selectivity, color processing and spatial invariance are also qualities of images that are important for visual perception.

Suppose the spatiotemporal filters are l_x by l_y by n_t in size (space x space x time, a typical example would be 12 x 12 x 30). A full V1 column may employ a number on the order of $N = 1{,}024$ spatiotemporal filters. The number of feedforward operations necessary to compute the dot-product between the filters and the feedfoward input is thus $2Nl_x^2l_y^2n_t$. In contrast, the number of recurrent operations necessary for the same computation is $2N^2 + 2Nl_x^2l_y^2$. The second term in this sum is smaller than the number of feedforward operations by a factor of n_t, which could be up to 30 (assuming 5ms bins and history-dependence for up to 150ms in the past). The first term may in principle be large, but as discussed above recurrent connectivity in cortex is sparse, hence the total number of non-zero connections in the matrix R may be a small fraction of all possible connections, reducing $2N^2$ to $2pN^2$ with p the probability of connection between all pairs of neurons. Sparse connectivity does not impair the quality of the representation, because only neurons with similar spatio-temporal receptive fields need to be wired together.

We thus see that the computational complexity of recurrent neural networks is much reduced compared to simple linear spatiotemporal filters. This advantage mimics the advantage offered by so-called IIR (infinite impulse response) filters over FIR (finite impulse response) filters well-known in the signal processing literature.

The second efficiency concern to any algorithm is its memory requirement. Modern computational hardware improves primarily by making memory access more efficient, and the brain's parallel computational hardware has often been thought to be efficient mostly through its distributed memory systems and the bandwidth of information that travels within and across brain areas continuously. A quick calculation shows that that the memory requirements of recurrent networks are straightforwardly n_t times less than feedforward algorithms, simply because lagged copies of stimulus inputs need to be stored at all.

Another algorithmic advantage to the recurrent network is its relatively small number of parameters. If these parameters are indeed learned or optimized to the statistics of the natural world, then an algorithm with the fewest free parameters would be optimized most quickly and efficiently, and would be able to generalize better to never-before-seen images and sequences of images.

Given the significant computational advantages of using a recurrent network to compute visual motion properties, and given that the brain already has the necessary hardware to implement it (i.e. recurrent connections), it would be surprising if such a solution was not implemented in the brain.

7.3 Probabilistic Recurrent Neural Networks

In this section we introduce the binary-gated Gaussian recurrent neural network as a generative model of sequences of images. This model belongs to the class of nonlinear dynamical systems. Inference methods in such models typically require expensive variational [Minka, 2001] or sampling based approximations [Doucet et al., 2000], but we found that a low cost online filtering method works sufficiently well to learn an interesting model. We begin with a description of binary-gated Gaussian sparse coding for still images and then describe how to define the dependencies in time between variables.

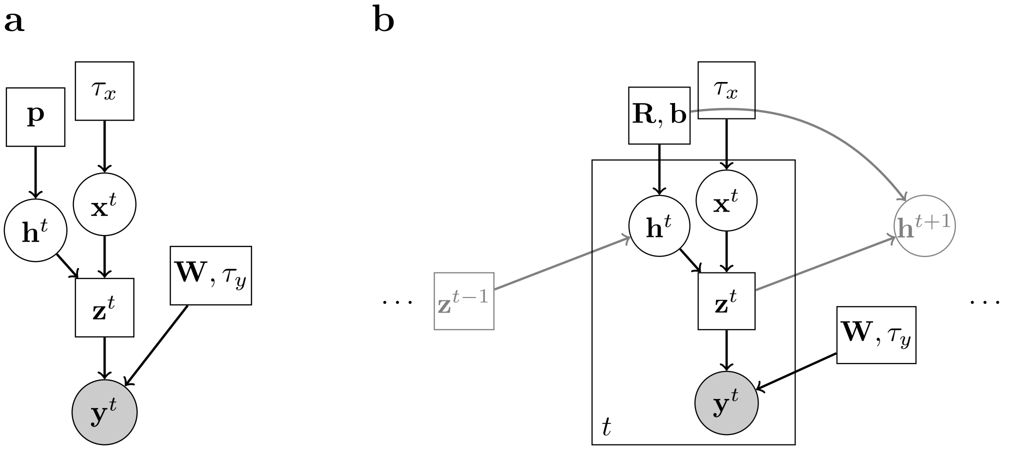

Figure 7.5: **The relationships between variables (neural activities, images/retinal activities) in the graphical models used. a)** Graphical model representation of the generative model of still images. **b)** Graphical model representation of the bgG-RNN with two consecutive time slices. The square box represents that the variable $\mathbf{z}_t$ is not random, but is given by $\mathbf{z}_t = \mathbf{x}_t \circ \mathbf{h}_t$. The parameters describe mean activities and connectivity parameters.

7.3.1 Binary Gated Gaussian Sparse Coding (bgG-SC).

Binary-gated Gaussian sparse coding (also called spike-and-slab sparse coding [Goodfellow et al., 2012] may be seen as a limit of sparse coding with a mixture of Gaussians priors [Olshausen and Millman, 2000] where one mixture component has zero variance. Mathematically, the data $\mathbf{y}^t$ is obtained by multiplying together a matrix $\mathbf{W}$ of basis filters with a vector $\mathbf{h}^t \circ \mathbf{x}^t$, where $\circ$ denotes the operation of Hadamard or element-wise product, $\mathbf{x}^t \in \mathbb{R}^N$ is Gaussian and spherically distributed with standard deviation τ_x and $\mathbf{h}^t \in \{0,1\}^N$ is a vector of independent Bernoulli-distributed elements with success probabilities $\mathbf{p}$. Finally, small amounts of isotropic Gaussian noise with standard deviation τ_y are added to produce $\mathbf{y}^t$.

For notational consistency with the dynamic version of this model, the t superscript indexes time. The joint log-likelihood is

$$\begin{aligned}\mathcal{L}^t_{\mathrm{SC}} = &- \|\mathbf{y}^t - \mathbf{W} \cdot (\mathbf{h}^t \circ \mathbf{x}^t)\|^2/2\tau_y^2 - \|\mathbf{x}^t\|^2/2\tau_x^2 + \\ &+ \sum_{j=1}^{N} \Big(h_j^t \log p_j + (1 - h_j^t) \log{(1 - p_j)} \Big) + \mathrm{const}, \end{aligned} \tag{7.1}$$

where N is the number of basis filters in the model. By using appropriately small activation probabilities $\mathbf{p}$, the effective prior on $\mathbf{h}^t \circ \mathbf{x}^t$ can be made arbitrarily sparse. Probabilistic inference in sparse coding is intractable but efficient variational approximation methods exist. We use a very fast approximation to MAP inference, the matching pursuit algorithm (MP) [Mallat and Zhang, 1993]. Instead of using MP to extract a fixed number of coefficients per patch as usual, we extract coefficients for as long as the joint log-likelihood increases. Patches with more complicated structure will naturally require more coefficients to code. Once values for $\mathbf{x}^t$ and $\mathbf{h}^t$ are filled in, the gradient of the joint log likelihood with respect to the parameters is easy to derive. Note that x_k^t for which $h_k^t = 0$ can be integrated out in the likelihood, as they receive no contribution from the data term in 7.1. Due to the MAP approximation, only the $\mathbf{W}$ can be learned. Therefore, we set τ_x^2, τ_y^2 to reasonable values, both on the order of the data variance. We also adapted p_k during learning so that each filter was selected by the MP process a roughly equal number of times. This helped stabilise learning, avoiding a tendency to very unequal convergence rates.

When applied to whitened small patches from images, the algorithm produced localized Gabor-like receptive fields as usual for sparse coding, with a range of frequencies, phases, widths and aspect ratios. We found that when we varied the average number of coefficients recruited per image, the receptive fields of the learned filters varied in size. For example with only one coefficient per image, a large number of filters represented edges extending from one end of the patch to the other. With a large number of coefficients, the filters concentrated their mass around just a few pixels. With even more coefficients, the learned filters gradually became Fourier-like.

During learning, we gradually adapted the average activation of each variable h_k^t by changing the prior activation probabilities p_k. For 16x16 patches in a twice overcomplete SC model (number of filters = twice the number of pixels), we found that learning with 10-50 coefficients on average prevented the filters from becoming too much or too little localized in space.

7.3.2 Binary-Gated Gaussian Recurrent Neural Network (bgG-RNN).

To obtain a dynamic hidden model for sequences of images $\{\mathbf{y}^t\}$ we specify the following conditional probabilities between hidden chains of variables $\mathbf{h}^t, \mathbf{x}^t$:

$$\begin{aligned}\mathbf{P}\left(\mathbf{x}^{t+1}, \mathbf{h}^{t+1}|\mathbf{x}^t, \mathbf{h}^t\right) &= \mathbf{P}\left(\mathbf{x}^{t+1}\right)\mathbf{P}\left(\mathbf{h}^{t+1}|\mathbf{h}^t \circ \mathbf{x}^t\right)\\ \mathbf{P}\left(\mathbf{x}^{t+1}\right) &= \mathcal{N}\left(\mathbf{0}, \tau_x^2 \mathrm{I}\right)\\ \mathbf{P}\left(\mathbf{h}^{t+1}|\mathbf{h}^t \circ \mathbf{x}^t\right) &= \sigma\left(\mathbf{R}\cdot\left(\mathbf{h}^t \circ \mathbf{x}^t\right) + \mathbf{b}\right), \end{aligned} \tag{7.2}$$

where $\mathbf{R}$ is a matrix of recurrent connections, $\mathbf{b}$ is a vector of biases and σ is the standard sigmoid function $\sigma(a) = 1/(1 + \exp(-a))$. Note how the $\mathbf{x}^t$ are always drawn independently while the conditional probability for $\mathbf{h}^{t+1}$ depends only on $\mathbf{h}^t \circ \mathbf{x}^t$. We arrived at these designs based on a few observations. First, similar to inference in SC, the conditional dependence on $\mathbf{h}^t \circ \mathbf{x}^t$, allows us to integrate out variables $\mathbf{x}^t, \mathbf{x}^{t+1}$ for which the respective gates in $\mathbf{h}^t, \mathbf{h}^{t+1}$ are 0. Second, we observed that adding Gaussian linear dependencies between $\mathbf{x}^{t+1}$ and $\mathbf{x}^t \circ \mathbf{h}^t$ did not modify qualitatively the results reported here. However, dropping $\mathbf{P}\left(\mathbf{h}^{t+1}|\mathbf{h}^t \circ \mathbf{x}^t\right)$ in favor of $\mathbf{P}\left(\mathbf{x}^{t+1}|\mathbf{h}^t \circ \mathbf{x}^t\right)$ resulted in a model which could no longer learn a direction-selective representation. For simplicity we chose the minimal model specified by 7.2. The full log likelihood for the bgG-RNN is $\mathcal{L}_{\text{bgG-RNN}} = \sum_t \mathcal{L}^t_{\text{bgG-RNN}}$ where

$$\begin{aligned}\mathcal{L}^t_{\text{bgG-RNN}} &= \text{const} - \|\mathbf{y}^t - \mathbf{W}(\mathbf{x}^t \circ \mathbf{h}^t)\|^2/2\tau_y^2 - \|\mathbf{x}^t\|^2/2\tau_x^2 + \\ &+ \sum_{j=1}^N h_j^t \log\sigma\left(\mathbf{R}\left(\mathbf{h}^{t-1} \circ \mathbf{x}^{t-1}\right) + \mathbf{b}\right)_j \\ &+ (1 - h_j^t)\log(1 - \sigma\left(\mathbf{R}\left(\mathbf{h}^{t-1} \circ \mathbf{x}^{t-1}\right) + \mathbf{b}\right)_j), \end{aligned} \tag{7.3}$$

where $\mathbf{x}^0 = \mathbf{0}$ and $\mathbf{h}^0 = \mathbf{0}$ are both defined to be vectors of zeros.

7.3.3 Inference and learning of bgG-RNN.

The goal of inference is to set the values of $\hat{\mathbf{x}}^t, \hat{\mathbf{h}}^t$ for all t in such a way as to minimize the objective set by 7.3. Assuming we have already set $\hat{\mathbf{x}}^t, \hat{\mathbf{h}}^t$ for $t = 1$ to T, we propose to obtain $\hat{\mathbf{x}}^{T+1}, \hat{\mathbf{h}}^{T+1}$ exclusively from $\hat{\mathbf{x}}^T, \hat{\mathbf{h}}^T$. This scheme might be called greedy filtering. In greedy filtering, inference is causal and Markov with respect to time. At step $T + 1$ we only need to solve a simple SC problem given by the slice $\mathcal{L}^{T+1}_{\text{bgG-RNN}}$ of the likelihood 7.3, where $\mathbf{x}^T, \mathbf{h}^T$ have been replaced with the estimates $\hat{\mathbf{x}}^T, \hat{\mathbf{h}}^T$. The greedy filtering algorithm proposed here scales linearly with the number of time steps considered and is well suited for online inference. The algorithm may not produce very accurate estimates of the global MAP settings of the hidden variables, but we found it was sufficient for learning a complex bgG-RNN model. In addition, its simplicity coupled with the fast MP algorithm in each $\mathcal{L}^t_{\text{bgG-RNN}}$ slice, resulted in very fast inference and consequently fast learning. In most scenarios we learned models in under 30 minutes on a standard quad core workstation.

Due to our approximate inference scheme, some parameters in the model had to be set manually. These are τ_x^2 and τ_y^2, which control the relative strengths in the likelihood of three terms: the data likelihood, the smallness prior on the Gaussian variables and the interaction between sets of $\mathbf{x}^t, \mathbf{h}^t$ consecutive in time. In our experiments we set τ_y^2 equal to the data variance and $\tau_x^2 = 2\tau_y^2$. We found that such large levels of expected observation noise were necessary to drive robust learning in $\mathbf{R}$.

For learning we initialized parameters randomly to small values and first learned $\mathbf{W}$ exclusively. Once the filters converge, we turn on learning for $\mathbf{R}$. $\mathbf{W}$ does not change very much beyond this point. We found learning of $\mathbf{R}$ was sensitive to learning rate. We set the learning rate to 0.05 per batch, used a momentum term of 0.75 and batches of 30 sets of 100 frame sequences. We whitened images with a center-surround filter and normalized the mean and variance of whitened pixel values in the training images to 0 and 1 respectively.

Gradients required for learning R show similarities to the STDP learning rule used in [Abbott and Blum, 1996] and [Rao and Sejnowski, 2000].

$$\frac{\partial \mathcal{L}^t_{\text{bgG-RNN}}}{\partial R_{jk}} = \left(h_k^{t-1} x_k^{t-1}\right) \cdot \left(h_j^t - \sigma\left(\mathbf{R}\left(\mathbf{h}^t \circ \mathbf{x}^t\right) + \mathbf{b}\right)_j\right). \tag{7.4}$$

We will assume for neural interpretation that the positive and negative values of $\mathbf{x}^t \circ \mathbf{h}^t$ are encoded by different neurons. If for a given neuron x_j^{t-1} is always positive, then the gradient 7.4 is only positive when $h_j^{t-1} = 1$ and $h_i^t = 1$ and negative when $h_j^{t-1} = 1$ and $h_i^t = 0$. In other words, the connection R_{ij} is strengthened when neuron j appears to cause neuron k to activate and inhibited if neuron j fails to activate neuron k. A similar effect can be observed for the negative part of x_j^{t-1}. This kind of Hebbian rule is widespread in cortex for long term learning and is used in previous computational models of neural sequence learning that partly motivated our work [Rao and Sejnowski, 2000].

7.4 Results

For data, we selected 100 short 100 frame long clips from a high resolution BBC wildlife documentary. Clips were chosen only if they seemed on visual inspection to have sufficient motion energy over the 100 frames. The clips chosen ended up being mostly panning shots and close-ups of animals in their natural habitats (the closer the camera is to a moving object, the faster it appears to move).

The results presented below measure the ability of the model to produce responses similar to those of neurons recorded in primate experiments. The stimuli used in these experiments are typically of two kinds: drifting gratings presented inside circular or square apertures or translating bars of various lengths. These two kinds of stimuli produce very clear motion signals, unlike motion produced by natural movies. In fact, most patches we used in training contained a wide range of spatial orientations, most of which were not orthogonal to the direction of local translation. After comparing model responses to neural data, we finish with an analysis of the connectivity pattern between model neurons that underlies their responses.

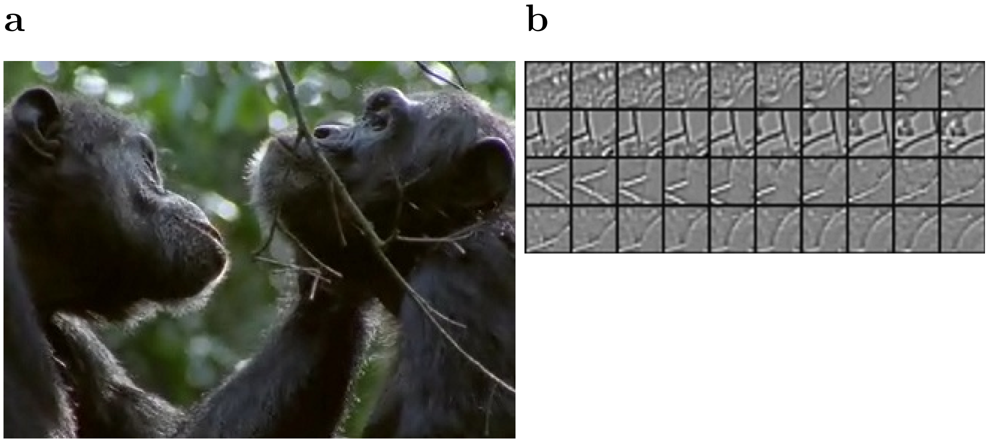

Figure 7.6: **a)** Snapshot of nature documentary used for learning the statistics of natural movies. **b)** Four samples of the sequences of patches extracted from the documentary.

7.4.1 Measuring responses in the model.

We first had to deal with the potential negativity of the variables in the model, since neural responses are always positive quantities. We decided to separate the positive and negative parts of the Gaussian variables into two distinct sets of responses. This interpretation is relatively common for sparse coding models and we also found that in many units direction selectivity was enhanced when the positive and negative parts of $\mathbf{x}^t$ were separated (as opposed to taking the absolute value for example). The enhancement was supported by a particular pattern of network connectivity which we describe in a later subsection.

Additionally, since our inference procedure is deterministic, it will produce the exact same response to the same stimulus every time. We added Gaussian noise to the spatially whitened test image sequences, partly to capture the noisy environments in cortex and partly to show robustness of direction selectivity to noise. The amount of noise added was about half the expected variance of the stimulus.

7.4.2 Direction selectivity and speed tuning.

Direction selectivity is measured with the following index: $\mathrm{DI} = 1 - R_{\mathrm{opp}}/R_{\mathrm{max}}$. Here R_{max} represents the response of a neuron in its preferred direction, while

R_{opp} is the response in the direction opposite to that preferred. This selectivity index is commonly used to characterize neural data. To define a neuron's preferred direction, we inferred latent coefficients over many repetitions of square gratings drifting in 24 directions, at speeds ranging from 0 to 3 pixels/frame in 0.25 steps. The periodicity of the stimulus was twice the patch size, so that motion locally appeared as an advancing long edge. The neuron's preferred direction was the direction in which it responded most strongly, averaged over all speeds. Once a preferred direction was established, we defined the neuron's preferred speed, as the speed at which it responded most strongly in its preferred direction. Finally, at this preferred speed and direction, we calculated the DI of the neuron. Similar results were obtained if we averaged over all speed conditions.

We found that most neurons in the model had sharp tuning curves and direction-selective responses. We cross validated the value of the direction index with a new set of responses to obtain an average DI of 0.65, with many neurons having a DI close to 1 (see figure 7.7c). 714 of 1,024 neurons were classified as direction-selective on the basis of having DI $>$ 0.5. Distributions of direction indices and optimal speeds are shown in figure 7.7c. A neuron's preferred direction was always close to orthogonal to the axis of its Gabor receptive field, except for a few degenerate cases around the edges of the patch. We defined the population tuning curve as the average of the tuning curves of individual neurons, each aligned by their preferred direction of motion. The DI of the population was 0.66. Neurons were also speed tuned, in that responses could vary greatly and systematically as a function of speed and DI was non-constant as a function of speed (see figure 7.7b). Usually at low and high speeds the DI was 0, but in between a variety of responses were observed. Speed tuning is also present in recorded V1 neurons [Orban et al., 1986], and could form the basis for global motion computation based on the intersection of constraints method [Simoncelli and Heeger, 1998].

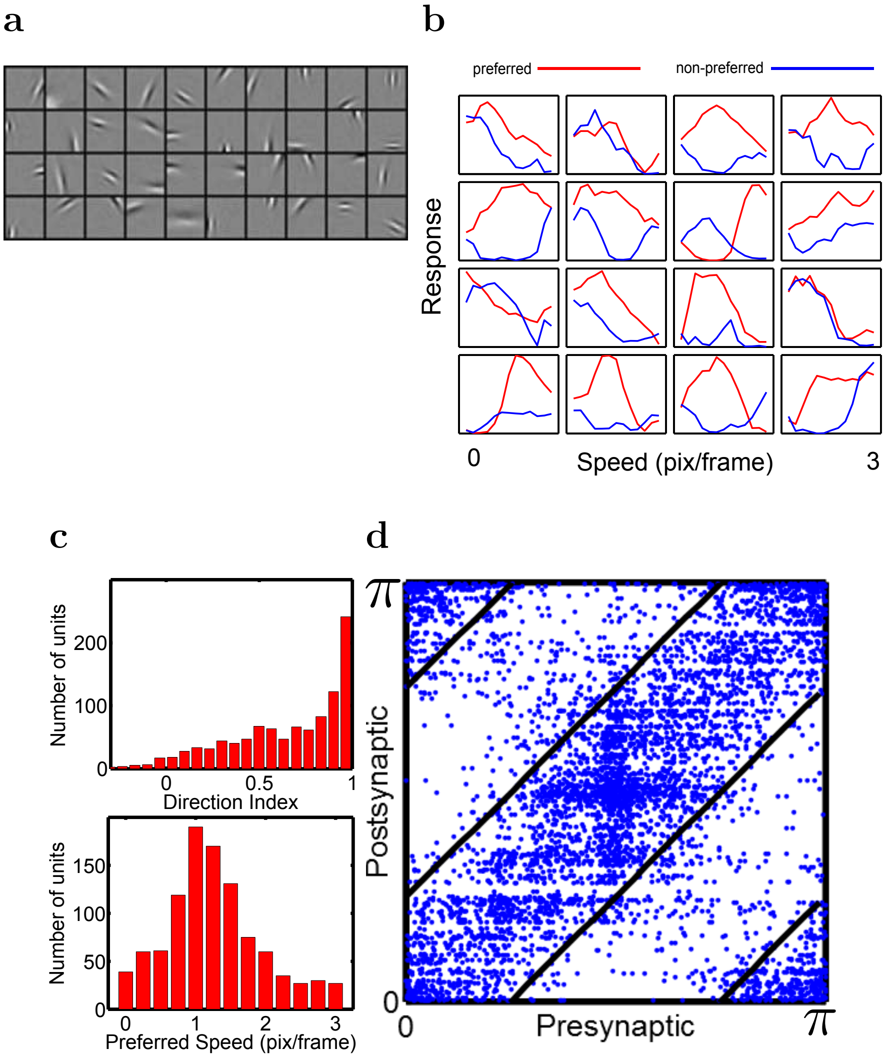

Figure 7.7: **Properties of the learned representations: static receptive fields, speed tuning, direction index and pairwise connectivities. a)** Population of static filters derived by the model. **b)** Speed tuning of 16 randomly chosen neurons. Note that some neurons only respond weakly without motion, some are inhibited in the non-preferred direction compared to static responses and most have a clear peak in the preferred direction at specific speeds. **c)** Top: Histogram of direction selectivity indices. Bottom: Histogram of preferred speeds. **d)** For each of the 10 strongest excitatory connections per neuron we plot an asterisk indicating the orientation selectivity of pre and post-synaptic units. Note that most of the points are within $\pi/4$ from the diagonal, an area marked by the black lines. Note also the relatively increased frequency of horizontal and vertical edges.

7.4.3 Vector velocity tuning

To get a more detailed description of single-neuron tuning, we investigated responses to different stimulus velocities. Since drifting gratings only contain motion orthogonal to their orientation, we switched to small (1.25pix x 2pix) drifting Gabors for these experiments. We tested the network's behavior with a full set of 24 Gabor orientations, drifting in a full set of 24 directions with speeds ranging from 0.25 pixels/frame to 3 pixels/frame, for a total of 6912 = 24 x 24 x 12 conditions with hundreds of repetitions of each condition. For each neuron we isolated its responses to drifting Gabors of the same orientation travelling at the 12 different speeds in the 24 different directions. We present these for several neurons in polar plots in figure 7.8c. Note responses tend to be high to vector velocities lying on a particular line. In the next section we show that these are the so called constraint lines.

7.4.4 Connectomics in silico

We had anticipated that the network would learn direction selectivity via specific patterns of recurrent connection, in a fashion similar to the toy model studied in Rao and Sejnowski [Rao and Sejnowski, 2000]. We now show that the pattern of connectivity indeed supports this computation.

The most obvious connectivity pattern, clearly visible for single neurons in figure 7.8b, shows that neurons in the model excite other neurons in their preferred direction and inhibit neurons in the opposite direction. This asymmetric wiring naturally supports direction selectivity in combination with the second pattern described below. This connectivity pattern emerges gradually during learning, as shown in figure 7.9, a feature apparent in snapshots of the connectivity at the beginning, middle and end of learning.

We find that asymmetry is not sufficient for direction selectivity to emerge — strong excitatory projections also have to connect neurons with similar preferred orientations and similar preferred directions. Only then will direction information propagate in the network in the identities of the active variables. We considered the 10 strongest excitatory outputs for each neuron and calculated the expected deviation between the orientation of these outputs and the orientation of the root neuron. The average deviation was 23^o, half the expected deviation if connections were random. Figure 7.7d shows a raster plot of the pairs of orientations. The same pattern held when we considered the strongest excitatory inputs to a given neuron with an expected deviation of orientations of 24^o. We could not directly measure if neurons connected together according to direction selectivity because of the sign ambiguity of $\mathbf{x}^t$ variables. One can visually assess in figure 7.8b that neurons connected asymmetrically with respect to their RF axis, but did they also respond to motion primarily in that direction? As can be seen in figure 7.8c, they did indeed. Since direction tuning is a measure of the *incoming* connections to the neuron, we can qualitatively assess recurrence primarily connected together neurons with similar direction preferences.

We also observed that neurons mostly projected strong excitatory outputs to other neurons that were aligned parallel to the root neuron's main axis (visible in figures 7.8b). This is reminiscent of the aperture problem: locally all edges appear to translate parallel to themselves. A neuron X with a preferred direction v and preferred speed s has a so-called constraint line (CL), parallel to the Gabor's axis. When the neuron is activated by an edge E, the constraint line is formed by all possible future locations of edge E that are consistent with global motion in the direction v with speed s. Due to the presence of long contours in natural scenes, the activation of X can predict at the next time step the activations of other neurons with RFs aligned on the CL. Our likelihood function encourages the model to learn to make such predictions as well as it can, and it indeed discovers to use the constraint line solution. To quantify the degree to which connections were made along a CL, for each neuron we fit a 2D Gaussian to the distribution of RF positions of the 20 most strongly connected neurons, each further weighted by its strength (the filled red circles in figure 7.8b). The major axis of the Gaussians represent the constraint lines of the root neuron and are in 862 out of 1024 neurons less than 15^o away from perfectly parallel to the root neurons' axis. The distance of each neuron to their constraint line was on average 1.68 pixels.

Yet perhaps the strongest manifestation of the CL tuning property of neurons in the model can be seen in their responses to small stimuli drifting with different vector velocities. Many of the neurons in figure 7.8c respond best when the velocity vector ends on the constraint line and a similar trend holds for the aligned population average.

It is already known from experiments of axon mappings simultaneous with dye-sensitive imaging that neurons in V1 are more likely to connect with neurons of similar orientations situated as far away as 4 mm / 4-8 minicolumns away [Skaggs and McNaughton, 1997]. The model presented here makes three further predictions: that neurons connect more strongly to neurons in their preferred direction, that connected neurons lie on the constraint line and that they have similar preferred directions to the root neuron.

7.5 Discussion

We have shown that a network of recurrently-connected neurons can learn to discriminate motion direction at the level of individual neurons. Online greedy filtering in the model is a sufficient approximate-inference method to produce direction-selective responses. Fast, causal and online inference is a necessary requirement for practical vision systems (such as the brain) but previous visual-motion models did not provide such an implementation of their inference algorithms. Another shortcoming of these previous models is that they obtain direction selectivity by having variables with different RFs at different time lags, effectively treating time as a third spatial dimension. A dynamic generative model may be more suited for online inference with such methods such as particle filtering, assumed density filtering, or the far cheaper method employed here of greedy filtering.

The model neurons can be interpreted as predicting the motion of the stimulus.

The lateral inputs they receive are however not sufficient in themselves to produce a response, the prediction also has to be consistent with the bottom-up input. When the two sources of information disagree, the network compromises but not always in favor of the bottom-up input, as this source of information might be noisy. This is reflected by the decrease in reconstruction accuracy from 80% to 60% after learning the recurrent connections. It is tempting to think of V1 direction selective neurons as not only edge detectors and contour predictors (through the nonclassical RF) but also predictors of future edge locations, through their specific patterns of connectivity.

The source of direction selectivity in cortex is still an unresolved question, but note that in the retina of non-primate mammals it is known with some certainty that recurrent inhibition in the non preferred direction is largely responsible for the direction selectivity of retinal ganglion cells [Fried et al., 2005]. It is also known that, unlike orientation and ocular dominance, direction selectivity requires visual experience to develop [Li et al., 2006], perhaps because direction selectivity depends on a specific pattern of lateral connectivity unlike the largely feedforward orientation and binocular tuning. Another experiment showed that after many exposures to the same moving stimulus, the sequence of spikes triggered in different neurons along the motion trajectory was also triggered in the complete absence of motion, again indicating that motion signals in cortex may be generated from lateral connections [Xu et al., 2012].

Thus, we see a number of reasons to propose that direction selectivity in the cortex may indeed develop and be computed through a mechanism analagous to the one we have developed here. If so, then experimental tests of the various predictions developed above should prove to be revealing.

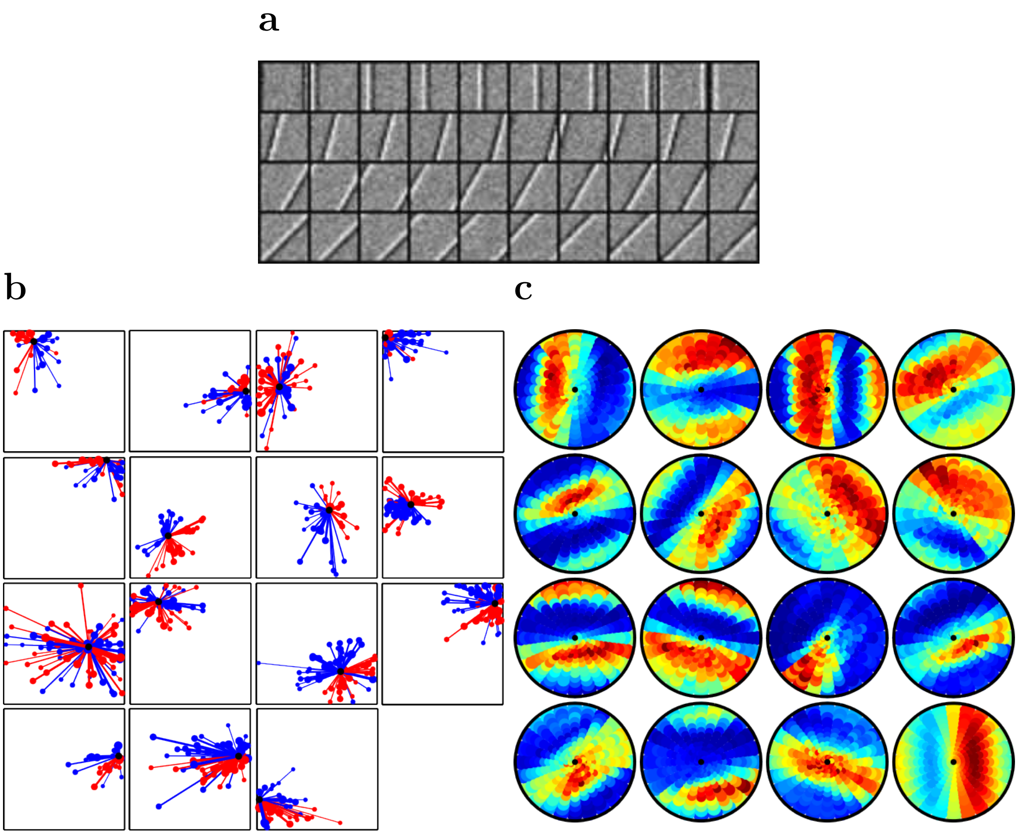

Figure 7.8: **Connectivity patterns between neurons enable selective responses to moving bars.** **a)** Test stimuli used to map direction selectivity. Dark bars were moving on a gray background in either of 24 random directions with one of 12 speeds. **b)** Each plot is based on the outgoing connections of a random set of direction-selective neurons. The centers of the Gabor fits to the neurons' receptive fields are shown as circles on a 16 by 16 square representing the image patch. The root neurons are shown as filled black circles. Filled red/black circles show neurons to which the root neurons have strong positive/negative connections, with a cutoff at one fourth of the maximal absolute connection. The width of the connecting lines and the area of the filled circles are proportional to the strength of the connection. A dynamic version of this plot during learning is shown as a movie in the supplementary material. **c)** The polar plots show the responses of neurons presented in *a* to small, drifting Gabors that match their respective orientations. Neurons are aligned in exactly the same manner on the 4 by 4 grid. Every disc in every polar plot represents one combination of speed and direction and the color of the disc represents the magnitude of the response, with intense red being maximal and dark blue minimal. The vector from the center of the polar plot to the center of each disc is proportional to the vector displacement of each consecutive frame in the stimulus sequence. Increasing disc sizes at faster speeds are used for display purposes. The very last polar plot shows the average of the responses of the entire population, when each neuron is aligned by its preferred direction.

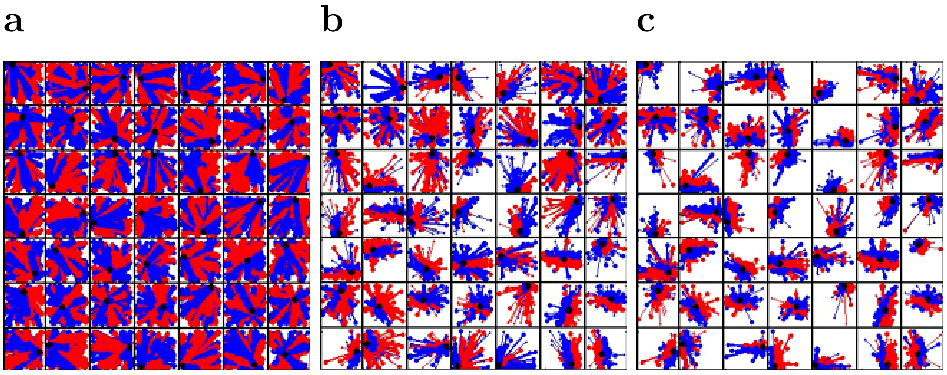

Figure 7.9: **Connectivity changes during learning. a)** We initialized the network with random connections between neurons. **bc)** During learning, connections gradually sparsify and become asymmetric between the two sides of the receptive fields of each cell.

VIII

Conclusion

We have developed statistical models that incorporate notions of dynamics and fitted these models directly to recorded multi-neuron data from motor and sensory cortices. Our approach bridges two existing computational methods in neuroscience: the relatively old tradition of computer simulations of networks and the newer model-based data fitting techniques.

Computer simulations are essential exploratory tools in neuroscience but they are often not well constrained by data. Simulation studies usually show that networks of neurons can reproduce certain properties reported in the literature, but many choices of parameters and network structure can also reproduce those same properties. With the recent advent of large-scale simulation studies, it seems the space of possible network parameters can increase in an unconstrained fashion.

We reason that the only way to meaningfully develop large-scale simulations of networks will be to directly fit all aspects of existing neurophysiological recordings. Much information about cortical networks is transparent in the temporal timecourses of different neural classes to varied inputs. While these details of the dynamics or of the receptive fields might be hard to describe explicitly and quantitatively, they can nonetheless be crucial information for statistically identifying the underlying network structure that generated them. The approach we suggest in this work uses all available data to fit network models that capture the statistical structure of the data, which in turn has been generated by real neuronal networks in the brain.

Note that other data fitting techniques have been developed to capture the shared variability in multi-neuron recordings ([Pillow et al., 2008]). However, the approach of [Pillow et al., 2008] as well as those of [Schneidman et al., 2005] and [Machens et al., 2010] lack the necessary network structure which allows us to interpret the fitted models and simulate them as dynamical networks. Most existing techniques for this purpose assume direct connections or interactions between neurons, yet most pairs of neurons in any brain area are not connected, and the functional connectivity between cell pairs is an indirect consequence of their participation in coordinated local network dynamics. Furthermore, fully pairwise-connected approaches to data modelling quickly run into the curse of dimensionality. The number of pairwise functional interactions scales quadratically with the number of recorded neurons, however the recording times usually remain the same, being typically constrained by the qualities of the biological preparation or the motivation of the animals.

We used the statistical network models to extract the underlying dynamical patterns of cortical responses in auditory cortex and formulated hypothesis about the cortical regimes of computation based on the inferred dynamics. Cortical networks in the synchronized state appear to be depression-stabilized, while network responses in the desynchronized state are consistent with an inhibition-stabilized regime. Previous work has studied such networks and showed that depression-stabilized networks agree with many observations of auditory cortex structure, while inhibition-stabilized networks may capture properties of the visual cortex ([Loebel et al., 2007], [Murphy and Miller, 2009]). We found that these two regimes can be exhibited by the same brain area in the same species in responses to the same stimuli, but under different brain states. It is thus possible that neural networks are more heterogeneous than thought across brain areas and species, but dynamical properties differ much more depending on brain state.

Indeed, in our respective preparations of the synchronized and desynchronized states in auditory cortex, we find strong evidence that the networks are stabilized by depression and inhibition respectively. Furthermore, we showed that depression-stabilized networks are inherently unstable to small perturbations. Depression is simply too slow to act as an effective negative feedback loop and an activated state can only be reset to quiescence by quick depletion of all the vesicles in the network. The dynamics of depression-stabilized networks are dominated by a single runaway excitatory mode which activates the entire population regardless of the qualities of the external stimulus and indeed even spontaneously.

Our statistical model fits identified the runaway excitatory mode of the network and also recovered a second excitatory mode closely-aligned with the first one and paired with it dynamically. The two trajectories together account for the stereotypical sequence of firing observed in the synchronized state. Activity packets, sometimes called population spikes, were shown to evolve dynamically and reliably across a two-dimensional space of tightly-aligned eigenvectors.

Such dynamics have been described in the past to explain large transient responses at stimulus onsets, but these studies have suggested the non-normal dynamics to be generated in a pair of excitatory and inhibitory populations ([Murphy and Miller, 2009]). Our model fits to the synchronized state suggests instead that both response modes or populations have excitatory effects on the network. Fast-spiking putative inhibitory neurons did not align with the late mode of dynamics; in fact their activity slightly preceded the average RS activity. Inhibitory interactions are still required for non-normal dynamics such that the second excitatory mode can inhibit the first one. A candidate class of interneurons for such interactions, likely not recorded in our experiments, are somatostatin-positive neurons, which have been shown before to have late onsets to auditory stimuli. In contrast, parvalbumin-positive neurons (likely FS cells in our dataset) have faster onsets to external stimuli than RS cells.

These two-dimensional dynamics dominate the statistical response properties of the network, greatly restricting the network capacity to encode stimuli. In contrast, the desynchronized network state appears to have much more flexible and high-dimensional response properties and can thus encode sensory stimuli more reliably. This is likely due to an overall increased ratio of inhibition to excitation, which was also observed in awake rodents ([Haider et al., 2013]). The ratio of recorded spikes of FS neurons to spikes of RS neurons was much greater in the desynchronized brain state than in the synchronized.

We showed in simulations that increased inhibitory neuron activity can transition a network state from synchronized to desynchronised, or equivalently, from depression-stabilized to inhibition-stabilized. Furthermore, in inhibitory-stabilized networks we reproduced a key property of the desynchronized state, namely that there are almost no noise correlations or trial-to-trial shared variability. Unlike depression-stabilized networks, an inhibition-stabilized network is robust to small perturbations due to the very fast negative feedback loop provided by inhibition, and the effect of small perturbations decays exponentially with the timescale of the excitatory and inhibitory conductances. Inhibition-stabilized networks clearly provide better coding properties not only due to the lack of trial-to-trial variability, but also because the inhibition balances the dominant excitatory response mode of the network, allowing other dynamical response modes to activate.

But are there any dynamics at all in the desynchronized state? To show that there are intracortical dynamics in the desynchronized state, we analyzed the dynamics of the neural responses to sustained tones and to random frequency-modulated noise sweeps with very short temporal autocorrelation. Neural responses had different properties in the desynchronized state, indicative of specific interactions between the FS and RS populations. The early transients to tone onsets were restricted to the FS population, suggesting that the increased effectiveness of the inhibitory neurons shuts off the early sensory responses of the much slower to respond putative excitatory neurons (RS). Late onset peaks in the sustained responses of both FS and RS neurons are consistent with an intra-cortical or local network origin of these responses. The late peak of the FS neurons was not present in the synchronized state, consistent with a lack of effective inhibition 30ms after stimulus onset.

Neural responses to random FM sweeps had long (50-100ms) autocorrelation properties despite stimuli being temporally uncorrelated at time lags of 10 ms or more. In contrast, subcortical responses did not have such long temporal autocorrelation. Having argued for the presence of dynamics in the desynchronized state, we fitted statistical dynamical models to speech-evoked responses. We found that the dimensionality of the fitted models was relatively high, and patterns of responses in spontaneous activity explained little of the response properties of the network to stimulation.

8.1 Emerging technologies for large-scale recordings

Over the past several decades, neural recording technologies have improved dramatically. In particular, the ability to monitor large, even complete populations with single neuron resolution is now becoming a reality with techniques like high-density electrophysiological probes and optical imaging. What challenges do the new recordings pose from a data analysis point of view and more importantly what new science can be conducted using them? While these questions may be best answered in practice, for the rest of this thesis we speculate and suggest possible applications.

Our analysis of chapter 4 suggested that animals in desynchronized brain states may encode relatively high-dimensional stimulus inputs. However many of the higher dimensions were very small compared to leading stimulus-encoding projections. Recording a larger number of neurons would allow a better ability to look at the small-variance signals in the brain, because these signals are distributed over the population and can be demixed from the multi-neuron activity with hidden Markov models such as the ones we have described here. Nothing so far suggests that the relevant brain computations are performed at a large, clearly-visible scale. In fact, the most large-scale signals that we currently see in recordings are synchronized periods of whole-population activity that are not linked to stimulus parameters or even to behavior (the animals are asleep).

Recording a large number of neurons simultaneously while animals are behaving would also enable more efficient single-trial analysis. Most electrophysiology studies still rely on averaging neural activity over trials, even when it is clear that a large amount of variability exists from trial to trial and is lost in the average. Instead, we suggest that in the future single trials of behavior will already be analyzed for important information by effectively averaging the neural activity over neurons instead of over trials. Neurons recorded often respond with similar spiking to other neurons, hence averaging the activity of a population would allow tracking their collective behavior closely. However, no neuron performs the exact same computation as another neuron. The underlying neural dynamics are distributed across the population and mixed together. The role of statistical models is then to demix the different sources of inputs and variability so as to find the weighted projections with most relevant information about the stimulus, the network computation or the behavior.

Another benefit of large-scale recordings may be to shed light on the noise that has been assumed to be overly-present in the brain. Single spikes are thought to occur with noisy timing and often be missed completely, but it may be possible to explain single spikes from the activity of all the other neurons in the local population. For example, recording all presynaptic sources of a neuron's dendritic input should in principle allow much better spike-level prediction than currently possible and may reveal computations that single neurons are performing.

Continuing the line of thought of the previous paragraph, recording the activity of a complete neural population may allow us to recover the actual connectome of pairwise connectivity. Currently the recovered functional connectivity from population recordings does not capture actual physical connections but only the distributions of common inputs that most pairs of neurons receive. Recovering physical connectivity from spiking responses will require recording an entire population with spike-level accuracy, so that no external common inputs can alter the correlation structure, because all the common inputs are within the recordings.

Bibliography

[Abbott and Blum, 1996] Abbott, L. and Blum, K. (1996). Functional significance of long-term potentiation for sequence learning and prediction. *Cerebral Cortex*, 6:406–416. (pages 117 and 133)

[Abolafia et al., 2013] Abolafia, J., Martinez-Garcia, M., Deco, G., and Sanchez-Vives, M. (2013). Variability and information content in auditory cortex spike trains during an interval-discrimination task. *Journal of Neurophysiology*, 110:2163–74. (page 15)

[Aizenberg and Geffen, 2013] Aizenberg, M. and Geffen, M. N. (2013). Bidirectional effects of aversive learning on perceptual acuity are mediated by the sensory cortex. *Nature Neuroscience*, 16(8):994–6. (page 107)

[Allman et al., 1985] Allman, J., Miezin, F., and McGuinness, E. (1985). Stimulus specific responses from beyond the classical receptive field: neurophysiological mechanisms for local-global comparisons in visual neurons. *Annual review of neuroscience*, 8(1):407–430. (page 14)

[Arieli et al., 1996] Arieli, A., Sterkin, A., Grinvald, A., and Aertsen, A. (1996). Dynamics of ongoing activity: explanation of the large variability in evoked cortical responses. *Science*, 273(5283):1868–71. (page 109)

[Atencio and Schreiner, 2013] Atencio, C. and Schreiner, C. (2013). Auditory cortical local subnetworks are characterized by sharply synchronous activity. *Journal of Neuroscience*, 33(47):18503–14. (pages 15 and 59)

[Azouz and Gray, 2003] Azouz, R. and Gray, C. M. (2003). Adaptive Coincidence Detection and Dynamic Gain Control in Visual Cortical Neurons In Vivo. *Neuron*, 37:513–523. (page 109)

[Bandyopadhyay et al., 2010] Bandyopadhyay, S., Shamma, S. A., and Kanold, P. O. (2010). Dichotomy of functional organization in the mouse auditory cortex. *Nature Neuroscience*, 13:361–368. (page 14)

[Banerjee and Liu, 2013] Banerjee, S. B. and Liu, R. C. (2013). Storing maternal memories: hypothesizing an interaction of experience and estrogen on sensory cortical plasticity to learn infant cues. *Frontiers in Neuroendocrinology*, 34(4):300–14. (page 107)

[Bao et al., 2004] Bao, S., Chang, E. F., Woods, J., and Merzenich, M. M. (2004). Temporal plasticity in the primary auditory cortex induced by operant perceptual learning. *Nature Neuroscience*, 7(9):974–81. (page 107)

[Barber, 2002] Barber, D. (2002). Learning in spiking neural assemblies. *Advances in Neural Information Processing*, 15. (page 118)

[Bathellier et al., 2012] Bathellier, B., Ushakova, L., and Rumpel, S. (2012). Discrete neocortical dynamics predict behavioral categorization of sounds. *Neuron*, 76(2):435–49. (pages 14, 96, and 109)

[Beltramo et al., 2013a] Beltramo, R., D'Urso, G., Dal Maschio, M., Farisello, P., Bovetti, S., Clovis, Y., Lassi, G., Tucci, V., Tonelli, D. D. P., and Fellin, T. (2013a). Layer-specific excitatory circuits differentially control recurrent network dynamics in the neocortex. *Nature neuroscience*, 16(2):227–234. (page 15)

[Beltramo et al., 2013b] Beltramo, R., D'Urso, G., Dal Maschio, M., Farisello, P., Bovetti, S., Clovis, Y., Lassi, G., Tucci, V., Tonelli, D. D. P., and Fellin, T. (2013b). Layer-specific excitatory circuits differentially control recurrent network dynamics in the neocortex. *Nature neuroscience*, 16(2):227–234. (page 59)

[Berkes et al., 2009] Berkes, P., Turner, R., and Sahani, M. (2009). A structured model of video produces primary visual cortical organisation. *PLoS Computational Biology*, 5. (page 118)

[Bermudez Contreras et al., 2013] Bermudez Contreras, E. J., Schjetnan, A. G. P., Muhammad, A., Bartho, P., McNaughton, B. L., Kolb, B., Gruber, A. J., and Luczak, A. (2013). Formation and reverberation of sequential neural activity patterns evoked by sensory stimulation are enhanced during cortical desynchronization. *Neuron*, 79(3):555–66. (pages 90, 92, and 105)

[Bishop, 2006] Bishop, C. M. (2006). *Pattern Recognition and Machine Learning*. Springer. (page 32)

[Brea et al., 2011] Brea, J., Senn, W., and Pfister, J. (2011). Sequence learning with hidden units in spiking neural networks. *Advances in Neural Information Processing*, 24. (page 118)

[Buesing et al., 2012] Buesing, L., Macke, J., and Sahani, M. (2012). Spectral learning of linear dynamics from generalised-linear observations with application to neural population data. *Advances in Neural Information Processing Systems*, 25. (page 30)

[Buzsaki, 2004] Buzsaki, G. (2004). Large-scale recording of neuronal ensembles. *Nature Neuroscience*, 7(5):446–51. (page 24)

[Cadieu and Olshausen, 2009] Cadieu, C. and Olshausen, B. (2009). Learning transformational invariants from natural movies. *Advances in Neural Information Processing*, 21:209–216. (pages 118 and 126)

[Cardin et al., 2009] Cardin, J., Carle, M., Meletis, K., Knoblich, U., Zhang, F., Deisseroth, K., Tsai, L., and Moore, C. (2009). Driving fast-spiking cells induces gamma rhythm and controls sensory responses. *Nature*, 459:663–7. (page 59)

[Castro-Alamancos, 2009] Castro-Alamancos, M. (2009). Cortical up and activated states: implications for sensory information processing. *The Neuroscientist*, pages 625–634. (pages 102 and 108)

[Castro-Alamancos, 2004a] Castro-Alamancos, M. A. (2004a). Absence of rapid sensory adaptation in neocortex during information processing states. *Neuron*, 41(3):455–464. (page 90)

[Castro-Alamancos, 2004b] Castro-Alamancos, M. A. (2004b). Dynamics of sensory thalamocortical synaptic networks during information processing states. *Progress in Neurobiology*, 74(4):213–47. (page 89)

[Cavanaugh et al., 2002] Cavanaugh, J. R., Bair, W., and Movshon, J. A. (2002). Nature and interaction of signals from the receptive field center and surround in macaque v1 neurons. *Journal of neurophysiology*, 88(5):2530–2546. (page 14)

[Churchland et al., 2010] Churchland, M. M., Yu, B., and al (2010). Stimulus onset quenches neural variability: a widespread cortical phenomenon. *Nature Neuroscience*, 13(3):369–78. (page 48)

[Churchland et al., 2007] Churchland, M. M., Yu, B. M., Sahani, M., and Shenoy, K. V. (2007). Techniques for extracting single-trial activity patterns from large-scale neural recordings. *Current Opinion in Neurobiology*, 17(5):609–618. (page 24)

[Cohen and Maunsell, 2009] Cohen, M. and Maunsell, J. (2009). Attention improves performance primarily by reducing interneuronal correlations. *Nature*, 12:1594–1600. (page 59)

[Constantinople and Bruno, 2011] Constantinople, C. and Bruno, R. (2011). Effects and mechanisms of wakefulness on local cortical networks. *Neuron*, 69:1061–1068. (pages 15 and 59)

[Cooke et al., 2007] Cooke, J. E., Zhang, H., and Kelly, J. B. (2007). Detection of sinusoidal amplitude modulated sounds: deficits after bilateral lesions of auditory cortex in the rat. *Hearing Research*, 231(1-2):90–9. (page 107)

[Crochet and Petersen, 2006] Crochet, S. and Petersen, C. C. H. (2006). Correlating whisker behavior with membrane potential in barrel cortex of awake mice. *Nature Neuroscience*, 9(5):608–10. (page 89)

[Curto et al., 2009] Curto, C., Sakata, S., Marguet, S., Itskov, V., and Harris, K. D. (2009). A simple model of cortical dynamics explains variability and state dependence of sensory responses in urethane-anesthetized auditory cortex. *The Journal of neuroscience*, 29(34):10600–12. (pages 15, 92, 105, 107, and 109)

[Dayan and Abbott, 2001] Dayan, P. and Abbott, L. (2001). *Theoretical Neuroscience*. The MIT Press. (page 118)

[de la Rocha et al., 2007] de la Rocha, J., Doiron, B., Shea-Brown, E., Josic, K., and Reyes, A. (2007). Correlation between neural spike trains increases with firing rate. *Nature*, 448:802–806. (page 15)

[Destexhe et al., 2007] Destexhe, A., Hughes, S. W., Rudolph, M., and Crunelli, V. (2007). Are corticothalamic 'up' states fragments of wakefulness? *Trends in Neurosciences*, 30(7):334–42. (pages 102 and 108)

[Destexhe et al., 2003] Destexhe, A., Rudolph, M., and Pare, D. (2003). The high-conductance state of neocortical neurons in vivo. *Nature Reviews Neuroscience*, 4:739–751. (page 63)

[Doucet et al., 2000] Doucet, A., Freitas, N., Murphy, K., and Russell, S. (2000). Rao-blackwellised particle filtering for dynamic Bayesian networks. *UAI'00 Proceedings of the Sixteenth conference on Uncertainty in artificial intelligence*, pages 176–183. (page 128)

[Douglas et al., 1995] Douglas, R., Koch, C., Mahowald, M., Martin, K., and Suarez, H. (1995). Recurrent excitation in neocortical circuits. *Science*, 269(5226):981–985. (page 119)

[Ecker et al., 2014] Ecker, A. S., Berens, P., Cotton, R. J., Subramaniyan, M., Denfield, G. H., Cadwell, C. R., Smirnakis, S. M., Bethge, M., and Tolias, A. S. (2014). State Dependence of Noise Correlations in Macaque Primary Visual Cortex. *Neuron*, 82(1):235–248. (pages 15 and 108)

[Eliades and Wang, 2008] Eliades, S. and Wang, X. (2008). Neural substrates of vocalization feedback monitoring in primate auditory cortex. *Nature*, 453:1102–06. (page 59)

[Elman, 1990] Elman, J. (1990). Finding structure in time. *Cognitive Science*, 14:179–211. (page 29)

[Ferster and Miller, 2000] Ferster, D. and Miller, K. D. (2000). Neural mechanisms of orientation selectivity in the visual cortex. *Annual Review of Neuroscience*, 23(1):441–471. (page 14)

[Fried et al., 2005] Fried, S., Munch, T., and Werblin, F. (2005). Directional selectivity is formed at multiple levels by laterally offset inhibition in the rabbit retina. *Neuron*, 46(1):117–127. (page 140)

[Friston, 1999] Friston, K. (1999). A theory of cortical responses. *Phil. Trans. R. Soc. B*, 360(1456):815–836. (page 119)

[Gabernet et al., 2005] Gabernet, L., Jadhav, S. P., Feldman, D. E., Carandini, M., and Scanziani, M. (2005). Somatosensory integration controlled by dynamic thalamocortical feed-forward inhibition. *Neuron*, 48:315–327. (page 16)

[Garcia-Lazaro et al., 2013] Garcia-Lazaro, J. A., Belliveau, L. A. C., and Lesica, N. A. (2013). Independent population coding of speech with sub-millisecond precision. *The Journal of Neuroscience*, 33(49):19362–72. (page 95)

[Giraud and Poeppel, 2012] Giraud, A.-L. and Poeppel, D. (2012). Cortical oscillations and speech processing: emerging computational principles and operations. *Nature Neuroscience*, 15(4):511–7. (page 109)

[Goard and Dan, 2009] Goard, M. and Dan, Y. (2009). Basal forebrain activation enhances cortical coding of natural scenes. *Nature Neuroscience*, 12(11):1444–9. (pages 15 and 90)

[Goodfellow et al., 2012] Goodfellow, I., Courville, A., and Bengio, Y. (2012). Spike-and-slab sparse coding for unsupervised feature discovery. arXiv:1201.3382v2. (page 129)

[Greenberg et al., 2008] Greenberg, D. S., Houweling, A. R., and Kerr, J. N. D. (2008). Population imaging of ongoing neuronal activity in the visual cortex of awake rats. *Nature Neuroscience*, 11(7):749–51. (page 89)

[Gu et al., 2011] Gu, Y., Liu, S., Fetsch, C., Yang, Y., Fok, S., Sunkara, A., DeAngelis, G., and Angelaki, D. (2011). Perceptual learning reduces interneuronal correlations in macaque visual cortex. *Neuron*, 71(4):750–61. (page 59)

[Guo et al., 2012] Guo, W., Chambers, A. R., Darrow, K. N., Hancock, K. E., Shinn-Cunningham, B. G., and Polley, D. B. (2012). Robustness of cortical topography across fields, laminae, anesthetic states, and neurophysiological signal types. *The Journal of Neuroscience*, 32(27):9159–72. (page 90)

[Haider et al., 2013] Haider, B., Hausser, M., and Carandini, M. (2013). Inhibition dominates sensory responses in the awake cortex. *Nature*, 493:97–100. (pages 15, 59, and 146)

[Haider and McCormick, 2009] Haider, B. and McCormick, D. a. (2009). Rapid neocortical dynamics: cellular and network mechanisms. *Neuron*, 62(2):171–89. (page 89)

[Hamilton et al., 2013] Hamilton, L., Sohl-Dickstein, J., Huth, A., Carels, V., Deisseroth, K., and Bao, S. (2013). Optogenetic activation of an inhibitory network enhances feedforward functional connectivity in auditory cortex. *Nature*, 80:1066–76. (page 59)

[Han and Mrsic-Flogel, 2013] Han, Y. and Mrsic-Flogel, T. (2013). A finely tuned cortical amplifier. *Nature Neuroscience*, 16(9):1166–1168. (page 14)

[Harris and Thiele, 2011] Harris, K. D. and Thiele, A. (2011). Cortical state and attention. *Nature Reviews Neuroscience*, 12(9):509–23. (pages 89, 108, and 109)

[Hasenstaub et al., 2007] Hasenstaub, A., Sachdev, R. N. S., and McCormick, D. a. (2007). State changes rapidly modulate cortical neuronal responsiveness. *The Journal of Neuroscience*, 27(36):9607–22. (pages 90 and 109)

[Hirata and Castro-Alamancos, 2011] Hirata, A. and Castro-Alamancos, M. A. (2011). Effects of cortical activation on sensory responses in barrel cortex. *Journal of Neurophysiology*, 105(4):1495–505. (pages 15 and 90)

[Horvath and Lesica, 2011] Horvath, D. and Lesica, N. A. (2011). The effects of interaural time difference and intensity on the coding of low-frequency sounds in the mammalian midbrain. *The Journal of neuroscience : the official journal of the Society for Neuroscience*, 31(10):3821–7. (page 96)

[Hromadka et al., 2013] Hromadka, T., Zador, A. M., and DeWeese, M. R. (2013). Up states are rare in awake auditory cortex. *Journal of Neurophysiology*, 109:1989–1995. (page 74)

[Jones et al., 2001] Jones, H., Grieve, K., Wang, W., and Sillito, A. (2001). Surround suppression in primate v1. *Journal of Neurophysiology*, 86(4):2011–2028. (page 14)

[Kalman, 1960] Kalman, R. (1960). A new approach to linear filtering and prediction problems. *Journal of Basic Engineering*, 82(1):35–45. (pages 21 and 24)

[Kaufman et al., 2014] Kaufman, M. T., Churchland, M. M., Ryu, S. I., and Shenoy, K. V. (2014). Cortical activity in the null space: permitting preparation without movement. *Nature Neuroscience*, 17:440–448. (page 47)

[Kayser et al., 2009] Kayser, C., Montemurro, M. A., Logothetis, N. K., and Panzeri, S. (2009). Spike-phase coding boosts and stabilizes information carried by spatial and temporal spike patterns. *Neuron*, 61(4):597–608. (page 109)

[Kimura et al., 2014] Kimura, R., Sohya, K., Tsumoto, T., Safari, M., Mirnajafi-Zadeh, J., Ebina, T., and Yanagawa, Y. (2014). Curtailing effect of awakening on visual responses of cortical neurons by cholinergic activation of inhibitory circuits. *Journal of Neuroscience*, 34(30):10122–33. (page 59)

[Lakatos et al., 2013] Lakatos, P., Musacchia, G., O'Connel, M. N., Falchier, A. Y., Javitt, D. C., and Schroeder, C. E. (2013). The spectrotemporal filter mechanism of auditory selective attention. *Neuron*, 77(4):750–61. (page 109)

[Latham et al., 2010] Latham, P. E., Richmond, B., Nelson, P., and Nirenberg, S. (2010). Intrinsic dynamics in neuronal networks. *Journal of Neurophysiology*, 83(2):808–827. (page 15)

[Li et al., 2013a] Li, L.-y., Li, Y.-t., Zhou, M., Tao, H. W., and Zhang, L. I. (2013a). Intracortical multiplication of thalamocortical signals in mouse auditory cortex. *Nature Neuroscience*, 16(9):1179–1181. (page 14)

[Li et al., 2006] Li, Y., FitzPatrick, D., and White, L. (2006). The development of direction selectivity in ferret visual cortex requires early visual experience. *Nature Neuroscience*, 9(5):676–681. (page 140)

[Li et al., 2013b] Li, Y.-t., Ibrahim, L. A., Liu, B.-h., Zhang, L. I., and Tao, H. W. (2013b). Linear transformation of thalamocortical input by intracortical excitation. *Nature Neuroscience*, 16(9):1324–1330. (page 14)

[Lien and Scanziani, 2013] Lien, A. D. and Scanziani, M. (2013). Tuned thalamic excitation is amplified by visual cortical circuits. *Nature Neuroscience*. (page 14)

[Litwin-Kumar and Doiron, 2012] Litwin-Kumar, A. and Doiron, B. (2012). Slow dynamics and high variability in balanced cortical networks with clustered connections. *Nature Neuroscience*, 15:1498–1505. (page 17)

[Livingstone, 1998] Livingstone, M. (1998). Mechanisms of direction selectivity in macaque V1. *Neuron*, 20:509–526. (page 117)

[Loebel et al., 2007] Loebel, A., Nelken, I., and Tsodyks, M. (2007). Processing of sounds by population spikes in a model of primary auditory cortex. *Frontiers in Neuroscience*, 1(1):197–209. (pages 15 and 144)

[London et al., 2010] London, M., Roth, A., Beeren, L., Hausser, M., and Latham, P. (2010). Sensitivity to perturbations in vivo implies high noise and suggests rate coding in cortex. *Nature*, 466:123–127. (page 65)

[Luczak et al., 2009] Luczak, A., Barthó, P., and Harris, K. D. (2009). Spontaneous events outline the realm of possible sensory responses in neocortical populations. *Neuron*, 62(3):413–25. (pages 15, 59, 96, 99, and 109)

[Luczak et al., 2013] Luczak, A., Bartho, P., and Harris, K. D. (2013). Gating of sensory input by spontaneous cortical activity. *The Journal of Neuroscience*, 33(4):1684–95. (pages 89, 90, 99, 107, and 109)

[Machens et al., 2010] Machens, C. K., Romo, R., and Brody, C. D. (2010). Functional, but not anatomical, separation of what and when in prefrontal cortex. *Journal of Neuroscience*, 30(1):350–360. (page 144)

[Macke et al., 2011] Macke, J., Busing, L., Cunningham, J., Yu, B., Shenoy, K., and Sahani, M. (2011). Empirical models of spiking in neural populations. *Advances in Neural Information Processing Systems*, 24:1350–1358. (pages 24, 30, and 34)

[MacLean et al., 2005] MacLean, J. N., Watson, B. O., Aaron, G. B., and Yuste, R. (2005). Internal dynamics determine the cortical response to thalamic stimulation. *Neuron*, 48(5):811–23. (pages 15 and 109)

[Mallat and Zhang, 1993] Mallat, S. and Zhang, Z. (1993). Matching pursuits with time-frequency dictionaries. *IEEE Transactions on Signal Processing*, 41(12):3397–3415. (page 130)

[Marguet and Harris, 2011] Marguet, S. L. and Harris, K. D. (2011). State-dependent representation of amplitude-modulated noise stimuli in rat auditory cortex. *The Journal of Neuroscience*, 31(17):6414–20. (pages 15, 89, 90, 92, 105, and 107)

[Middleton et al., 2012] Middleton, J., Omar, C., Doiron, B., and Simons, D. (2012). Neural correlation is stimulus modulated by feedforward inhibitory circuitry. *Jorunal of Neuroscience*, 32(2):506–18. (page 15)

[Mikami et al., 1986] Mikami, A., Newsome, W., and Wurtz, R. (1986). Motion selectivity in macaque visual cortex. II. Spatiotemporal range of directional interactions in MT and V1. *Journal of Neurophysiology*, 55(6):1328–1339. (page 117)

[Mikolov et al., 2011] Mikolov, T., Deoras, A., Kombrink, S., Burget, L., and Cernocky, J. (2011). Empirical evaluation and combination of advanced language modeling techniques. *Conference of the International Speech Communication Association.* (page 30)

[Minka, 2001] Minka, T. (2001). Expectation propagation for approximate Bayesian inference. *UAI'01 Proceedings of the Seventeenth conference on Uncertainty in artificial intelligence*, pages 362–369. (page 128)

[Mitchell et al., 2009] Mitchell, J. F., Sundberg, K. A., and Reynolds, J. H. (2009). Spatial attention decorrelates intrinsic activity fluctuations in macaque area v4. *Neuron*, 63:879–888. (page 15)

[Murphy and Miller, 2009] Murphy, B. K. and Miller, K. D. (2009). Balanced amplification: A new mechanism of selective amplification of neural activity patterns. *Neuron*, 61:635–648. (pages 15, 144, and 145)

[Okun et al., 2012] Okun, M., Yger, P., Marguet, S. L., Gerard-Mercier, F., Benucci, A., Katzner, S., Busse, L., Carandini, M., and Harris, K. D. (2012). Population rate dynamics and multineuron firing patterns in sensory cortex. *The Journal of Neuroscience*, 32(48):17108–19. (pages 59, 89, 92, and 105)

[Olshausen, 2003] Olshausen, B. (2003). Learning sparse, overcomplete representations of time-varying natural images. *IEEE International Conference on Image Processing.* (page 117)

[Olshausen and Millman, 2000] Olshausen, B. and Millman, K. (2000). Learning sparse codes with a mixture-of-Gaussians prior. *Advances in Neural Information Processing*, 12. (page 129)

[Orban et al., 1986] Orban, G., Kennedy, H., and Bullier, J. (1986). Velocity sensitivity and direction selectivity of neurons in areas V1 and V2 of the monkey: influence of eccentricity. *Journal of Neurophysiology*, 56(2):462–480. (page 135)

[Otazu et al., 2009] Otazu, G. H., Tai, L.-H., Yang, Y., and Zador, A. M. (2009). Engaging in an auditory task suppresses responses in auditory cortex. *Nature Neuroscience*, 12(5):646–54. (pages 15, 90, and 108)

[Pillow et al., 2008] Pillow, J. W., Shlens, J., Paninski, L., Sher, A., Litke, A. M., Chichilnisky, E. J., and Simoncelli, E. P. (2008). Spatio-temporal correlations and visual signalling in a complete neuronal population. *Nature*, 454(7207):995–999. (pages 24, 33, and 144)

[Polack et al., 2013] Polack, P.-O., Friedman, J., and Golshani, P. (2013). Cellular mechanisms of brain state-dependent gain modulation in visual cortex. *Nature neuroscience*, 16(9):1331–9. (page 89)

[Porter et al., 2011] Porter, B. A., Rosenthal, T. R., Ranasinghe, K. G., and Kilgard, M. P. (2011). Discrimination of brief speech sounds is impaired in rats with auditory cortex lesions. *Behavioural Brain Research*, 219(1):68–74. (page 107)

[Poulet and Petersen, 2008] Poulet, J. F. A. and Petersen, C. C. H. (2008). Internal brain state regulates membrane potential synchrony in barrel cortex of behaving mice. *Nature*, 454(7206):881–5. (page 89)

[Rao and DH, 1999] Rao, R. and DH, B. (1999). Predictive coding in the visual cortex: a functional interpretation of some extra-classical receptive-field effects. *Nature Neuroscience*, 2(1):79–87. (page 119)

[Rao and Sejnowski, 2000] Rao, R. and Sejnowski, T. (2000). Predictive sequence learning in recurrent neocortical circuits. *Advances in Neural Information Processing*, 12:164–170. (pages 117, 119, 120, 133, and 137)

[Reed et al., 2011] Reed, A., Riley, J., Carraway, R., Carrasco, A., Perez, C., Jakkamsetti, V., and Kilgard, M. P. (2011). Cortical map plasticity improves learning but is not necessary for improved performance. *Neuron*, 70(1):121–31. (page 107)

[Renart et al., 2010] Renart, A., de la Rocha, J., Bartho, P., Hollender, L., Parga, N., Reyes, A., and Harris, K. D. (2010). The asynchronous state in cortical circuits. *Science (New York, N.Y.)*, 327(5965):587–90. (pages 17, 72, 73, 107, and 108)

[Rigas and Castro-Alamancos, 2007] Rigas, P. and Castro-Alamancos, M. A. (2007). Thalamocortical Up states: differential effects of intrinsic and extrinsic cortical inputs on persistent activity. *The Journal of Neuroscience*, 27(16):4261–72. (page 109)

[Ringach, 2009] Ringach, D. L. (2009). Spontaneous and driven cortical activity: implications for computation. *Current Opinion in Neurobiology*, 19(4):439–44. (page 109)

[Rothschild et al., 2010a] Rothschild, G., Nelken, I., and Mizrahi, A. (2010a). Functional organization and population dynamics in the mouse primary auditory cortex. *Nature Neuroscience*, 13:353–360. (page 14)

[Rothschild et al., 2010b] Rothschild, G., Nelken, I., and Mizrahi, A. (2010b). Functional organization and population dynamics in the mouse primary auditory cortex. *Nature Neuroscience*, 13:353–60. (page 59)

[Rumelhart et al., 1986] Rumelhart, D., Hinton, G., and Williams, R. (1986). Learning internal representations by error propagation. *Mit Press Computational Models Of Cognition And Perception Series*, pages 318–462. (page 30)

[Sachidhanandam et al., 2013] Sachidhanandam, S., Sreenivasan, V., Kyriakatos, A., Kremer, Y., and Petersen, C. C. H. (2013). Membrane potential correlates of sensory perception in mouse barrel cortex. *Nature Neuroscience*, 16(11):1671–7. (page 89)

[Sahani and Linden, 2003] Sahani, M. and Linden, J. (2003). How linear are auditory cortical responses? In Becker, S., Thrun, S., and Obermayer, K., editors, *Advances in neural information processing systems 15*, pages 301–308, Cambridge, MA. MIT. (page 96)

[Sakata and Harris, 2009] Sakata, S. and Harris, K. (2009). Laminar structure of spontaneous and sensory-evoked population activity in auditory cortex. *Neuron*, 64:404–18. (page 59)

[Sato et al., 2013] Sato, T. K., Häusser, M., and Carandini, M. (2013). Distal connectivity causes summation and division across mouse visual cortex. *Nature neuroscience.* (page 14)

[Sato et al., 2012] Sato, T. K., Nauhaus, I., and Carandini, M. (2012). Traveling waves in visual cortex. *Neuron*, 75:218–229. (page 15)

[Schneider et al., 2014] Schneider, D., Nelson, A., and Mooney, R. (2014). A synaptic and circuit basis for corollary discharge in the auditory cortex. *Nature*, 513:189–194. (page 59)

[Schneidman et al., 2005] Schneidman, E., Berry, M., Segev, R., and Bialek, W. (2005). Weak pairwise correlations imply strongly correlated network states in a neural population. *Nature*, 440:1007–1012. (pages 24, 31, 34, and 144)

[Simoncelli and Heeger, 1998] Simoncelli, E. and Heeger, D. (1998). A model of neuronal responses in visual area MT. *Vision Research*, 38(5):743–761. (page 135)

[Skaggs and McNaughton, 1997] Skaggs, W. and McNaughton, B. (1997). Replay of neuronal firing sequences in rat hippocampus during sleep following spatial experience. *Journal of Neuroscience*, 17(6):2112–2127. (page 139)

[Song et al., 2006] Song, W.-J., Kawaguchi, H., Totoki, S., Inoue, Y., Katura, T., Maeda, S., Inagaki, S., Shirasawa1, H., and Nishimura, M. (2006). Cortical intrinsic circuits can support activity propagation through an isofrequency strip of the guinea pig primary auditory cortex. *Cerebral Cortex*, 16:718–729. (page 15)

[Steriade et al., 2001] Steriade, M., Timofeev, I., and Grenier, F. (2001). Natural waking and sleep states: a view from inside neocortical neurons. *Journal of Neurophysiology*, 85(5):1969–1985. (page 89)

[Sun et al., 2010] Sun, Y. J., Kim, Y.-J., Ibrahim, L. A., Tao, H. W., and Zhang, L. I. (2010). Response features of parvalbumin-expressing interneurons suggest precise roles for subtypes of inhibition in visual cortex. *Neuron*, 67(5):847–857. (page 16)

[Sun et al., 2014] Sun, Y. J., Kim, Y.-J., Ibrahim, L. A., Tao, H. W., and Zhang, L. I. (2014). Synaptic mechanisms underlying functional dichotomy between intrinsic-bursting and regular-spiking neurons in auditory cortical layer 5. *Journal of Neuroscience*, 33(12):5326–5339. (page 15)

[Tan et al., 2013] Tan, A., Andoni, S., and Priebe, N. (2013). A spontaneous state of weakly correlated synaptic excitation and inhibition in visual cortex. *Neuroscience*, 247:364–75. (page 15)

[Tan et al., 2014] Tan, A. Y. Y., Chen, Y., Scholl, B., Seidemann, E., and Priebe, N. J. (2014). Sensory stimulation shifts visual cortex from synchronous to asynchronous states. *Nature*. (pages 15 and 89)

[Ter-Mikaelian et al., 2007] Ter-Mikaelian, M., Sanes, D. H., and Semple, M. N. (2007). Transformation of temporal properties between auditory midbrain and cortex in the awake Mongolian gerbil. *The Journal of Neuroscience*, 27(23):6091–102. (page 90)

[van Vreewijk and Sompolinsky, 1996] van Vreewijk, C. and Sompolinsky, H. (1996). Chaos in neuronal networks with balanced excitatory and inhibitory activity. *Science*, 274(5293):1724–1726. (page 72)

[Wehr and Zador, 2005] Wehr, M. and Zador, A. (2005). Synaptic mechanisms of forward suppression in rat auditory cortex. *Nature*, 47:437–445. (pages 15, 16, and 63)

[Wetzel et al., 1998] Wetzel, W., Ohl, F. W., Wagner, T., and Scheich, H. (1998). Right auditory cortex lesion in Mongolian gerbils impairs discrimination of rising and falling frequency-modulated tones. *Neuroscience Letters*, 252(2):115–8. (page 107)

[Wiskott and Sejnowski, 2002] Wiskott, L. and Sejnowski, T. (2002). Slow feature analysis: Unsupervised learning of invariances. *Neural Computation*, 14(4):715–770. (page 118)

[Wolf et al., 2014] Wolf, F., Engelken, R., Puelma-Touzel, M., Weidinger, J. D. F., and Neef, A. (2014). Dynamical models of cortical circuits. *Current Opinion in Neurobiology*, 25:228–236. (page 15)

[Xu et al., 2012] Xu, S., Jiang, W., Poo, M.-M., and Dan, Y. (2012). Activity recall in a visual cortical ensemble. *Nature Neuroscience*, 15(3):449–55, S1–2. (pages 89 and 140)

[Yu et al., 2006] Yu, B., Afshar, A., Santhanam, G., Ryu, S., Shenoy, K., and Sahani, M. (2006). Extracting dynamical structure embedded in neural activity. *Advances in Neural Information Processing Systems*, 18:1545–1552. (page 24)

[yun Li et al., 2014] yun Li, L., Xiong, X. R., Ibrahim, L. A., Yuan, W., Tao, H. W., , and Zhang, L. I. (2014). Differential receptive field properties of parvalbumin and somatostatin inhibitory neurons in mouse auditory cortex. *Cerebral Cortex*, online. (pages 15 and 16)

[Zhang et al., 2014] Zhang, S., Xu, M., Kamigaki, T., Do, J. P. H., Chang, W.-C., Jenvay, S., Miyamichi, K., Luo, L., and Dan, Y. (2014). Long-range and local circuits for top-down modulation of visual cortex processing. *science*, 345(6197):660–665. (page 14)

[Zhou et al., 2014a] Zhou, M., Liang, F., Xiong, X. R., Li, L., Li, H., Xiao, Z., Tao, H. W., and Zhang, L. I. (2014a). Scaling down of balanced excitation and inhibition by active behavioral states in auditory cortex. *Nature Neuroscience*, (April). (pages 89 and 90)

[Zhou et al., 2014b] Zhou, Y., hua Liu, B., Wu, G. K., Kim, Y.-J., and Xiao, Z. (2014b). Preceding inhibition silences layer 6 neurons in auditory cortex. *Neuron*, 65:706–717. (page 15)

[Zion Golumbic et al., 2013] Zion Golumbic, E. M., Ding, N., Bickel, S., Lakatos, P., Schevon, C. a., McKhann, G. M., Goodman, R. R., Emerson, R., Mehta, A. D., Simon, J. Z., Poeppel, D., and Schroeder, C. E. (2013). Mechanisms underlying selective neuronal tracking of attended speech at a ”cocktail party”. *Neuron*, 77(5):980–91. (page 109)